

DISSERTATION

**DIAGNOSTICS OF CARBON AND SILICON-BASED PLASMAS: FROM
SURFACE CHEMISTRY TO GAS-PHASE PHYSICS**

Submitted by

Jie Zhou

Department of Chemistry

In partial fulfillment of the requirements

for the degree of Doctor of Philosophy

Colorado State University

Fort Collins, Colorado

Spring, 2006

UMI Number: 3226165

INFORMATION TO USERS

The quality of this reproduction is dependent upon the quality of the copy submitted. Broken or indistinct print, colored or poor quality illustrations and photographs, print bleed-through, substandard margins, and improper alignment can adversely affect reproduction.

In the unlikely event that the author did not send a complete manuscript and there are missing pages, these will be noted. Also, if unauthorized copyright material had to be removed, a note will indicate the deletion.

UMI[®]

UMI Microform 3226165

Copyright 2006 by ProQuest Information and Learning Company.

All rights reserved. This microform edition is protected against unauthorized copying under Title 17, United States Code.


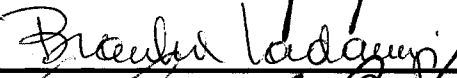


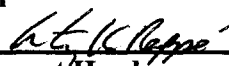
ProQuest Information and Learning Company
300 North Zeeb Road
P.O. Box 1346
Ann Arbor, MI 48106-1346

COLORADO STATE UNIVERSITY

November 14, 2005

WE HEREBY RECOMMEND THAT THE DISSERTATION PREPARED UNDER OUR SUPERVISION BY JIE ZHOU ENTITLED **DIAGNOSTICS OF CARBON AND SILICON-BASED PLASMAS FROM SURFACE CHEMISTRY TO GAS-PHASE PHYSICS** BE ACCEPTED AS FULFILLING IN PART THE REQUIREMENTS FOR THE DEGREE OF DOCTOR OF PHILOSOPHY

Committee on Graduate Work

	DORHOOT
David Grainger	GRAINGER
	LADANYI
Bruce Ladanyi	LADANYI
	L.A. Belfiore
L.A. Belfiore	L.A. Belfiore
	FISHER
Ellen Fisher	FISHER
Advisor	
	
H. Klapp	
Department Head	

ABSTRACT OF DISSERTATION

DIAGNOSTICS OF CARBON AND SILICON BASED PLASMAS FROM SURFACE CHEMISTRY TO GAS-PHASE PHYSICS

Plasma enhanced chemical vapor deposition (PECVD) has been widely used for deposition of organic polymers and carbon or silicon-based materials. A variety of gas phase, plasma-surface, and surface analysis techniques were used to provide a full understanding of these plasmas. This dissertation first describes the synthesis of a nanostructured composite material formed from plasma-polymerized polypyrrole (PPPy) coated Au fibers. The chemical, structural, and electrochemical characteristics of PPPy films were characterized by Fourier transform infrared spectroscopy (FTIR), X-ray photoelectron spectroscopy (XPS), and UV-Vis spectroscopy as well as cyclic voltammetry (CV), and scanning electron microscopy (SEM). Higher degree of retained functional group in the polypyrrole backbone was found with increasing duty cycle of pulsed plasma. In addition, as-deposited PPPy films coated on Au nanotubes demonstrate better electrochemical properties than as-deposited PPPy films coated on flat indium tin oxide (ITO) electrodes as a result of the increase in surface area and decrease in film thickness.

Langmuir probe and mass spectrometry measurements were used to characterize the gas-phase of low pressure, 13.56 MHz inductively coupled plasmas

used for deposition of diamond-like carbon (DLC) thin films. The ionic composition of Ar and CH₄/Ar plasma molecular beams was studied using a mass spectrometer with energy analysis capabilities. Low-energy peaks contributed significantly to the total area of the ion energy distributions (IEDs) measured for Ar⁺ in Ar and CH₄/Ar plasmas. In contrast, for all other ions in these systems, the low-energy peaks had a lower contribution to the IEDs as a result of the low probability of energy exchange via ion-neutral collisions. Hydrogenated DLC films were deposited on silicon wafers at different substrate potentials to determine the effect of ion bombardment on film properties. The hydrogen content, surface roughness and deposition rate decreased, whereas the hardness of the films increased when a negative bias voltage was applied. These results demonstrate that ion energy has a significant effect on the composition and morphology of plasma deposited DLC films.

The internal and translational energies of gas-phase radicals, SiH and CH, were characterized using laser-induced fluorescence (LIF) for silicon-based (SiH₄/Ar and Si₂H₆/Ar) and carbon-based (CH₄/Ar) plasmas. The average rotational temperatures (Θ_R) of SiH and CH were found in these plasmas as ~ 500 K and ~ 1450 K, respectively, with no obvious dependence on plasma parameters. Modeling of kinetic data yielded average SiH translational temperatures (Θ_T) of ~ 1000 K in the SiH₄/Ar plasmas and average CH Θ_T of ~ 2200 - 2500 K in the CH₄/Ar plasmas at 50 mTorr within the studied range. No clear dependence on the argon fraction was observed in both SiH₄/Ar and CH₄/Ar plasmas. Interestingly, Θ_T of SiH in the Si₂H₆/Ar plasmas decreased from ~ 1000 K to ~ 550 K as the Ar fraction in the plasma increases. This indicated that the translational energy of SiH in Si₂H₆/Ar plasmas has been thermalized with addition of high fraction of Ar gas. In addition, the average

CH Θ_T did change with applied rf power, $\Theta_T = \sim 2050-9050$ K, which suggests Θ_T is associated with the electron temperature in the plasma.

The surface reactivity, R , of CH radicals was measured during plasma deposition of amorphous hydrocarbon films using our imaging of radicals interacting with surfaces (IRIS) technique. IRIS combines spatially-resolved LIF with molecular beam and plasma techniques. The measured surface reactivity of CH is near unity and shows no dependence on the applied rf power, argon fraction, substrate temperature, or substrate bias. From these results, CH was clearly involved in film growth despite its low gas-phase density.

Jie Zhou
Department of Chemistry
Colorado State University
Fort Collins, Colorado 80523
Spring, 2006

ACKNOWLEDGMENTS

I would like to express my most sincere gratitude to my advisor, Professor Ellen R. Fisher, for her outstanding contribution as my mentor in graduate studies. She showed me the direction when I encountered confusion and gave me support when I faced difficulties. Her constant help and inspiration made this work possible.

Thanks must also go to my Fisher group members, past and present: Dr. Ina T. Martin, Dr. Wendy C. Flory, Dr. Michelle L. Steen, Dr. Jianming Zhang, Dr. Dongping Liu, Dr. Patrick R. McCurdy, Dr. Reed A. Ayers, Eli Adams.

Finally, I would like to thank my wife, Liping Yi Elizabeth for the sacrifices she had to make for me to get through five years of graduate school. My beloved daughter, Elizabeth Y. Zhou, brings me happiness. My parents, Huirong Wang and Zhenhua Zhou, always see values in me and give me confidence. My brothers Yue Zhou and Ye Zhou, care about every bit of my happiness and sadness. It would be impossible for me to accomplish anything without their affection and support.

DEDICATION

This work is dedicated to my wife, Liping Yi Elizabeth, for standing by me through the hard times during the past five years of graduate school. I could not have done it without her.

TABLE OF CONTENTS

ABSTRACT OF DISSERTATION	iii
ACKNOWLEDGMENTS	vi
DEDICATION	vii
TABLE OF CONTENTS	viii
TABLE OF ABBREVIATIONS	xii
CHAPTER 1. Introduction and Overview	1
1.1. Introduction	2
1.2. Plasma fundamentals	3
1.3. Plasma enhanced chemical vapor deposition	5
1.4. Plasma diagnostics during deposition	6
1.4.1. Plasma gas-phase physics	6
1.4.2. Energy partitioning of gas-phase species	8
1.4.3. Plasma-surface interactions	9
1.5. Overview of research	9
References	13
CHAPTER 2. Experimental Methods	16
2.1. Surface characterization methods	17
2.1.1. Plasma polymerization of polypyrrole	17
2.1.2. Au nanotube synthesis	19

2.1.3. Plasma reactor for diagnostics and DLC film deposition	21
2.1.4. Fourier transfer infrared spectroscopy	24
2.1.5. Scanning electron microscopy	25
2.1.6. X-ray photoelectron spectroscopy	25
2.1.7. UV-Vis spectroscopy	25
2.1.8. Cyclic voltammetry	26
2.1.9. Atomic force microscopy	26
2.1.10. Hardness measurements	26
2.2. Diagnostics of plasma gas-phase physics	26
2.2.1. Mass spectrometry	26
2.2.2. Langmuir probe measurements	29
2.3. Gas-phase energetics of radicals and radical-surface interactions	32
2.3.1. IRIS data collection	32
2.3.2. Reactivity measurements	36
2.3.3. Rotational temperature measurements	37
2.3.4. Speed and translational temperature measurements	39
References	44
CHAPTER 3. Synthesis and Properties of Plasma-Polymerized Polypyrrole/Au	
Composite Nanofibers	47
3.1. Introduction	48
3.2. Results and discussion	50
3.2.1. Spectroscopic analysis of PPPy films	50
3.2.2. Gas-phase analysis of pyrrole plasmas	58
3.2.3. Morphology	60

3.2.4. Cyclic voltammetry	64
3.3. Summary	66
References	68
CHAPTER 4. Investigation of Inductively Coupled Ar and CH₄/Ar Plasmas and the Effects of Ion Energy on DLC Film	71
4.1. Introduction	72
4.2. Results and discussion	74
4.2.1. Argon	75
4.2.2. CH ₄ /Ar mixture	83
4.2.3. Effects of ion energy on the properties of DLC film	93
4.3. Conclusions	101
References	103
CHAPTER 5. Effects of Argon Dilution on the Translational and Rotational Temperature of SiH in Silane and Disilane Plasmas	106
5.1. Introduction	107
5.2. Results	109
5.3. Discussion	119
5.4. Summary	125
References	126
CHAPTER 6. Surface Reactivity and Energy Energetics of CH Radicals during Plasma Deposition of Hydrogenated Diamond-like Carbon Films	129

6.1. Introduction	130
6.2. Results	133
6.2.1. Spectroscopy	133
6.2.2. Radical-surface interaction	133
6.2.3. Translational and rotational temperature	137
6.3. Discussion	147
6.4. Summary	152
References	154
CHAPTER 8. Research Summary	157
References	162

TABLE OF ABBREVIATIONS

PPPy	plasma-polymerized polypyrrole
PPy	polypyrrole
ITO	indium tin oxide
DLC	diamond-like carbon
PECVD	plasma enhanced chemical vapor deposition
PVD	physical vapor deposition
CVD	chemical vapor deposition
CCP	capacitively coupled plasma
ICP	inductively coupled plasma
rf	radio frequency
<i>P</i>	applied rf power
CW	continuous wave
FTIR	Fourier transform infrared spectroscopy
XPS	X-ray photoelectron spectroscopy
CV	cyclic voltammetry
SEM	scanning electron microscopy
AFM	atomic force spectroscopy
RMS	root-mean-square

MS	mass spectroscopy
FWHM	full width at half maximum
IED	ion energy distribution
EEDF	electron energy distribution function
n_e	electron density
n_i	ion density
T_e	electron temperature
V_p	plasma potential
λ_D	Debye length
V_f	floating potential
LIF	laser induced fluorescence
IRIS	imaging of radicals interacting with surfaces
ICCD	intensified charge coupled device
Θ_R	rotational temperature
Θ_T	translational temperature
V_{sub}	substrate potential
T_s	substrate temperature
S	scatter coefficient
R	surface reactivity

CHAPTER 1

INTRODUCTION AND OVERVIEW

This dissertation chapter provides an introduction to plasma fundamentals and plasma enhanced chemical vapor deposition (PECVD). The basics of plasma gas-phase diagnostics and plasma-surface interactions are also covered. In addition, this chapter contains an overview of the research presented in Chapters 3-6.

1.1. Introduction

Plasma processing of materials is an essential technology for microelectronics fabrication,¹ thin film deposition,² and surface modification.^{3,4} The advantage of using plasmas in these processes is that materials can be deposited, etched or modified at low substrate temperatures (< 675 K).⁵ Electrons, however, can gain significant energy (1-10 eV),² such that active radicals, ions, and excited species can be created via inelastic collisions between electrons and gas molecules. In past years, plasma enhanced chemical vapor deposition (PECVD) has been extensively used in the microelectronic industry for deposition of various thin films^{2,4,5} such as conductive polymers,^{6,7} amorphous hydrogenated silicon films,⁸ and diamond-like carbon films (DLC).⁹

Despite the wide use of plasmas, little is still known about the mechanisms for plasma processing due to the complexity of plasma chemistry in these systems. During plasma deposition processes, radicals and ions have long been considered as the most important species because of their relative reactivities and abundance in these systems. Therefore, a solid understanding of the gas-phase plasma physics and the energy partitioning of these gas-phase species, such as radical translational, vibrational, and rotational energy, and ion energy distributions, is critical for optimization of existing processes and to drive the development of new materials. Recently, more attention has been focused on the characterization and understanding of plasma-material interactions during plasma processing of materials, because the ultimate properties of plasma-prepared materials are controlled by these surface reactions. Understanding how each species influences the surface structure is, therefore, essential for optimizing the plasma processing of materials.

1.2. Plasma fundamentals

A plasma is a partially ionized gas consisting of ions, electrons, metastable species, and neutral species in an electrically quasi-neutral state.^{10,11} When an electrical field is applied to a gas, free electrons are accelerated by the field. Because the mass of an electron is much smaller than that of a neutral species, electrons lose almost no energy during electron-neutral momentum transfer collisions. As a consequence, the free electrons can be accelerated to very high energies, typically several electron volts (1-10 eV average energy),¹² whereas gas molecules have much lower energy. This leads to a “nonequilibrium” or cold plasma in which the electrons do not achieve thermodynamic equilibrium with gas molecules. When electron energies are higher than the threshold energies of inelastic collisions (ionization or excitation), electron-ion pairs and neutral radicals are created by electron impact with neutral species.⁵ Therefore, low-temperature plasmas are widely used to induce chemical reactions at relatively low gas temperatures (< 1000 K), without damage of the underlying substrate.

In the bulk plasma, the electron density and ion density are roughly the same, making the plasma quasi-neutral. Since both electrons and ions are lost on the walls of the plasma reactor due to diffusion, in a small region near the surface (namely the sheath region), both electron and ion densities are lower than those in the bulk plasma region.⁵ Because electrons have higher thermal velocities than ions, electrons reach the surface faster, thereby leaving the plasma with an overall positive charge in the sheath region. An electric field that retards the electrons and accelerates the ions develops in this sheath region in such a way as to make the net current zero. Consequently, the surface potential is more negative relative to the plasma potential.

Therefore, this sheath potential drop provides ions with high energies with which they bombard the surface.

Conventionally, plasmas are electrically created by either capacitive coupling (capacitively coupled plasmas-CCPs) or inductive coupling (inductively coupled plasmas-ICPs). In CCP reactors, a radio frequency (rf) voltage is applied between two electrodes and a power of 50–2000 W then can be transferred to a low-pressure gas to create a plasma. CCPs are usually weakly ionized with a fractional ionization of about 10^{-5} .⁵ The typical operating pressures in CCPs are 10–1000 mTorr, leading to a low-density plasma of 10^9 – 10^{10} cm⁻³ with an electron temperature varying from 1–5 eV.^{5,11} Currently, ICPs are widely used in the semiconductor industry.¹³⁻¹⁸ In these reactors, the power is supplied to the plasma reactor by either a spiral coil sitting on the top of a quartz window, or a multi-turn coil surrounding a tubular reactor through a matching network. The rf current passing through the coil produces oscillating magnetic fields, which sequentially create oscillating electric fields in the reactor. These fields are the power source for plasma formation. Typically, ICPs operate with a fractional ionization of about 10^{-3} at pressures of 0.5–200 mTorr. The plasma density in ICPs is about 10^{11} – 10^{12} cm⁻³ and the electron temperature varies between 2–7 eV.^{5,11} Moreover, a negative self-bias on the substrate can be formed in an ICP reactor by applying another independently controlled rf generator through capacitive coupling to the substrate.^{5,11} Thus, the plasma can be generated by one rf power source through the coil and the degree of ion bombardment on the substrate can be regulated independently by a second power supply on the substrate. Compared with that from the coil, the power supplied to plasmas from a substrate bias is very low, and it does not significantly influence the plasma density.

1.3. Plasma enhanced chemical vapor deposition

PECVD has been extensively used for deposition of a wide variety of thin films, from organic polymers¹⁹⁻²¹ to inorganic films.²²⁻²⁴ These plasma-prepared films have potential applications in microelectronics,²⁵⁻²⁷ biomedical devices,^{28,29} separation membranes,³⁰⁻³² protective coatings,^{25,33,34} pharmaceutical packaging,³⁵ the aerospace industry,^{19,36} and automotive fields.^{19,37} PECVD of organic polymers, especially conjugated polymers, is also called plasma polymerization. The films obtained by plasma polymerization are generally homogeneous, adherent, and pinhole-free with a high degree of crosslinking and branching.³⁸ The properties and composition of plasma-deposited polymers can be controlled by plasma parameters, such as power input, monomer flow rate, pressure, substrate position, and substrate temperature. Despite the increasing use of plasma polymerization, the underlying mechanisms are still not well understood because of the complexity of plasma chemistry. It was recently reported, that, under low plasma power input conditions, a polymer created by PECVD retains most of the aromatic ring structure of the starting monomer and resembles a more conventionally synthesized polymer.^{38,39} Moreover, pulsing the applied electric field during plasma polymerization can lead to structurally well-defined polymer repeat units, which is attributed to the minimal fragmentation of the monomer and very little damage of the growing film by incident plasma species during the duty cycle on-period, followed by conventional polymerization mechanisms proceeding during the off-period.³⁹

PECVD has also been used for deposition of various inorganic thin films, such as hydrogenated amorphous silicon (a-Si:H),⁸ titanium oxide,²² and SiO₂ films.⁴⁰ Compared with other deposition methods, such as physical vapor deposition (PVD), and chemical vapor deposition (CVD), PECVD methods are attracting great interest

because they can be performed at relative low substrate temperature ($< 600\text{ }^{\circ}\text{C}$), provide good step coverage, and have easy control of reaction parameters.^{5,15,40} In addition, PECVD processes can deposit materials with properties that a thermal CVD process can not because ion bombardment of the substrate can be easily tuned. The high ion energy increases film density and affects the amount and type (tensile or compressive) of film stress.⁴⁰

1.4. Plasma diagnostics during deposition

During plasma processing of materials, control of the characteristics of the prepared materials is a crucial issue, which is accomplished not only by characterization of prepared materials, but also by precise measurement of the processing plasma. The ultimate properties of prepared thin films or modified material surfaces strongly depend upon the plasma parameters used during the processing. Therefore, the diagnostics of the processing plasma is an important technology in the plasma processing of materials. Since a large number of variables affect the ultimate material properties via competing chemical and physical processes in plasmas, it is not easy to fully understand the overall processes, even for the plasmas with relatively simple gas-phase compositions. Appropriate reliable diagnostic techniques are, therefore, necessary to provide an understanding of the plasmas and actual phenomena occurring, which in turn will enable control of the overall process. In this section, an overview of commonly used plasma diagnostic techniques during materials processing will be covered.

1.4.1. Plasma gas-phase physics. As noted in Section 1.2, a plasma is produced by the dissipation of electrical power to the medium in a low pressure gas. Electrons, to which most of the power is transferred, obtain enough energy to initiate excitation,

ionization, and dissociation processes via collisions with atoms and molecules. Atoms, radicals, and ionic species are initially created in this process and can be the origin of further chemical reactions. As a consequence, the plasma phase is usually a very complex mixture of a variety of active species. Therefore, gas-phase physical parameters of plasmas, such as electron and ion density, electron temperature, plasma potential, electron energy distribution function (EEDF), and ion energy are critical to understand the overall plasma process.

To measure electron and ion density, plasma potential, electron temperature, and EEDF, a Langmuir probe is the most often used tool in low-pressure plasmas. This method was developed by Irving Langmuir and his co-workers in the 1920s and has since been further developed to extend its applicability to more general conditions than those presumed by Langmuir.⁵ There are many theories and textbooks where practical usage of the probes is explained.^{5,41} Briefly, a potential scan is conducted on a metal probe inserted in a plasma to draw electron and ion saturation current (V - I characteristics). The electron density, ion density, plasma potential, and EEDF can be derived from this V - I curve. Probes are usually quite small to prevent large perturbations of the plasma.

For full understanding of the gas-phase plasma, radical density, ion density, and ion energy have to be measured because these parameters strongly affect the properties of prepared materials or modified surfaces. It was reported that in fluorocarbon plasmas used for etching Si and SiO₂, the dominant process can vary from fluorocarbon deposition at low ion energy to etching at high ion energy.⁴² Mass spectrometry is a suitable technique to obtain these parameters for low-temperature plasmas with high detection sensitivity. Plasma diagnostics with a mass spectrometer are usually performed by sampling plasma species (ions and neutrals) through a

sampling aperture located at or near the wall of the plasma reactor. After extraction from the plasma, the fluxes of these species are mass analyzed. Moreover, with suitable ion optics, either positive or negative ions can also be analyzed. In such cases, the filament of the ion source is turned off, and suitable voltages are applied to the ion optics.¹¹ The ion energy distribution function (IEDF) then can be measured individually for each selected ion.

1.4.2. Energy partitioning of gas-phase species. Rates of processes occurring in the gas phase and on the surfaces strongly depend upon the energies of the interacting species, i.e., translational and internal energies (rotational and vibrational). Moreover, the gas-phase density of these species is also important to understand mechanisms of film growth, etching, and modification. Spectroscopic techniques are ideally suited for determining the quantum state distributions of species such as radicals and molecular ions. Among various optical techniques, optical emission spectroscopy (OES) provides information on density, vibrational and rotational temperatures of plasma-generated species. However, it lacks spatial resolution and only provides information about the excited state species, which are usually not critical to the overall chemistry because their number densities are several orders of magnitude smaller than those of ground state species.⁴³ Laser-induced fluorescence (LIF) has been used to measure plasma species in ground states. Compared with OES, LIF is sensitive, selective, and spatially resolved. With this technique, the internal energies of species usually can be obtained by comparing the experimental excitation spectrum with a calculated spectrum. Furthermore, the translational energy of radicals extracted from a plasma can be measured by LIF combined with molecular beam techniques.⁸

1.4.3. Plasma-surface interactions. Extensive research has focused on plasma-surface interactions because the ultimate properties of plasma processing materials depend upon the reactions between the gas-phase species and the surfaces of materials. The combination of plasma gas-phase diagnostics and surface analysis is usually the best strategy to understand plasma-surface interactions. Such characterization of gas-phase plasma species as well as molecules generated at the substrate surface during plasma processing can be achieved with our “imaging of radicals interacting with surfaces (IRIS)” technique.⁴⁴ This method combines molecular beam and plasma technologies with spatially resolved LIF to measure radical-surface interactions during plasma processing of a substrate. Reactivity measurements can be made by varying various parameters, such as applied rf power, pressure, substrate temperature, and substrate material. In addition, the effects of ion energy on the surface reactivity of radicals can be also explored with the IRIS technique by applying different substrate biases.⁴⁴

1.5. Overview of research

The principle goal of this work is to understand the mechanisms occurring in both the plasma gas phase and at the substrate surface during the plasma polymerization of polypyrrole and deposition of hydrogenated amorphous silicon, carbon films, including diamond-like carbon (DLC) films. The diagnostics of gas-phase physical parameters, such as electron temperature, electron and ion density, plasma potential, and ion energy, are necessary to fully understand these non-equilibrium, complex plasmas and to offer a good model for these systems. Moreover, characterization of both gas-phase properties and plasma-surface interactions for key species in these plasmas, such as SiH and CH radicals, is a critical component of the

existing research. Of a variety of analytical techniques, LIF is suitable technique to characterize SiH and CH radicals, which allows a more complete mechanistic study of these deposition systems because SiH and CH radicals are quite important species during the film growth processes.

Chapter 2 provides the experimental details for the surface analyses, gas-phase diagnostics, and plasma-surface interactions used in this work. The physical and chemical properties of plasma-deposited films are investigated using several analytical methods, including Fourier-transform infrared (FTIR) spectroscopy, x-ray photoelectron spectroscopy (XPS), scanning electron microscopy (SEM), UV-Vis spectroscopy, cyclic voltammetry (CV), atomic force microscopy (AFM), and nanoindentation. Mass spectrometry (MS), Langmuir probe, and LIF are used to investigate the gas-phase physics and chemistry of plasmas, such as plasma density, ion energy, radical density, and radical energy participation. Our IRIS technique is also used to study the net steady-state surface reactivity of molecules during bombardment of the substrate by the full range of plasma species.

One project included in this work involved the template synthesis of gold nanotubes and subsequent coating by plasma polymerization of polypyrrole. Nanostructured composites have many potential applications in microelectronics, chemical sensors, and electrochemical energy production.²⁰ Chapter 3 describes the chemical, structural, and electrochemical characteristics of a nanostructured composite material prepared from plasma-polymerized polypyrrole (PPPy) coated Au nanotubes. The effects of the duty cycle of a pulsed plasma and the annealing process on the physical and chemical properties of the PPPy films were investigated using FTIR, XPS, UV-Vis spectroscopy, and SEM. The influence of surface area on the electrochemical properties of PPPy films was explored by coating PPPy films onto the

surface of Au nanotubes. The composition of the pyrrole plasma gas-phase was characterized by MS to understand the mechanisms of plasma polymerization in these systems.

Chapter 4 presents diagnostic studies of Ar and CH₄/Ar plasmas during DLC film deposition in an ICP reactor. The gas-phase plasma diagnostics combined with the surface analysis of DLC films were utilized for elucidating the mechanisms of DLC film growth. A Langmuir probe was used to measure the electron density (n_e), ion density (n_i), electron temperature (T_e), plasma potential (V_p) and electron energy distribution function (EEDF). Relative ion intensities, ion energy distributions (IEDs) and mean ion energies were measured by a mass-resolved ion energy analyzer in the molecular beams of Ar and CH₄/Ar plasmas. The effect of ion energy bombardment on the DLC film growth was also explored by controlling the substrate potentials on the silicon wafers. The structural and surface properties of films were characterized by FTIR, SEM, AFM and nanoindentation.

Chapter 5 details studies of the energy partitioning of plasma generated SiH radicals during the deposition of a-Si:H films. The effects of Ar dilution on the translational and rotational temperatures of SiH in effusive plasma molecular beams of SiH₄/Ar and Si₂H₆/Ar plasmas were measured using spatially and temporally resolved LIF techniques. The translational temperatures were derived from the speed distributions of SiH in the molecular beams of these plasmas, whereas the rotational temperatures were obtained by comparing the experimental excitation spectra with simulated spectra. Interestingly, the translational temperature of SiH is strongly coupled to the Ar dilution in Si₂H₆/Ar plasmas, but not in SiH₄/Ar systems. In both systems, the rotational temperature of SiH is independent of the Ar dilution. These results are discussed with respect to parent gas dissociation mechanisms.

Although the gas-phase density of CH in hydrocarbon plasmas is relative low, it has a significant influence on the quality of plasma-prepared hydrocarbon films, including DLC films.⁴³ The role of CH radicals during the growth of hydrocarbon films, however, is still not well understood. Chapter 6 presents IRIS studies of CH radicals in CH₄/Ar plasmas. The surface reactivity of CH radicals is measured as a function of applied rf power, argon fraction, substrate temperature, and substrate bias. The energy partitioning of CH radicals is also investigated. These results combined with the diagnostic data obtained in Chapter 4 provide deep insight into the roles of CH radicals in the film growth of DLC films.

References

- (1) Ventzek, P. L. G.; Hoekstra, R. J.; Kushner, M. J. *J. Vac. Sci. Technol. B* **1993**, *12*, 416.
- (2) d'Agostino, R. *Plasma Deposition, Treatment, and Etching of Polymers*; Academic Press, INC.: New York, **1990**.
- (3) Inagaki, N. *Plasma Surface Modification and Plasma Polymerization*; Technomic Publishing: Lancaster, PA, **1996**.
- (4) Yasuda, H. *Plasma Polymerization*; Academic Press: Orlando, FL, **1985**.
- (5) Lieberman, M. A.; Lichtenberg, A. J. *Principles of Plasma Discharges and Materials Processing*; Wiley: New York, **1994**.
- (6) Brady, K.; Lau, T.; Megill, W.; Wallace, G. G.; Diamond, D. *Synthetic Metals* **2005**, *154*, 25.
- (7) Zhou, J.; Fisher, E. R. *J. Nanosci. Nanotech.* **2004**, *4*, 539.
- (8) Kessels, W. M. M.; McCurdy, P. R.; Williams, K. L.; Barker, G. R.; Venturo, V. A.; Fisher, E. R. *J. Phys. Chem. B* **2002**, *106*, 2680.
- (9) Takai, O.; Anita, V.; Saito, N. *Surf. Coat. Technol.* **2005**, *200*, 1106.
- (10) Hollahan, J. R.; Bell, A. T. *Techniques and Applications of Plasma Chemistry*; Wiley: New York, **1974**.
- (11) Grill, A. *Cold Plasma in Materials Fabrication from Fundamentals to Applications*; The Institute of Electrical and Electronics Engineers, Inc.: New York, **1994**.
- (12) Morosoff, N. *Plasma Deposition, Treatment, and Etching of Polymers*; Academic Press: San Diego, **1990**.

- (13) Carter, J. B.; Holland, J. P.; Peltzer, E.; Richardson, B.; Bogle, E.; Nguyen, H. T.; Melaku, Y.; Gates, D.; Ben-Dor, M. *J. Vac. Sci. Technol. B* **1993**, *11*, 1301.
- (14) Barnés, M. S.; Foster, J. C.; Keller, J. H. *Appl. Phys. Lett.* **1993**, *22*, 2622.
- (15) Lee, J. J. *Surf. Coat. Technol.* **2005**, *200*, 31.
- (16) Song, H.; Zhao, Y. N.; Yu, X. *Thin Solid Films* **2005**, *489*, 164.
- (17) Kim, K. N.; Jung, S. J.; Yeom, G. Y. *Surf. Coat. Technol.* **2005**, *200*, 784.
- (18) Kim, G.; Kim, C.; Efremov, A. M. *Vacuum* **2005**, *79*, 231.
- (19) Silverstein, M. S.; Chen, R.; Kesler, O. *Polym. Eng. Sci.* **1996**, *36*, 2542.
- (20) Tran, N. D.; Dutta, N. K.; Choudhury, N. R. *Thin Solid Films* **2005**, *491*, 123.
- (21) Wang, J.; Neoh, K. G.; Kang, E. T. *Thin Solid Films* **2004**, *446*, 205.
- (22) Maeda, M.; Watanabe, T. *Thin Solid Films* **2005**, *489*, 320.
- (23) Voulgaris, C.; Panou, A.; Amanatides, E.; Mataras, D. *Surf. Coat. Technol.* **2005**, *200*, 351.
- (24) Stelzner, T.; Arold, M.; Falk, F.; Stafast, H.; Probst, D.; Hoche, H. *Surf. Coat. Technol.* **2005**, *200*, 372.
- (25) Wrobel, A. M.; Wertheimer, M. R.; Dib, J.; Schreiber, H. P. *J. Macromol. Sci. Chem. A* **1980**, *14*, 321.
- (26) Bruno, G.; Capezzuto, P.; Cicala, G. *Pure Appl. Chem.* **1992**, *64*, 725.
- (27) Haque, Y.; Ratner, B. D. *J. Polym. Sci., Part B, Polym. Phys.* **1988**, *22*, 1237.
- (28) Park, S. Y.; Kim, N. *J. Appl. Polym. Sci., Appl. Polym. Symp.* **1990**, *46*, 91.
- (29) Limb, J. S.; Edell, J. D.; Gleason, F. E.; Gleason, K. K. *J. Appl. Polym. Sci.* **1998**, *67*, 1489.
- (30) Weichart, J.; Mueller, J. *J. Membr. Sci.* **1994**, *86*, 87.
- (31) Weichart, J.; Mueller, J. *Surf. Coat. Technol.* **1993**, *59*, 342.

- (32) Silverstein, M. S.; Zuri, L.; Narkis, M. *Polym. Prepr. (Am. Chem. Soc., Div. Polym Chem.)* **1997**, *38*, 1000.
- (33) Petasch, W.; Baumgaertner, K.; Raeuchle, E.; Walker, M. *Surf. Coat. Technol.* **1993**, *59*, 301.
- (34) Sadhir, R. K.; Saunders, H. E.; Bennett, A. I. *J. Appl. Polym. Sci., Appl. Polym. Symp.* **1990**, *46*, 209.
- (35) Lamendola, R.; d'Agostino, R. *Pure Appl. Chem.* **1998**, *70*, 1203.
- (36) Hozumi, A.; Takai, O. *Thin Solid Films* **1998**, *334*, 54.
- (37) Morra, M.; Occhiello, E.; Garbassi, F. *J. Appl. Polym. Sci.* **1993**, *48*, 1331.
- (38) Hu, X.; Zhao, X.; Uddin, A.; Lee, C. B. *Thin Solid Films* **2005**, *477*, 81.
- (39) Spanos, C. G.; Badyal, J. P. S.; Goodwin, A. J.; Merlin, P. J. *Polymer* **2005**, *46*, 8908.
- (40) Rogers, B. R.; Cale, T. S. *Vacuum* **2002**, *65*, 267.
- (41) Pfau, S.; Tichy, M. *Langmuir Probe Diagnostics of Low-temperature Plasmas*; Wiley-VCH: Berlin, **2001**.
- (42) Cardinaud, C.; Peignon, M. C.; Tessier, P. Y. *App. Surf. Sci.* **2000**, *164*, 72.
- (43) Luque, J.; Juchmann, W.; Jeffries, J. B. *Appl. Opt.* **1997**, *36*, 3261.
- (44) Fisher, E. R. *Plasma Process. Polym.* **2004**, *1*, 13.

CHAPTER 2

EXPERIMENTAL METHODS

This dissertation chapter contains three main sections, which describe the methods by which data discussed in the following chapters were collected. The first section of this chapter describes our plasma reactors used to deposit polypyrrole and DLC films, as well as common surface analysis techniques. The second section of this chapter provides a detailed description of gas-phase diagnostic methods. The third section of this chapter describes the imaging of radicals interacting with surfaces (IRIS) technique, which was used to characterize gas-phase and surface properties of plasma radicals.

2.1. Surface characterization methods

2.1.1 Plasma polymerization of polypyrrole. Plasma polymerization reactions were carried out in a home-built tubular glass inductively coupled (13.56 MHz) rf plasma reactor, Figure 2.1.¹ The reactor consisted of two cylindrical Pyrex tubes held together by a 50 mm o-ring joint and a Thomas pinch clamp. Glass sleeves were employed to reduce deposition on the reactor walls. An 8 ½ turn, 10 gauge nickel-coated copper wire was used for the inductor coil. Gases were introduced through a single ¾ inch port located directly in front of the inductor coil. Gas products were removed from the system through a liquid N₂ cold trap by an Alcatel 2012A mechanical pump at a speed of 4.2 Ls⁻¹. Power was supplied to the inductor coil by an Advanced Energy RFPP 5s power supply, which has a 13.56 MHz power range of 0-500 W. Films were deposited on substrates placed in the downstream of the reactor 3 cm away from the right end of the inductor coil. Substrates used were either KBr pellets for Fourier transfer infrared spectroscopy (FTIR) or indium tin oxide (ITO) conducting glass working electrodes for cyclic voltammetry (CV). Pyrrole (Acros, C₄H₅N=67.09 g/mol, 99%; boiling point: 129 °C at 760 mmHg; modified Reid vapor pressure: 0.25 p.s.i. (± 0.05)) was purified several times before use by the freeze-pump-thaw method to remove any residual gases dissolved in the pyrrole. Plasma polymerization of pyrrole was performed for 5 minutes using a peak applied rf power, $P_p = 130$ W, a 10% duty cycle (the ratio of on time to total cycle time multiplied by 100) and a system pressure of 110 mTorr (as monitored with a MKS Baratron capacitance manometer). The continuous wave (CW) equivalent power of the plasma is the product of the duty cycle and P_p ; thus, a 10% duty cycle with $P_p = 130$ W corresponds to an equivalent CW power of 13 W. Following film deposition, substrates were removed from the chamber for analysis. For comparison to annealed

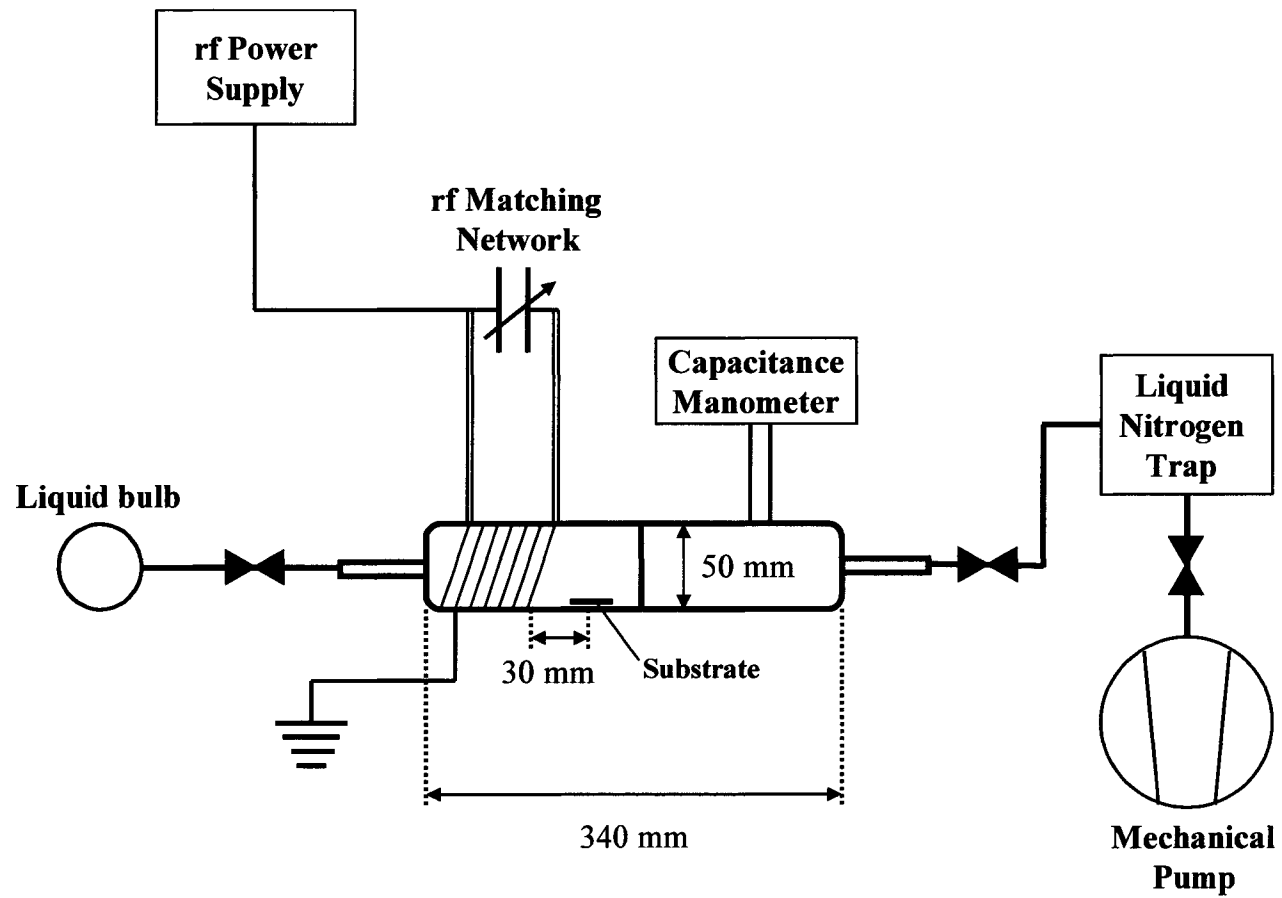


Figure 2.1. Schematic of the plasma reactor used for deposition of polypyrrole film.

films, some plasma-polymerized polypyrrole (PPPy) films underwent thermal treatment for 1 hour at 300 °C under a nitrogen atmosphere.² The films were weighed before and after thermal treatment to determine if significant weight loss has occurred. Following thermal treatment, films experience only ~0.1-0.2% weight loss, indicating the films are mostly intact following treatment.

2.1.2 Au nanotube synthesis. Polyester track-etch membranes (Whatman Company) were used to form the Au nanotubes in this work. Although different porous media can be considered, track-etch templates have several advantages partially linked to their production process. This track-etch method entails bombarding nonporous surface of polymer with energetic heavy ions, to create linear damage tracks in the polymer, and then chemically etching these tracks into pores.^{3,4} Consequently, randomly distributed cylindrical pores with uniform diameter can be produced on the membranes. Pore sizes can vary from 10 nm to several μm with a length to diameter ratio in the range 10-1000. Pore densities can approach 10^9 pores per square centimeter.⁴ The quality of the etch process depends on the energy deposition density of the ion along its path, on the radiation sensitivity of the polymer, on the storage conditions of the ion-irradiated polymer before etching, and on the etchant. Most important storage factors are the atmosphere in which the material is stored, the temperature and the illumination conditions during storage. For a typical polyester membrane which has a monomer unit of $-\text{OOC-R-COO-R}'-$, main points of etch attack are the partially charged $-\text{COO}-$ ester groups in the damaged zone of a latent track. These weakened ester groups are hydrolyzed by alkalis. During alkaline etching the ordinary bond between carbon and oxygen is broken which produces $-\text{COO}-$ and HO^- at the ends of the formed fragments.⁵

In the present experiment, membranes used for synthesis of Au nanotubes were $\sim 11 \mu\text{m}$ thick, with a pore density of 2×10^7 pores/ cm^2 and pore diameters of 1000 nm and were rinsed in methanol before use. Smaller diameter Au tubes (i.e. 200 nm) have also been produced. Au tubules were synthesized using electroless plating template-synthesis methods described previously.^{4,6-9} This method involves applying a sensitizer, Sn^{2+} , to the membrane surfaces of porous polyester membranes. The sensitizer binds to the surfaces via complexation with surface carbonyl and hydroxyl groups. This sensitized membrane is then activated by exposure to Ag^+ resulting in a redox reaction in which the surface bound Sn^{2+} is oxidized to Sn^{4+} and the Ag^+ is reduced to elemental Ag ($\text{Sn}^{2+}:\text{Ag} = 1:2$). As a result, the pore walls and membrane faces become coated with discrete, nanoscopic Ag particles. The Ag-coated membrane was then immersed in a Au^+ plating bath. The Ag particles are galvanically displaced by Au since gold is more noble metal. Consequently, the pore walls and faces become coated with Au particles. These particles are excellent catalytic sites for the oxidation of formaldehyde and the concurrent reduction of Au^+ to Au. As a result, gold plating continues on the gold particles, with formaldehyde as the reducing agent ($2\text{Au}^+ + \text{HCHO} + 3\text{OH}^- \rightarrow \text{HCOO}^- + 2\text{H}_2\text{O} + 2\text{Au}$), which results in Au plating on the membrane surfaces and pore walls.^{9,10} Finally, this yields a gold microtubule within each pore; Au surface layers also form on both faces of the membrane. The inner Au tubule formation within the pores was performed for 120 minutes at room temperature. One surface layer was removed from the Au plated membrane by polishing with a laboratory tissue dampened with methanol. The resulting Au microtubule-containing membrane was placed on a piece of Cu foil with the intact Au surface layer down. This composite membrane was then immersed in hexafluoroisopropanol (Aldrich) for 3-4 hours to dissolve the polyester membrane,

freeing the ensemble of Au nanotubes, standing upright on the Cu foil. These tubules were placed within the plasma reactor and PPPy films were deposited onto the outer surface of each Au tubule.

2.1.3 Plasma reactor for diagnostics and DLC film deposition. Figure 2.2. is a schematic of the new chamber we constructed for gas-phase analyses of our plasma systems. Film deposition experiments and plasma diagnostics were performed in an inductively coupled plasma reactor mated to the chamber. There are two cylinders inside the plasma reactor; the height and inner diameter of each cylinder are 15 cm and 5.5 cm, respectively. The top cylinder is made by stainless steel and has a shower head structure used as gas inlet. The entire cylinder is grounded all time during the experiments. Plasmas were produced by the inductive coupling of 13.56 MHz rf power (RF5S, Advanced Energy) to an eight-loop induction coil surrounding the bottom glass cylinder through a variable capacitor matching network. Reactant gases, Ar (General Air, 99.99%) and CH₄ (General Air, 99.99%) were used without further purification. For CH₄/Ar plasmas, the flow ratio was fixed at 15:85, and the gases were premixed before entering the plasma reactor through the shower head. All diagnostic experiments were conducted at pressures of 30 mTorr, 40 mTorr and 50 mTorr by varying CH₄ and Ar flow rates, and the P ranged from 30-150 W.

The main chamber is made of aluminum board (thickness = 0.5 in), and is pumped by a 10 in diffusion pump (5300 L/s air, Varian Inc.) with a mechanical backing pump (400 L/min, Alcatel). For all experiments, a base pressure of $\leq 2.0 \times 10^{-6}$ Torr in the main chamber was achieved before collecting any data. The expansion of the plasma into the differentially pumped main chamber takes place sequentially through a 9.75 mm diameter hole at the bottom of the glass reactor and through a metal grid ($1 \times 1 \text{ mm}^2$) attached to the inner wall of the main chamber. This

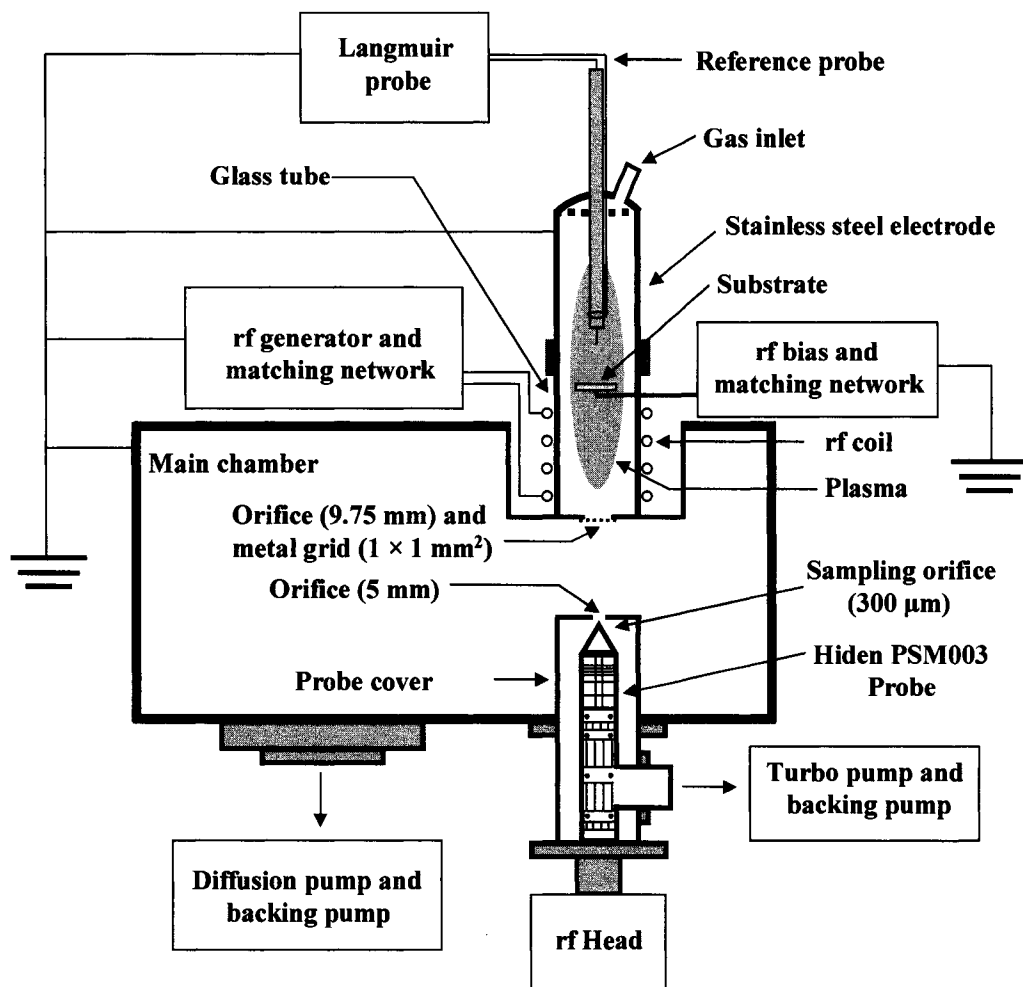


Figure 2.2. Schematic of the experimental apparatus used for plasma diagnostics during the deposition of DLC films. The dimension of main chamber is $622 \times 448 \times 253 \text{ mm}^3$.

leads to a working pressure of $\leq 1.0 \times 10^{-4}$ Torr in the main chamber at all investigated reactor pressures. The metal grid and main chamber were grounded at all times to confine the plasma to the reactor. Ideally, an infinitely small orifice should be used for ion sampling to prevent perturbation of the plasma. Minimum orifice diameters are, however, restricted by the need for sufficient signal. With the present orifice size (9.75 mm), the disturbances to ion energy result primarily from neutral molecule density changes around the orifice. A transition from the higher density of the plasma (≤ 50 mTorr) to the much lower density (10^{-6} Torr) of the chamber occurs around the orifice. In the transition region, the presence of the orifice increases the density of molecules on the downstream side of the orifice and decreases the density of molecules in the plasma near the orifice. This effect increases the possibility of ion-molecule collisions occurring after the ion passes through the orifice.¹¹ Thus, the ion energy may be disturbed from energy exchange via ion-neutral collisions. However, the pressure in the main chamber is $\leq 1.0 \times 10^{-4}$ Torr when the pressure in the reactor is lower than 50 mTorr. This suggests that beyond the transition region, ions will not encounter further collisions in the main chamber due to the relatively long mean free path (> 50 cm).

DLC films were deposited on rf biased substrates in the ICP reactor, as shown in Figure 2.2. An aluminum substrate (25 mm diameter, 3 mm thick) was placed 30 mm below the tip of the Langmuir probe, perpendicular to the axis of the plasma reactor. The substrate was capacitively coupled by an independently controlled 13.56 MHz rf generator (RF5S, Advanced Energy) through a matching network consisting of a combination of two variable capacitors (500 pF, Jennings Inc.) and one inductor. The substrate was not grounded during deposition. This leads to a positive floating potential on the substrate during the deposition when no rf power is applied to the

substrate. In this study, the substrate potential ranges from +50 V to -150 V by varying the input rf power from 0 to 30 W. Silicon (100) wafers (15 mm × 12 mm × 1 mm) were mechanically attached to the substrate surface with good electrical contact between the wafer and substrate. Prior to deposition, the silicon wafers were bombarded with high-energy Ar⁺ using a 110 W Ar plasma with -150 V self-bias voltage for 15 min to remove the native oxide layer on the silicon wafer. To evaluate the effect of ion energy on the properties of DLC films, the applied rf coil power and reactor pressure were fixed at 90 W and 50 mTorr, respectively, to maintain an approximately constant ion flux (small increases of ion flux may be induced by the applied substrate rf powers). More methane rich (CH₄:Ar = 50: 50) mixtures were used to increase the deposition rate of DLC films. The deposition time was 10 min for all films. The substrate temperature increased somewhat from bombardment of energetic ions during deposition. However, the maximum temperature after a 10 min deposition was < 150 °C, which does not significantly influence the properties of DLC films.¹²

2.1.4 Fourier transfer infrared spectroscopy. A Nicolet Magna 760 FTIR spectrometer was used to characterize PPPy and DLC films. For all FTIR measurements, N₂ purging was used to reduce absorption from atmospheric moisture and CO₂. FTIR spectra of PPPy films deposited on KBr pellets were obtained using with 8 cm⁻¹ resolution and 30 scans. For the plasma deposition of DLC films, Si wafers were used as substrates. The hydrogen content in DLC films deposited at different self-biases was evaluated by FTIR spectra (1 cm⁻¹ resolution, 200 scans per spectrum). The final absorbance intensity was normalized by the film thickness to negate the influence of film thickness.

2.1.5 Scanning electron microscopy. SEM images of all materials were obtained using a JEOL JSM-6500F microscope with an accelerating voltage of 5-15 keV. Prior to SEM analysis, the samples were affixed to a standard SEM sample stub by double-sided carbon tapes. To prevent surface charging during SEM analysis, a thin film (5-20 nm thick) of Au was sputtered onto the surface of all samples prior to imaging. In Chapter 4, DLC film thicknesses were determined from SEM cross-sectional images with a 15 keV accelerating voltage.

2.1.6 X-ray photoelectron spectroscopy. XPS analyses were performed on a Physical Electronics PE5800 ESCA/AES system. Spectra were collected using a 2 mm monochromatic Al K_α X-ray source (1486.6 eV), hemispherical analyzer, and multichannel detector. A low energy (~1 eV) electron neutralizer was used for charge neutralization. Survey spectra were collected with a pass energy of 187.85 eV. High resolution C_{1s} and N_{1s} spectra were acquired at an analyzer pass energy of 23.50 eV. Curve fitting was performed using Gaussian functions with the FWHM (full width at half maximum) of ≤ 2.5 eV, which is expected for plasma polymers.¹³ All the binding energies were referenced to the peak of α carbons in the ring of pyrrole at 285 eV. A photoelectron take-off angle of 45° with respect to the sample surface was used for all spectra. The sampling depth is ~ 5 nm at this take-off angle.

2.1.7 UV-Vis spectroscopy. UV-Vis spectra of the PPPy films were obtained on a Varian Cary 500 UV-Vis spectrometer with the samples normal to the probe irradiation. A simple check of the optical activity of our samples was performed by examining changes in the intensity of the light source as a function of sample rotation with respect to a second sample. No change in signal intensity was observed, indicating our samples were not optically active.

2.1.8 Cyclic voltammetry. CV on the PPPy materials was performed using an Epsilon EC potentiostat. The cell was composed of PPPy deposited on an ITO plate ($1 \times 1 \text{ cm}^2$) as the working electrode, a Pt wire counter electrode, and an Ag/AgCl reference electrode. The electrolyte was 0.1 M LiClO₄ in acetonitrile non-aqueous solution.

2.1.9 Atomic force microscopy. The surface roughness of the hydrogenated DLC films was measured using atomic force microscopy (AFM) (Digital Instruments) operated in air in tapping mode. Silicon tips (MikroMasch) with a 40 N/m force constant and 170 kHz resonant frequency were used. The displayed z scale for all images was fixed from 0 to 20 nm, and $2 \times 2 \text{ }\mu\text{m}$ areas were imaged.

2.1.10 Hardness measurements. The hardness and Young's modulus of the DLC films were determined by Nanoindenter XP (MTS Systems Corporation) using a diamond tip (Berkovich), which was operated in dynamic control module (DCM) mode. Replicate indentations (40) were performed on each film sample and the hardness and Young's modulus were calculated from loading curves.

2.2. Diagnostics of plasma gas-phase physics

2.2.1. Mass spectrometry. Mass spectral data of pyrrole plasmas were obtained by a mass spectrometer (Dycor 100) mated to our imaging of radicals interacting with surfaces (IRIS) high vacuum apparatus, Figure 2.3.¹⁴ On this apparatus, a plasma tube nearly identical to the ones used for our polymerization studies is used as the source for a molecular beam, discussed further in Section 2.3.1. For mass spectrometry studies, the mass spectrometer is directly in line with the plasma molecular beam, well downstream of the plasma source ($\sim 20 \text{ cm}$) in a differentially pumped chamber. The mass spectrometer can be operated with or without an ionizing

potential. When the ionizer is on, an accelerating potential of 70 eV was used between the filament and the anode of the mass spectrometer. In this configuration, spectra of all the species in the plasma molecular beam (including neutral and ionic plasma species as well as species resulting from fragmentation in the ionizer) are collected. When the ionizer of the mass spectrometer is turned off, nascent ions generated in the pyrrole plasma are detected.

The mass spectrometer used for IED measurements is also shown in Figure 2.2. The mass spectrometer probe (PSM003, Hiden Analytical Ltd) consists of a combination of ion extractor, electron-impact ion source, Bessel box energy filter, triple-section quadrupole mass filter (QMF) and secondary electron multiplier. The probe is surrounded by an aluminum cylindrical cover with a 5 mm diameter hole in the center of the top surface. The distance between the plasma reactor hole and top surface of the probe cover is 5 cm, which is much less than the mean free path (> 50 cm) in the main chamber under the present operation conditions. To sample ions and neutrals, a vacuum sealed skimmer located 2 mm below the hole of the probe cover was attached to the end of the mass spectrometer. The diameter of the skimmer is 300 μm in the present studies. Ions created in the plasma sequentially pass through the reactor hole, grid, probe cover hole, and sampling orifice, and eventually enter the ion energy analyzer of the mass spectrometer. A base pressure of $\sim 8 \times 10^{-8}$ Torr inside the MS was achieved by using a 60 L/s turbo molecular pump backed by a 400 L/min mechanical pump. With the 300 μm sampling orifice, the pressure in the mass spectrometer probe was maintained at $< 9 \times 10^{-7}$ Torr during experiments, which is much lower than the minimum required pressure (5×10^{-6} Torr) for operating the ion detector. Moreover, the low pressure environment in the mass spectrometer probe increases the mean free path of the sampled species to prevent gas-phase ion-molecule

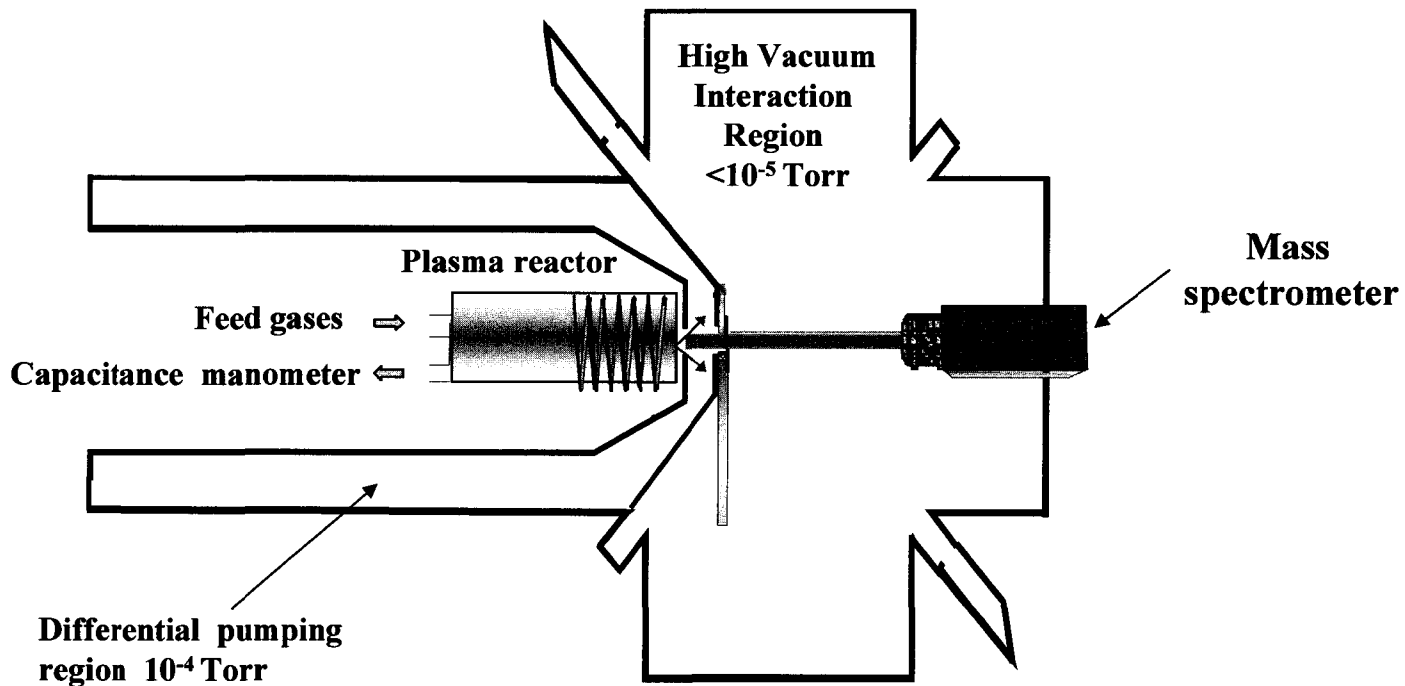


Figure 2.3. Schematic of the molecular beam apparatus used to perform mass spectral experiments.

collisions and ensures that no disturbance of ion energy occurs inside the probe. For ion analysis, the internal ionization source was disabled and the front lenses were used to extract ions from the plasma molecular beam and focus them into the mass filter. The source region is held at the mid axis potential of the gauge. The QMF identifies various ions according to their mass-to-charge (m/z) ratio and the IED is measured individually for each m/q selected ion. Each IED measurement was repeated three times. The rf head which contains the rf generator circuit and the detector amplifier/discriminator was directly mounted on the probe vacuum feedthrough. Power and control signals were fed to the rf head via a series of cables housed in a conduit connecting to the mass spectrometer interface unit (MSIU). The operating settings of each component of the mass spectrometer were computer-controlled by the software 'MASsoft' provided by Hiden Analytical.

2.2.2. Langmuir probe measurements. The experimental arrangement for Langmuir probe measurements is shown in Figure 2.2. A double probe (Smart Probe, Scientific System Ltd) was used in this work to measure the plasma potential (V_p), electron temperature (T_e), electron density (n_e), ion density (n_i), electron energy distribution function (EEDF) and Debye length (λ_D) of Ar and CH₄/Ar plasmas. The Langmuir probe was encased in a cylindrical and hollow alumina tube (470 mm in length). A tungsten wire, 10 mm in length and 0.19 mm in diameter, was used as the probe tip, and located 10 mm below the bottom end of the stainless steel electrode. It was necessary to use a smaller probe tip to minimize perturbation to the local plasma and to draw low current to prevent overheating and melting of the tip.¹⁵ The entire probe was inserted into the plasma reactor along its central axis. A ring shaped reference probe was used to track and compensate any low frequency DC shifts in the plasma potential. A pair of inductors situated close to the probe tip are self-resonant

with their intrinsic capacitance close to the driving rf frequency (13.56 MHz) to compensate for rf variation.¹⁶ During the operation of the probe, a continuous flow of dry air was used to cool the inductors placed inside the probe and the probe holder to prevent overheating by resistive heating or thermal conduction from the probe tip.

Langmuir probe measurements were performed as follows. The sweep voltage applied to the tip started at -95 V and ended at a voltage just above the plasma potential. Therefore, the resulting I-V curve covered the range from the ion saturation current to the electron saturation current. At each bias point, the measurements were performed twenty times to yield one data point. Five cycles of sweeps were then repeated to yield one smooth I-V characteristic. To obtain good measurements, a cleaning routine was conducted by pulse biasing the probe to 100 V. Thus, possible contamination layers on the probe surface were removed by the bombardment of electrons with high kinetic energy. When a I-V scan was started, a clean cycle with a 2 s duration and 2 s interval was performed before the first sweep was acquired and then subsequent cleans were performed at the clean interval period until the I-V scan was completed.

Although Langmuir probes are fairly straightforward to operate, analysis of Langmuir probe data is quite complicated because there is no universal method to interpret the data. In the present study, the data analysis was completed with a data analysis software (SmartSoft) based on well established theories.¹⁷ V_p is determined from the cut-off point on the voltage axis by the second derivative I'' of the I-V curve, i.e. $d^2I/dV^2 = 0$. On the I-V curve, the floating potential (V_f) is the voltage at which the current is equal to zero. The electron temperature is calculated by using the current measured at the plasma potential, $I(V_p)$ and dividing it by the integral of the I-V curve from V_f to V_p , i.e.

$$\frac{I(V_p)}{\int_{V_f}^{V_p} I(V)dv} = \frac{1}{kT_e} \quad (1)$$

The method used here to calculate kT_e is less sensitive to noise than the more common technique of calculating kT_e by dividing $I(V_p)$ by the derivative of the I-V characteristic.¹⁷ The electron number density, n_e , is calculated from the current measured at the plasma potential using following equation:

$$n_e = \frac{I(V_p)}{A_p} \left[\frac{2\pi m_e}{e^2 kT_e} \right]^{1/2} \quad (2)$$

A_p is the area of the probe tip, m_e is the mass of electron, e is the electronic charge and kT_e is the electron temperature in eV. The Debye length, λ_D , which develops around the probe, is calculated from the electron temperature using the equation 3:

$$\lambda_D = \left[\frac{\epsilon_0 kT_e}{e^2 n_e} \right]^{1/2} \quad (3)$$

To measure the ion saturation current, a large negative bias is applied to the probe with respect to the plasma potential. The sheath which develops around the probe tip expands when a voltage is applied. To account for this effect, Laframboise theory is used to calculate the ion density (n_i^+).¹⁷ First, the ion current can be roughly described by:

$$I_+ \approx \alpha_+ \left[\frac{V - V_p}{kT_e} \right]^{\gamma_+} I_{+th} \quad (4)$$

where α_+ and γ_+ are sheath expansion factors depending on the ratio between the radius of the probe r_p and the Debye length λ_D and I_{+th} is the ion thermal current, defined as:

$$I_{+th} = en_i^+ \left[\frac{kT_e}{2\pi m_i^+} \right]^{1/2} A_p \quad (5)$$

The expansion factors α_+ and γ_+ are obtained by calculating the ion thermal current at a default voltage of -50 V. At this voltage, the collection of highly energetic electrons can be neglected:

$$I_{+th} = \frac{I(I_{onvoltage=-50V})}{\alpha_+ \left[\frac{V - V_p}{kT_e} \right]^{\gamma_+}} \quad (6)$$

The ion density is further estimated by:

$$n_i^+ = \frac{I_{+th}}{A_p} \left[\frac{2\pi m_i^+}{e^2 kT_e} \right]^{1/2} \quad (7)$$

where $m_i^+ = 40$ is used to calculate the ion density in argon plasmas and the mass of the most dominant ion is used in calculating n_i^+ in CH₄/Ar plasmas. Electron energy distribution functions, $n(\varepsilon)$ expressed in cm⁻³eV^{-3/2}, yield information on the energy available for excitation or ionization of the discharge gas. The EEDFs in the present study are not fully Maxwellian and best described by a Druyvesteyn distribution,

$$n(\varepsilon) = n_e f(\varepsilon) = \frac{2I_e''}{eA_p} \left[\frac{2m_e \varepsilon}{e} \right]^{1/2} \quad (8)$$

where the energy $\varepsilon = V - V_p$, V is the applied bias voltage to the probe tip; I_e'' is the second derivative of the electron current with respect to the electron energy ε ; $f(\varepsilon)$ is the normalized EEDF. During the EEDF measurements, I_e'' of the I-V characteristic is calculated numerically and averages over 1000 current values at each point on the I-V curve.

2.3. Gas-phase energetics of radicals and radical-surface interactions

2.3.1. IRIS data collection. The IRIS apparatus, Figure 2.4, has been described in detail previously.¹⁸⁻²¹ Briefly, a combination of molecular beam techniques and

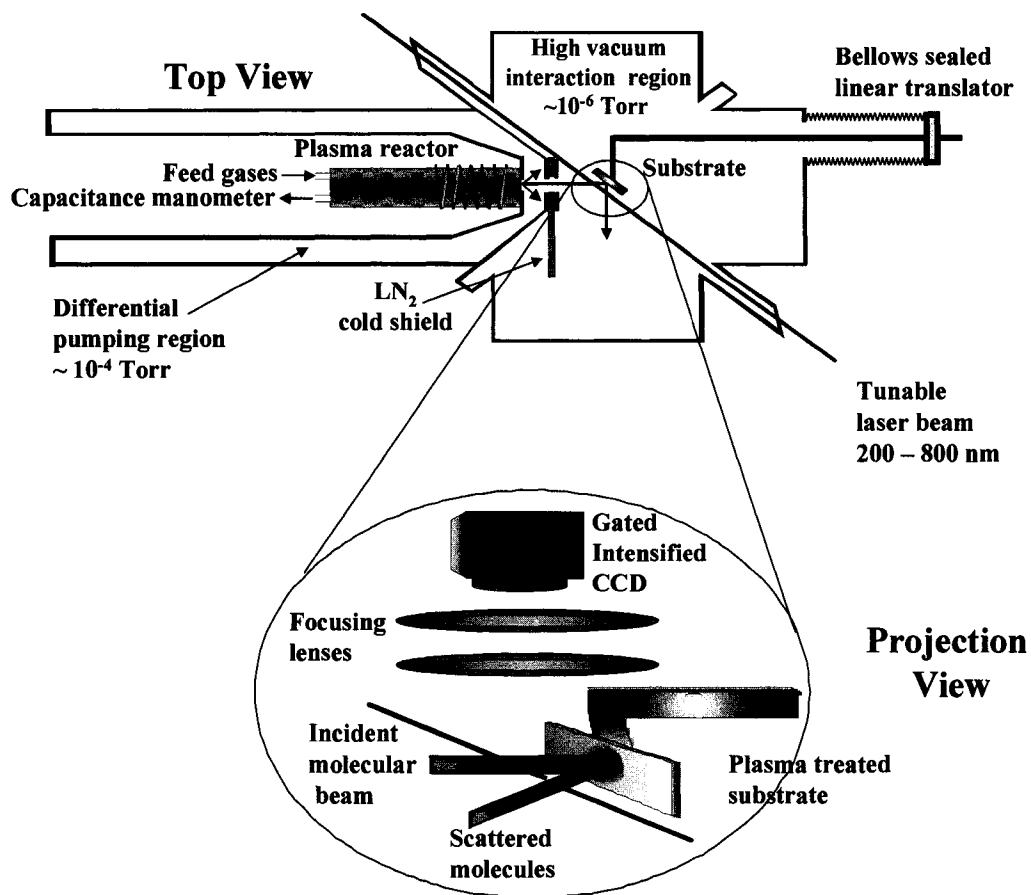


Figure 2.4. Schematic of the IRIS apparatus. The ICCD camera is located perpendicular to the plane of intersection and directly above the interaction region. Spectral scattering of the molecules off the substrate is illustrated.

laser-induced fluorescence has been used to investigate the steady state surface reactivity of gas-phase species during plasma processing of a surface, as well as the gas-phase energetics of the species as a function of different plasma parameters, such as applied rf power, pressure, and gas composition. In a typical IRIS experiment, the feed gases enter the rear of a glass reactor tube, 13.56 MHz rf power is applied to an inductor coil and a plasma is produced. Expansion of the plasma through a series of collimating slits into a differentially pumped high vacuum chamber generates an effusive molecular beam consisting of virtually all species present in the plasma, including the species of interest. Using spatially and temporally resolved LIF allows the study of either the interaction of the radicals with surfaces or the speed of the radicals in the molecular beam. For reactivity measurements, the LIF intensity of a freely expanding molecular beam is compared with the LIF intensity of a molecular beam that is directed onto a substrate. The difference in LIF intensity is directly proportional to the amount of radicals scattered and/or created at the substrate's surface. For speed measurements, "snapshots" of the LIF intensity of a freely expanding molecular beam are taken at different delays after the laser excitation pulse. The speed of radicals can subsequently be deduced from the spatial movement in maximum intensity of the fluorescence between the different delays.

A tunable excimer-pumped (Lambda Physik LPX210i, XeCl, 100 mJ/pulse, 100 Hz) dye laser beam intersects the plasma molecular beam at either 45° or 90° downstream from the plasma source and excites SiH or CH radicals, depending on the plasma system. A lens is used to focus the laser radiation at the position of the molecular beam, yielding a well-defined laser beam < 1 mm wide. Spatially and temporally resolved LIF signals are collected by an electronically gated, intensified charge coupled device (ICCD) located perpendicular to both the molecular and the

laser beam, directly above the interaction region. SiH and CH fluorescence was collected by a set of two lenses, with focal lengths of 300 and 75 mm, imaging a 2664 mm² area onto the 512 × 512 pixel array of the ICCD. For CH measurements, a 8 nm bandwidth interference filter centered at 425 nm was placed between the ICCD camera and the vacuum chamber to reduce spurious signals from scattered laser light and plasma emission. No interference filter was used for the SiH measurements.

The plasma is produced by the inductively coupling of 13.56 MHz rf power (20-200 W) to an eight-loop induction coil surrounding the glass plasma reactor and tuned by a variable capacitor matching network. In Chapter 5, the total pressure was maintained at 50 mTorr for the SiH₄/Ar and Si₂H₆/Ar mixtures. Silane (Voltaix, 99.999%), disilane (Voltaix, 99.99%) and argon (Air Products, 99.999%) were used as feed gases. For mixtures, the fraction of SiH₄ or Si₂H₆ is defined as the ratio of the flow rate of SiH₄ or Si₂H₆ to the flow rate of Ar. For all experiments, the applied rf power was 60 W. Exalite 417 dye (Exciton) was used in the dye laser to probe the SiH A²Δ-X²Π transition. The output laser energy with this dye was typically 3-7 mJ/pulse. Rotational lines Q₁ (*J* = 10.5) at 413.418 nm and R₂ (*J* = 2.5) at 413.428 nm were used for the rotational temperature measurements because the relatively large difference in rotational quantum number means the relationship between these two peaks is sensitive to Θ_R. The R₁₂ (*J* = 1.5) rotational line at 414.438 nm was used for translational temperature measurements because of its higher LIF intensity. Measurements of the SiH LIF signal intensity as a function of laser energy yielded typical optical saturation behavior. All reactivity and speed experiments were performed at laser energies in the optical saturation regime such that the measurements are not affected by small fluctuations in laser power.

In Chapter 6, the source of the molecular beam is a plasma consisting of either 100% CH₄ (General Air, 99.9%) or CH₄/Ar (General Air, 99.9%) mixtures with Ar fractions of 0-20%. The total gas flow was maintained at 30 sccm leading to source pressures of 45-55 mTorr. The molecular beam was collimated by two slits, 1.08 and 1.23 mm wide, with the second slit 12 mm downstream from the first one. Coumarin 440 (Exciton) was used to excite the CH A²Δ ← X²Π transition. For reactivity and speed measurements, the laser was tuned to 430.404 nm (~12 mJ/pulse), corresponding to the R₁(J=1) rotational line of the CH A²Δ ← X²Π transition.

2.3.2. Reactivity measurements. For CH reactivity measurements, the laser radiation is directed into the chamber such that it intersects the molecular beam at a 45° angle, Figure 2.4. A substrate (25 × 40 mm² p-type Si wafer with the polished side facing the molecular beam) can be rotated into the path of the molecular beam with its surface parallel to the laser beam. The laser-surface distance is maintained at ~3 mm. LIF signals are collected with the surface out of and in the path of the molecular beam. Comparisons between the spatial distribution of scattered and incident molecules are used to determine the surface reactivity of the species of interest. A gate width of 2000 ns was used such that the fluorescence is collected over the entire radiative lifetime of the CH A²Δ state (538 ± 5 ns).²² The pixels were 4 × 4 binned to increase the signal-to-noise ratio. Each image consists of 6000 laser pulses. Multiple sets of data were taken with the surface alternating in and out of the molecular beam path. Background images were taken with the laser tuned to an off-resonance wavelength (430.2 nm) and subtracted from each image. Subsequently, the image with the surface out of the molecular beam path is subtracted from the image with the surface in, yielding the signal resulting from scatter of CH at the substrate surface. One-dimensional cross sections were formed by averaging 15 pixel columns

along the laser axis and plotting signal intensity as a function of distance along the laser path.

Spatially resolved LIF data are interpreted using a quantitative model of the experiment that produces the surface reactivity of the CH radicals. The simulation program has been described in detail previously.^{18,20} The model is based on the known geometry of the experiment and calculates the spatial distribution of the radical number density in the molecular beam at the interaction region as well as the radical number density along the laser beam for molecules scattering from the substrate surface. The scattering coefficient, S , defined as the ratio of the flux of scattered molecules to that of the incident beam, is adjusted to best fit the experimental data. The surface reactivity, R , is defined as $1-S$.

2.3.3. Rotational temperature measurements. The rotational temperatures of SiH and CH were measured by collecting SiH and CH fluorescence excitation spectra with the ICCD images 4×4 binned to increase the signal-to-noise ratio. The gate delay and gate width of the ICCD camera were set at 205 ns and 2000 ns, respectively. These settings allow for the collection of fluorescence over the entire radiative lifetimes of the $A^2\Delta$ states of SiH (534 ns)²³ and CH (538 ns).²² The rotational temperature of SiH is deduced from the relative height of the neighboring Q_1 ($J = 10.5$) and R_2 ($J = 2.5$) rotational lines at 413.40 nm and 413.45 nm, whereas Θ_R of CH is deduced from the relative height of the neighboring R_2 ($J=1$) and Q_1 ($J=14.5$) rotational lines at 430.042 and 430.067 nm. The excitation LIF spectra of SiH and CH were scanned with a laser step size of 0.001 nm in wavelength, and 1500 and 1000 laser shots per step for SiH and CH, respectively. The final Θ_R is determined from simulations of these rotational lines using the LIFBASE program at different temperatures until a best fit to the experimental data is obtained.²⁴

The measurements of rotational temperatures of molecules using excitation LIF spectra have been discussed previously.²⁵ Briefly, the rotational energy for a diatomic molecule at J th level is quantized as shown in equation 9:²⁶

$$E_r(J) = \frac{\hbar^2}{2I} J(J+1) = \frac{\hbar^2}{2\mu R_e^2} J(J+1) = BJ(J+1) \quad (9)$$

where, I is the rotational moment of inertia; μ is the reduced mass for a diatomic molecule AB, $\mu = m_A m_B / (m_A + m_B)$; R_e is the equilibrium distance between two atoms; J is the rotational angular momentums, $J = 0, 1, 2, \dots$; B is the rotational constant, $B = h/8\pi^2 c \mu R_e^2$ in units of cm^{-1} . The rotational selection rules are: 1. the molecule must have a permanent dipole moment ($\mu \neq 0$); 2. $\Delta J = \pm 1$; 3. $\Delta M_J = 0, \pm 1$, a rule which is important only if the molecule is in an electric or magnetic field.²⁷

The population N_J of the J th level relative to N_0 is obtained from Boltzmann's distribution law:²⁷

$$\frac{N_J}{N_0} = g_J \exp\left(-\frac{E_r(J)}{kT}\right) = (2J+1) \exp(-BJ(J+1)/kT) \quad (10)$$

where, g_J is the degeneracy of the J th level, $g_J = 2J+1$. Since the intensity of absorption of radiation is directly proportional to the number of molecules in the absorbing state, which is, in turn, governed by Boltzmann's distribution,

$$I_J \propto N_J \propto (2J+1) \exp(-BJ(J+1)/kT) \quad (11)$$

where, I_J is the absorbance intensity of the J th level. When an excitation scan is performed in a single vibrational band, the rotational temperature can be determined from the linear plot that relates LIF intensities to the energy of the ground-state rotational levels, equation 10:²⁵

$$I_J = (2J+1) \exp(-E_r(J)/kT) B_{12} \Phi C \quad (12)$$

where, B_{12} is the Einstein absorption constant between levels of the transition; C is an experimental constant; k is the Boltzmann constant; J is the rotational quantum number in the ground state; and ϕ is the fluorescence quantum yield. The final determination of rotational temperatures in the present studies is obtained by performing two-line excitation scans (absorbance intensities are $I_{J_1-J_2}$ and $I_{J'_1-J'_2}$, respectively):²⁵

$$\Theta_R = T_{rot} = -\frac{E_r(J_1) - E_r(J'_1)}{k \ln\left(\frac{B_{12}(J_1 - J_2)\phi_{J_2}g_{J_1}I_{J_1-J_2}}{B_{12}(J_1 - J_2)\phi_{J_2}g_{J_1}I_{J'_1-J'_2}}\right)} \quad (13)$$

where, k is the Boltzmann constant; J and J' refer to the two different transitions; $B_{12}(J_1 - J_2)$, g_{J_1} , ϕ_{J_2} , and $I_{J_1-J_2}$ are the Einstein absorption constant (lower level-higher level), the rotational degeneracy (lower level), the fluorescence quantum yield (higher level), and the absorbance intensity (lower level-higher level) for the J th transition, respectively. To determine the rotational temperatures of SiH and CH, the excitation scans of two neighboring rotational lines were performed. The rotational quantum numbers of these two rotational lines are quite different, which is well suited for the determination of Θ_R because the relative LIF intensities of these two rotational lines are sensitive to small changes in Θ_R .

2.3.4. Speed and translational temperature measurements. The speed measurements in the present studies were conducted in molecular beams formed from plasmas. There are two main types of molecular beams, effusive and supersonic expansion. They are both produced from a bulk gas passing through a small hole into a vacuum. The two types of beams are produced by changing the pressure and the dimension of the hole. An effusive beam is produced when the mean free path in the bulk gas is much larger than the dimensions of the hole. The molecules can therefore

leave the source without collisions with other particles and the energy distribution of the molecular beam is therefore given by the energy distribution of the bulk gas.²⁸ However, a supersonic beam can be created when the mean free path in the bulk becomes smaller than the dimensions of the outlet at higher source pressure. Many collisions then take place as the gas exits the source and expands into vacuum. These collisions result in energy transfer from the perpendicular kinetic energy components to the parallel kinetic component. In the case of molecules, energy will also be transferred from the internal energy modes, rotations and vibrations, to the parallel kinetic component.²⁸

In our IRIS apparatus, the pressure inside the plasma reactor is maintained at ~ 50 mTorr (the mean free path is ~ 1 mm). The plasma is expanded into the first differentially pumped region through a 9.5 mm diameter orifice leading to a pressure of $\sim 5 \times 10^{-4}$ Torr in this region. The molecular beam is subsequently collimated by two ~ 1 mm wide slits entering the second differentially pumped region. The typical pressure in this region is maintained below 10^{-5} Torr during experiments. Considering the dimensions of the gas extraction orifice (9.5 mm) and the slit widths (~ 1 mm), this means that the molecular beam in the high vacuum chamber is best classified as collisionless “near-effusive”.²⁹ Therefore, the measured speeds of SiH and CH in the molecular beams approximate the random speeds of SiH and CH in the plasmas and that this can be used to study the kinetic translational temperatures of SiH and CH in the plasmas.

For speed measurements, the laser is directed into the high vacuum chamber such that it intersects the molecular beam at a 90° angle, Figure 2.5. To improve spatial and temporal resolution, the ICCD pixels are not binned and a short gate width of 100 ns is used for speed measurements. For high accuracy of the measurements,

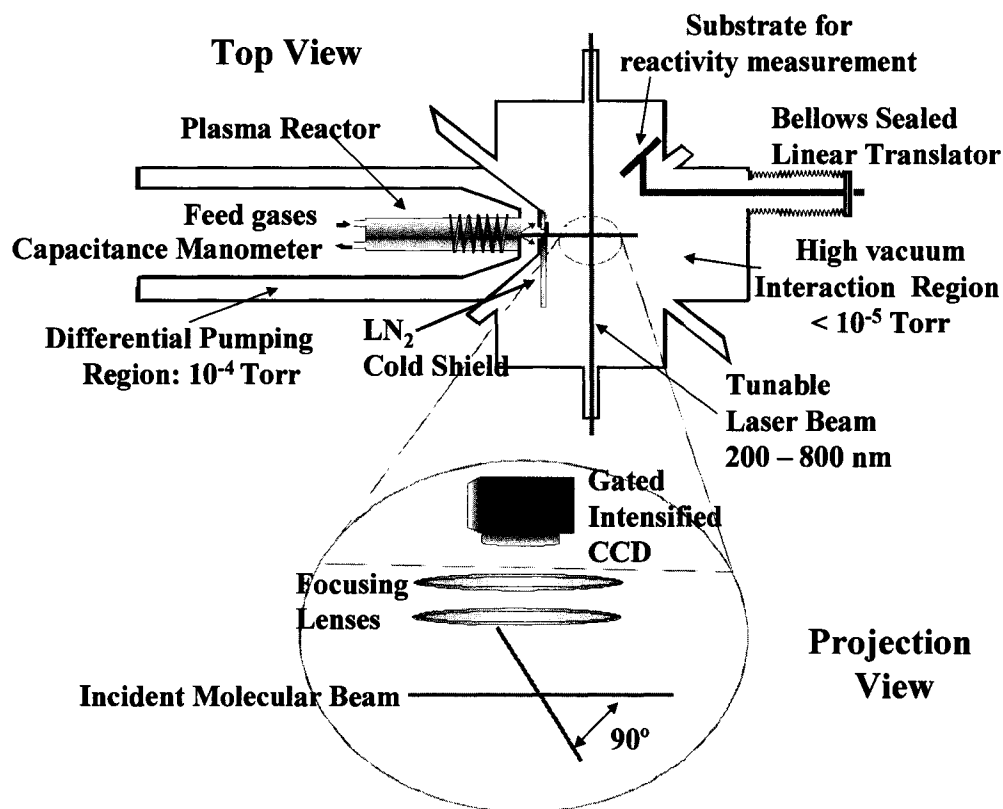


Figure 2.5. Schematic of the modified IRIS apparatus used for speed measurements. The ICCD camera is located perpendicular to the plane of intersection and directly above the interaction region. The laser beam intersects the molecular beam at a 90° angle.

time delays are preferentially taken as high as possible. However, this is limited by the radiative lifetimes of SiH and CH. For SiH experiments, the ICCD images were taken at four different delays, typically 205, 505, 805, and 1105 ns after the laser pulse and the LIF signals were collected for 8 or 12 accumulations of 10^4 laser shots at each time delay. In Chapter 6, these ICCD images were taken at 205, 705, 1205, and 1705 ns after the laser pulse for CH excitation with 5 to 8 accumulations of 6,000 laser shots at each time delay. Background images obtained with an off-resonance laser wavelength were subtracted from the on-resonance images. One-dimensional cross section plots were made by averaging over 100 rows (10.08 mm) of pixels perpendicular to the laser beam and plotting signal intensity as a function of distance away from the laser beam path. This leads to “snapshots” of the spatial position of the LIF intensity at four different time delays. Because only relatively short time delays could be used in both SiH and CH systems, the spatial movement at different time delays is not obvious. Therefore, to accurately determine the peak positions of LIF intensity, a symmetrical laser spatial profile is assumed and the plot is fitted by a Gaussian function. As described previously,¹⁹ the peak positions are then plotted as a function of time delay and fit with a linear regression. The slope of this linear fit yields the average speeds of SiH and CH along the center axis of the molecular beam.

The translational temperatures can be calculated from the average speeds as noted above ($\Theta_T = \pi m v^2 / 8k$, where m is the mass of the radical and k is Boltzmann constant).^{29,30} Note that the average speed obtained by this method is considered as a lower limit because radicals are also moving in radial directions. To account for this, a Monte Carlo simulation program is used to simulate the spatial LIF intensity of SiH and CH along the molecular beam's central axis. This model assumes a Gaussian laser beam profile and calculates its time evolution using a Maxwell-Boltzmann

distribution of molecular speeds within the molecular beam. As the molecular beam is well-collimated in the direction of propagation, the molecular speed distribution is described by a Maxwell-Boltzmann distribution of speeds:³¹

$$\frac{N_v}{N} = 4\pi \left(\frac{m}{2\pi kT} \right)^{3/2} v^2 e^{-mv^2/2kT} \quad (12)$$

where N_v is the number density at the speed (v); m is the mass of molecule; k is the Boltzmann constant; and T is the translational temperature, Θ_T . Curves are calculated for different Θ_T using a statistically significant number of pseudorandom numbers and are normalized to the same peak height. Other than the peak height, there are no adjustable parameters in the model. The Θ_T that best describes the data is determined by nonlinear least square regression analysis.³⁰ The peak positions of the simulated data are plotted again as a function of time delay and the slope is compared with the experimentally obtained value. The procedure is repeated at different temperatures until a best fit is obtained, yielding the final translational temperatures of SiH and CH in the plasma.

References

- (1) Mackie, N. M.; Castner, D. G.; Fisher, E. R. *Langmuir* **1998**, *14*, 1227.
- (2) Lee, K. P.; Park, S. Y.; Kim, N.; Song, S. K. *Mol. Cryst. Liq. Cryst.* **1993**, *224*, 53.
- (3) Apel, P. Y.; Blonskaya, I. V.; Orelovitch, O. L.; Root, D.; Vutsadakis, V.; Dmitriev, S. N. *Nucl. Instr. and Meth. in Phys. Res. B* **2003**, *209*, 329.
- (4) Martin, C. R. *Science* **1994**, *266*, 1961.
- (5) Fleischer, R. L.; Price, P. B.; Walker, R. M. *Nuclear Tracks in Solids*; Univ. of California Press: Berkeley, CA, **1975**.
- (6) Steen, M. L.; Flory, W. C.; Capps, N. E.; Fisher, E. R. *Chem. Mater.* **2001**, *13*, 2749.
- (7) Cepak, V. M.; Martin, C. R. *Chem. Mater.* **1999**, *11*, 1363.
- (8) Cepak, V. M.; Hulteen, J. C.; Che, G.; Jirage, K. B.; Lakshmi, B. B.; Fisher, E. R.; Martin, C. R. *J. Mater. Res.* **1998**, *13*, 3070.
- (9) Hulteen, J. C.; Martin, C. R. *J. Mater. Chem.* **1997**, *7*, 1075.
- (10) Menon, V. P.; Martin, C. R. *Anal. Chem.* **1995**, *67*, 1920.
- (11) Thompson, B. E.; Allen, K. D.; Richards, A. D.; Sawin, H. H. *J. Appl. Phys.* **1986**, *59*, 1890.
- (12) Grill, A.; Meyerson, B. S. *In Synthetic Diamond: Emerging CVD Science and Technology*; John Wiley & Sons: New York, **1994**.
- (13) Sandrin, L.; Silverstein, M. S.; Sacher, E. *Polymer* **2001**, *42*, 3761.
- (14) Williams, K. L.; Martin, I. T.; Fisher, E. R. *J. Am. Soc. Mass. Spectrom.* **2002**, *13*, 518.
- (15) Minayeva, O. B.; Hopwood, J. J. *J. Appl. Phys.* **2003**, *94*, 2821.

- (16) Backer, H.; Bradley, J. W.; Kelly, P. J.; Arnell, R. D. *J. Phys. D: Appl. Phys.* **2001**, *34*, 2709.
- (17) *SmartProbe: Installation and Software Manual*; Scientific Systems, Ltd, **2004**.
- (18) Fisher, E. R. *Plasma Process. Polym.* **2004**, *1*, 13.
- (19) Zhang, J.; Williams, K. L.; Fisher, E. R. *J. Phys. Chem. A* **2003**, *107*, 593.
- (20) Williams, K. L.; Fisher, E. R. *J. Vac. Sci. Technol. A* **2003**, *21*, 1024.
- (21) McCurdy, P. R.; Butoi, C. I.; Williams, K. L.; Fisher, E. R. *J. Phys. Chem. B* **1999**, *103*, 6919.
- (22) Becker, K. H.; Brenig, H. H.; Tatarczyk, T. *Chem. Phys. Lett.* **1980**, *71*, 242.
- (23) Bauer, W.; Becker, K. H.; Duren, R.; Hubrich, C.; Meuser, R. *Chem. Phys. Lett.* **1984**, *108*, 560.
- (24) Luque, J.; Crosley, D. R. LIFBASE: Database and spectral simulation; 2.0.54 ed. ed.; SRI International Report No. MP 99-009, **2005**.
- (25) Luque, J.; Juchmann, W.; Jeffries, J. B. *Appl. Opt.* **1997**, *36*, 3261.
- (26) Steinfeld, J. I. *An Introduction to Modern Molecular Spectroscopy*; The MIT Press: London, England, **1985**.
- (27) Hollas, J. M. *Modern Spectroscopy*; John Wiley & Sons, Inc.: New York, **1998**.
- (28) Scoles, G.; Bassi, D.; Buck, U.; Laine, D. *Atomic and Molecular Beam Methods*; Oxford University Press: New York, Oxford, **1988**; Vol. 1.
- (29) Kessels, W. M. M.; McCurdy, P. R.; Williams, K. L.; Barker, G. R.; Venturo, V. A.; Fisher, E. R. *J. Phys. Chem. B* **2002**, *106*, 2680.
- (30) McCurdy, P. R.; Venturo, V. A.; Fisher, E. R. *Chem. Phys. Lett.* **1997**, *274*, 120.

- (31) Serway, R. A. *Physics for Scientist and Engineers*; Saunders College
Publishing: New York, 1986.

CHAPTER 3

SYNTHESIS AND PROPERTIES OF PLASMA-POLYMERIZED POLYPYRROLE/Au COMPOSITE NANOFIBERS

Reprinted with permission from Jie Zhou and Ellen R. Fisher, *J. Nanosci. Nanotech.* **4**, 539-547, 2004

This dissertation chapter contains results from a paper published in the *Journal of Nanoscience and Nanotechnology*. The manuscript was written by Jie Zhou and edited by Ellen R. Fisher. This chapter describes the chemical, structural, and electrochemical characteristics of a nanostructured composite material formed from plasma-polymerized polypyrrole-coated Au fibers. Additionally, the effect of thermal treatment on the electrochemical properties of the polypyrrole films was studied.

3.1. Introduction

Polypyrrole (PPy) is an intrinsically conducting polymer that has attracted the attention of researchers for many years,¹⁻⁴ primarily because of the numerous applications potentially available through its electrical properties. For example, PPy films have recently been evaluated as gate materials for polymer-based FETs (field-effect transistors).⁵ Traditional materials used in electrical applications (metals and silicon-based semiconductors) may be replaced by PPy films in the future because of advantages in physical properties, cost, and ease of production with PPy materials. Since the first demonstration of a polythiophene FET by Tsumura in 1986,⁶ PPy-based FETs have been actively investigated for their potential applications as matrix-array drivers of large area LCD panels.⁵ PPy films can also be used in electro-optic devices and as coatings for gallium arsenide (GaAs) and silicon semiconductor electrodes.⁷ The conduction mechanisms of PPy films have been studied extensively. The neutral forms of the polymers are generally not conductive but rather large band gap insulators. By oxidizing or reducing the polymer, either chemically or electrochemically, conductivity is obtained. This process is sometimes called “doping” but is different than the usual doping of semiconductors. The conduction comes about from the production of polaron (low doping) and bipolaron (high doping) states in the gap of the polymer. Chemically these states are equivalent to a radical and a diradical. Conductivity is via propagation of the polarons through the polymer which may be thought of chemically as shifting of the double bonds.

Many methods are used in the synthesis of polymer films, such as traditional chemical polymerization,² electrochemical polymerization,^{3,8} and chemical vapor deposition (CVD).^{4,9} Recently, plasma polymerization or plasma-enhanced CVD (PECVD) has also been used to prepare semiconducting polymer films.^{7,10-12} Plasma

polymerization utilizes an ionized gas produced by a gaseous electric discharge. In non-equilibrium plasmas, the gas temperature may be near ambient (<1000 K), whereas the electron temperature is high enough ($\sim 10^5$ K) that the electrons can rupture molecular bonds.^{13,14} When an organic vapor is used to form a plasma, the deposition of polymeric films onto an exposed surface is often observed.¹⁵ Radicals resulting from the collision of the organic monomer molecules and high energy electrons can combine on surfaces to form the polymeric materials.¹⁴ In some instances, polymerization takes place in the gas phase of the plasma. Advantages of this technique include good adhesion of the film to the substrate, solvent-less processing requirements, production of “pinhole-free” films, and the ability to form copolymers from monomers with very different chemistries.^{10,13,14,16} Conversely, branching and crosslinking of the polymer film can adversely affect the structure and conductivity of the polymer.¹⁷ Pulsed-plasmas have also been used to synthesize polymer films. With pulsed-plasmas, high retention of the monomer functional group can be achieved because of the milder pulsed conditions that limit the film’s exposure to high energy plasma species.¹

There is a considerable interest in nanoscale materials with novel or enhanced physical and chemical properties.^{18,19} In general, many of these studies are driven by the desire to improve mechanical, magnetic, or electrical properties of the materials.^{3,20} These materials have wide-ranging implications to a variety of areas including chemistry, physics, electronics, optics, and biomedical science.² Recently, template-directed synthesis is one of the major strategies used to construct new nanomaterials.²¹⁻²⁴ This method typically entails synthesizing the desired material through electropolymerization,^{3,22} CVD,^{20,24,25} and solution-phase electroless deposition^{23,26} within the pores of membranes. Compared with conventionally

prepared PPy, conductive microtubules exhibit different properties, specifically a higher degree of molecular and supermolecular order resulting in better electrical conductivity.^{19,27} Also, the diffusion-limiting kinetics of polymer electrodes are strongly influenced by the nature of the surface between the electrode and electrolyte interface.^{3,28} Hence, the exploration of the properties of conducting polymers coated on open or closed nanotubular materials has attracted many scientists.^{3,4} These unique nanostructures have potential applications in many areas including electronics, functional devices, and nano-biomolecular applications.^{2,3,20} Here, we explore the combination of plasma polymerization to produce PPy films (PPPy) coated on Au tubules, creating a composite nanostructured material.

3.2. Results and Discussion

3.2.1. Spectroscopic analysis of PPPy films. It is well known that the extent of plasma polymerization of a monomer largely depends on the pressure in chamber, applied rf power, rate of monomer flow, addition of carrier gases and the position of the substrate in the reactor. The rate of polymerization via a free radical mechanism depends on the square root of initiator concentration and varies directly with monomer concentration.¹³ Figure 3.1 shows FTIR spectra of films deposited in pulsed plasmas ($P_p = 130$ W) as a function of the duty cycle of the plasma. These spectra clearly show that decreasing the duty cycle of the plasma leads to increased retention of the pyrrole ring. This is demonstrated by the increase in the =C-H in-plane deformation ($1037\sim 1096$ cm^{-1})⁵ and the =C-H out-of-plane deformation (740 cm^{-1})⁵ as the duty cycle decreases. Both of these vibrations indicate an increase in the aromatic ring breathing of pyrrole. Furthermore, the decrease in the C \equiv N stretch (2219 cm^{-1}) and the aliphatic C-H stretching at (2900 cm^{-1}), which come from the

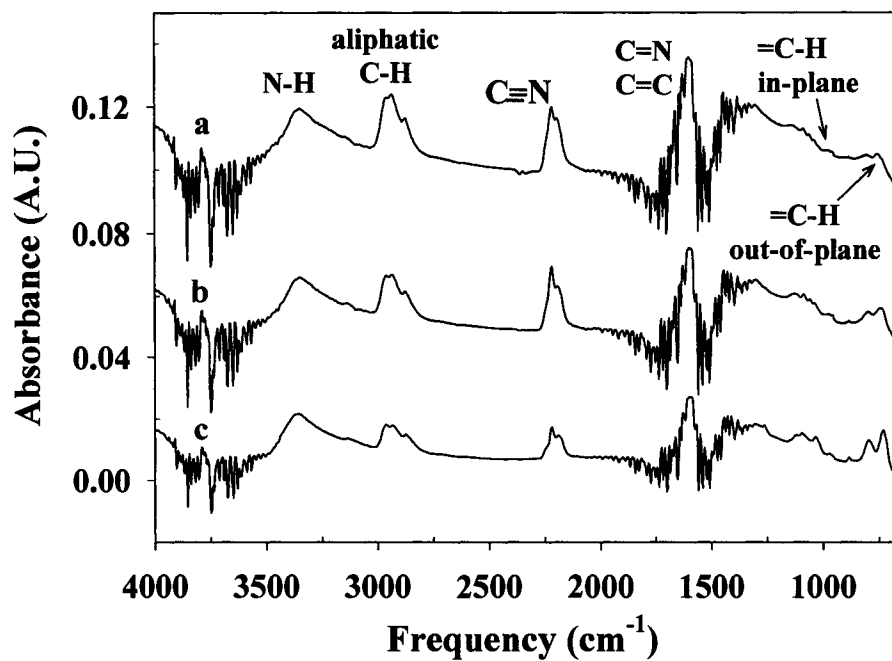


Figure 3.1. FTIR spectra of PPPy films deposited using pulsed plasmas with $P_p = 130$ W and duty cycles of (a) 30%, (b) 20%, and (c) 10%. Spectra have not been normalized, but spectra a and b are offset from their baseline.

partial ring –opening reactions of the pyrrole monomer, is consistent with the hypothesis that increasing the applied plasma power (equivalent CW power) results in more ring-opening reactions.²⁹ When the pyrrole rings are broken, branching and crosslinking reactions tend to occur predominantly.³⁰ Thus, increasing the duty cycle of the plasma leads to increased branching and crosslinking.

The PPPy films deposited on ITO glass substrates in our lab were quite uniform, thin and pinhole-free. However, they were also soft, easily scratched, and peeled from the surface in the LiClO₄/acetonitrile electrolyte solution, making it difficult to perform cyclic voltammetry on these materials.⁵ It has been reported that thermal treatment of PPPy films can increase the stability and electrical properties.⁵ For this reason, thermal treatment of the PPPy films was performed at 300 °C, under N₂ atmosphere for 1 hour. Thermally treated PPPy films were darker in color and stable enough to endure repeated CV scans in the LiClO₄/acetonitrile solution. The FTIR spectrum of the thermally treated PPPy film is shown in Figure 3.2a. Compared to the as-deposited PPPy film (Figure 3.2b), the thermally treated material has an extremely wide absorption band at ~1600 cm⁻¹ indicating the conjugated structure is significantly increased in these materials. In contrast, the C≡N stretching at 2219 cm⁻¹ and the aliphatic C-H stretching at 2900 cm⁻¹ is decreased in the spectrum of the thermally-treated materials. This suggests that the thermal treatment results in retention of unsaturated chains of PPy and removes low molecular weight fragments in the PPPy film caused by the plasma polymerization process.

The UV-Vis spectra of as-deposited and thermally-treated PPPy films are shown in Figure 3.3. Both films exhibit broad absorption bands above 400 nm, with some underlying structure, indicative of a conjugated system with heteroatoms.¹⁶ The as-deposited film has several broad absorption bands nominally centered at ~290 nm,

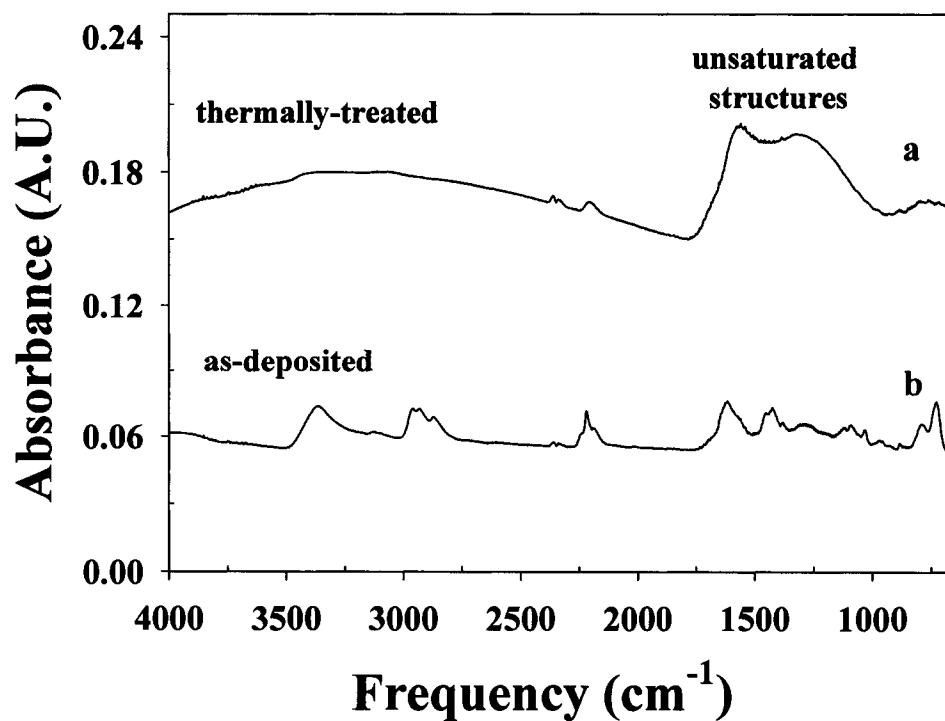


Figure 3.2. FTIR spectra of PPPy films, (a) after thermal treatment, (b) before thermal treatment. The thermal treatment lasted for one hour at 300 °C under a nitrogen atmosphere. Spectra have not been normalized, but spectra a and b are offset from their baseline.

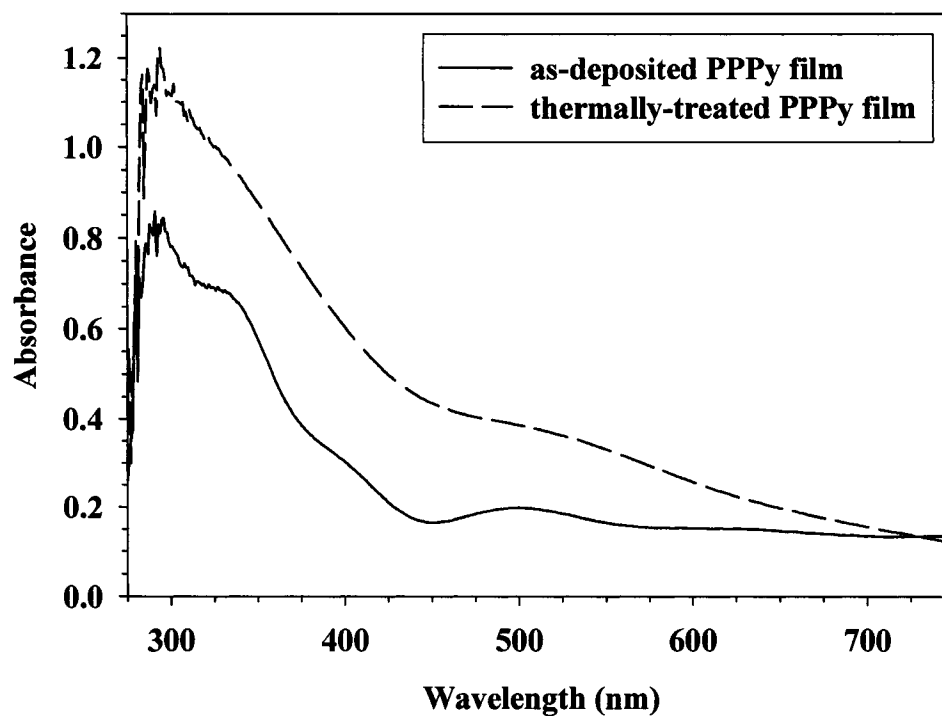


Figure 3.3. UV-Vis spectra of PPPy films as-deposited and thermally-treated PPPy. Thermal treatment was for 1 hour at 300 °C under N₂ atmosphere.

340 nm, 400 nm, and 500 nm. There is, however, only a small absorption at wavelengths above ~500 nm. Both experimental and theoretical studies of the HOMO-LUMO gaps for pyrrole oligomers have shown that the absorption band centered at 400-435 nm correlates to long chain polypyrrole.³¹⁻³⁴ The absorption bands at lower wavelengths correspond to the coexistence of both neutral and charged oligomers. Also, the band centered at 500 nm has been associated with the existence of a bipolaron band,³³ as well as with a shorter chain polypyrrole.^{32,34} In contrast to the as-deposited film, the annealed film exhibits a strong absorption band at the higher wavelengths. This suggests the thermally treated material has more wide-range conjugation, in agreement with the FTIR data.

Survey XPS spectra showed that both the thermally treated and the as-deposited films contained low concentrations of oxygen (<6%), primarily as a result of oxidation reactions post deposition.³⁵ XPS high resolution C_{1s} and N_{1s} spectra for as-deposited and thermally treated PPPy films are shown in Figure 3.4. All the binding energies were referenced to the peak of α carbons in the ring of pyrrole at 285 eV. The C_{1s} spectrum for the as-deposited film is rather broad and asymmetric on the high binding energy side, Figure 3.4a. Line shape analysis reveals that the C_{1s} peak can be decomposed into three lines. The lowest energy component is at 283.7 eV (FWHM=1.84 eV, 20.0%) and can be attributed to β carbons in the pyrrole ring.³⁶ The line characteristic of the α carbons in the ring is located at 285.0 eV (FWHM=1.96 eV; 50.5%).³⁶ The third line located at 286.3 eV (FWHM=2.34 eV; 29.5%) is relatively broad and is likely an overlap of C=N, carbonyl groups or carbon bonded to oxygen.³⁷ The N_{1s} spectrum for the as-deposited film also contains three components, Figure 3.4b. The line centered at the lowest binding energy, 398.4 eV

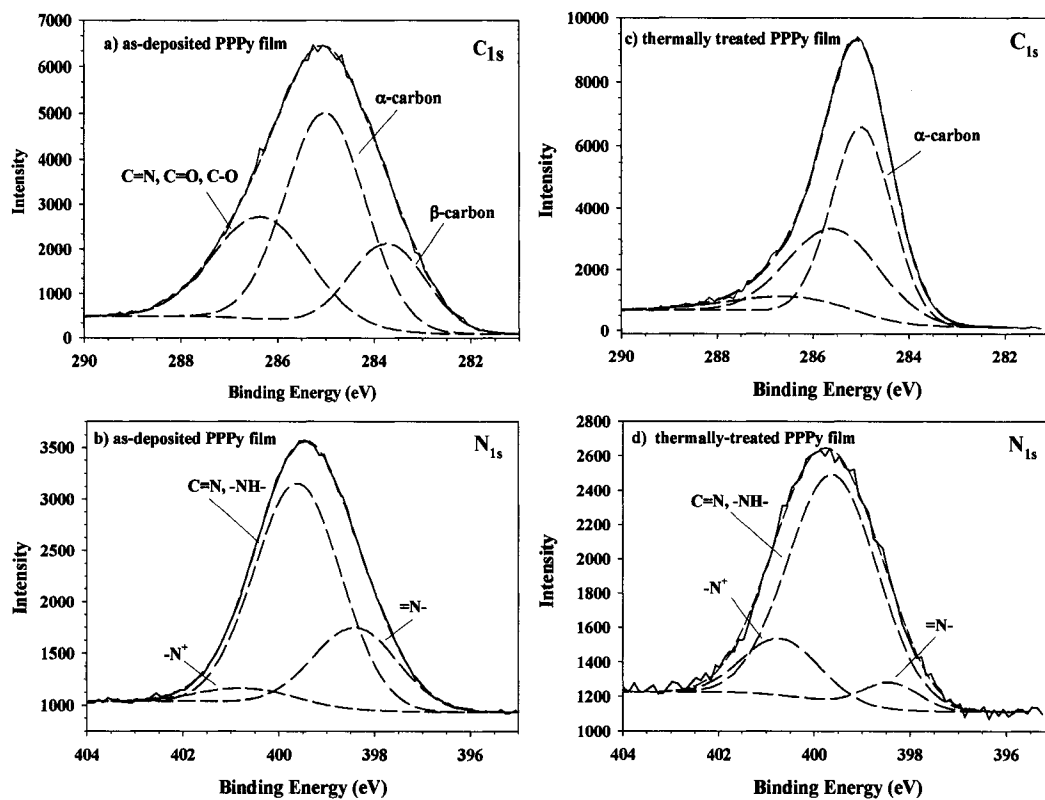


Figure 3.4. High resolution XPS C_{1s} and N_{1s} of as-deposited and thermally-treated PPPy films. Dashed lines represent the curve fits to the data using Gaussian line shapes. Thermal treatment was for 1 hour at 300 °C under N₂ atmosphere.

(FWHM=2.06 eV; 25.1%), results from =N-; whereas the largest component in the spectrum at 399.6 eV (FWHM=2.11eV; 70.0%) is assigned to -NH- and C≡N.³⁷ The third line at 400.7 eV (FWHM=2.32 eV; 4.9%) is from nitrogen atoms that are more positively charged than the nitrogen atoms of the main pyrrole peak.^{37,38} In general, the presence of three peaks in the N_{1s} spectrum is indicative of the neutral form of polypyrrole.³⁹ For the 401 eV binding region of the N_{1s} core level, it has been shown that shifts of ~5.8 eV per unit charge occur.³⁸ Using this value, extra charges of the order of +0.2 are present on selected N atoms in our films. It is, however, generally accepted that this charge does not occur at specific nitrogen sites, but rather involves the entire pyrrole ring unit.^{36,40} Note that these spectra and assignments are similar to those found in the literature for PPPy films^{16,37,41} and for some electrochemically grown films.^{36,39} Upon thermal treatment, both C_{1s} and N_{1s} spectra undergo significant changes. Specifically, in the C_{1s} spectrum, Figure 3.4c, the peak has narrowed considerably, reducing the high energy binding component to a shoulder. The three peaks at 285.0 eV (FWHM = 1.5 eV; 54.1%), 285.54 eV (FWHM = 2.3 eV; 34.7%), and 286.54 eV (FWHM=2.9 eV; 8.2%) are assigned to the α carbons in the ring, and to C-O or C-N peaks. The N_{1s} peak structure, Figure 3.4d, has also changed, with a significant decrease in the =N- peak at 398.4 eV (FWHM=1.39 eV; 5.8%), and a strong increase in the amount of highly positive nitrogen atoms [400.7 eV (FWHM=1.87 eV; 16.4%)]. The primary component at 399.6 eV remains dominant, however, accounting for nearly 80% of the nitrogen atoms (FWHM=2.18eV; 77.8%).

It is useful to explore the peak shapes in the XPS spectra. Note that for the both the as-deposited and the thermally-treated PPPy films, the peak shapes are somewhat asymmetrical. The skewed shape of the C_{1s} XPS peaks in polypyrrole materials has been attributed to cross-linked, chain terminating or non-α,α' bonded

carbons as well as carbons in partially saturated rings.³⁶ This type of carbon is considered as a measure of the disorder of the material. In the N_{1s} spectra, as noted above the asymmetric shape is considered to be a result of electrostatic effects. A comparison of the spectra for as-deposited PPPy films and thermally treated PPPy films suggest that again, there is somewhat more order in the thermally-treated materials than the as-deposited materials. Moreover, the highest binding energy peak in the C_{1s} spectra for the thermally-treated material could be assigned to $\pi-\pi^*$ shakeup satellite structures,³⁶ again indicative of an unsaturated polymeric system with intact aromatic structure. Thus, the FTIR, UV-Vis, and XPS analyses of these films indicate that thermal treatment of the PPPy films results in a more ordered material, most likely through the loss of loosely-bound short chain oligomers.

3.2.2. Gas-phase analysis of pyrrole plasmas. Detecting gas-phase species (ions, radicals) in-situ during plasma polymerization of pyrrole is critical to understanding the mechanism for polymerization of pyrrole. Therefore, mass spectral analyses of the pyrrole plasma were performed. Figure 3.5a shows the mass spectrum of pyrrole vapor (plasma off), which represents simply the fragmentation pattern of the monomer. The main component is located at 66 m/z, the M-1 peak of pyrrole, $C_4H_4N^+$, where M represents the parent monomer mass (i.e. m/z = 67). The mass peaks at m/z = 39~41 are easily assigned to $C_3H_3^+$, $C_3H_4^+$ and $C_2H_2NH^+$,⁴² respectively; and the peak at m/z = 28 can be attributed to $HC\equiv NH^+$.⁴² Figure 3.5b shows the mass spectrum of a CW plasma of pyrrole at an applied rf power of 13 W, which is the equivalent power for a 10% pulsed plasma with $P_p = 130$ W. No new peaks were observed in the mass spectrum when the plasma was on. Also, a large range scan from 1-200 m/z was also performed contained no obvious mass peaks

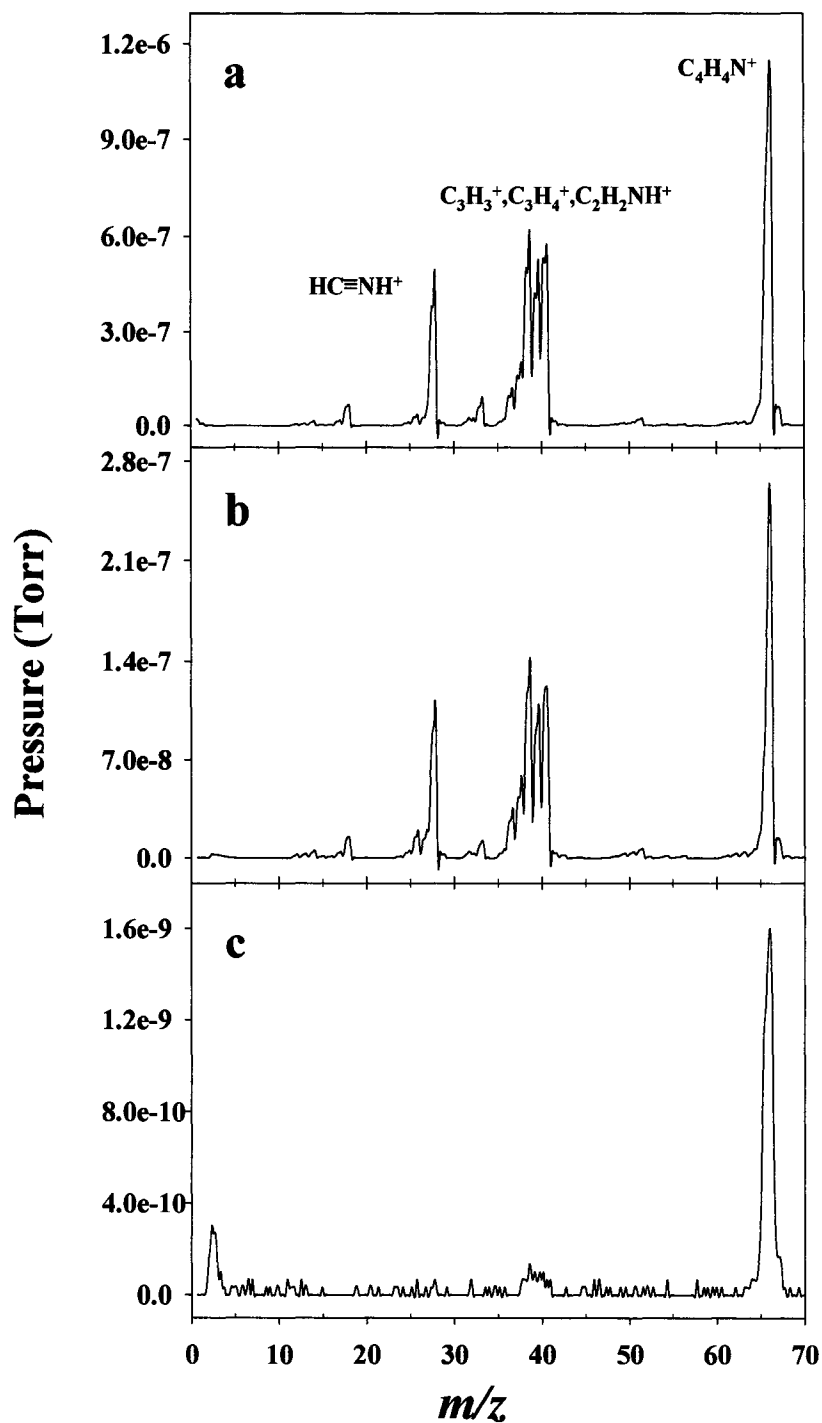


Figure 3.5. Mass spectra of gas-phase plasma species. (a) The fragmentation pattern of pyrrole monomer with plasma off and ionizer on; (b) The mass spectrum of gas-phase species in a pyrrole plasma (13 W CW) with the ionizer on (electron energy of 70 eV). (c) The mass spectrum of nascent ions generated by 13W CW pyrrole plasma.

above $m/z = 66$, suggesting that no polymerized species are present in the gas-phase of the plasma. Because this low power plasma may not be completely consistent with the 130 W pulsed plasma, we did perform mass spectral analysis at a somewhat higher applied rf power of 25 W. There was essentially no difference in the mass spectra at the higher power. This is consistent with the hypothesis that plasma polymerization in this system takes place primarily on the surface of the substrate as a result of the diffusion of plasma species to the surface, rather than in the gas-phase.

The mass spectrum of nascent ions produced in the pyrrole plasma (13 W CW plasma on, filament off) is shown in Figure 3.5c. The most prominent peak in this spectrum is the M-1 peak of pyrrole, with smaller peaks from the fragments of pyrrole at 39 m/z -41 m/z . From Figure 3.5, it is clear that the plasma we used did not generate a significantly different fragmentation pattern for the monomer. Indeed, the cleavage patterns of pyrrole in our plasma demonstrate the similar ring cleavage patterns as are observed in the mass spectrum of pyrrole.⁴²

3.2.3. Morphology. The morphology of the flat ITO glass substrates is shown in Figure 3.6a, demonstrating these substrates do have some roughness on the submicron scale. The morphology of PPPy films (as-deposited) on the flat ITO glass is shown in Figure 3.6b. Spherical structures can be seen on the surface, with spherulite sizes ranging from 1.2~2.5 μm , clearly much larger than the roughness of the underlying ITO. This type of globular structure has been observed previously for PPy films produced via electrochemical means,²⁸ and by plasma polymerization.⁴³ In general, these structures can be explained by diffusion controlled nucleation growth at the surface of the film.¹³ Under these conditions, tiny dust particles on the surface of the substrate possibly can serve as nucleation sites during plasma polymerization. This type of growth mechanism is consistent with the mass spectral data that showed there

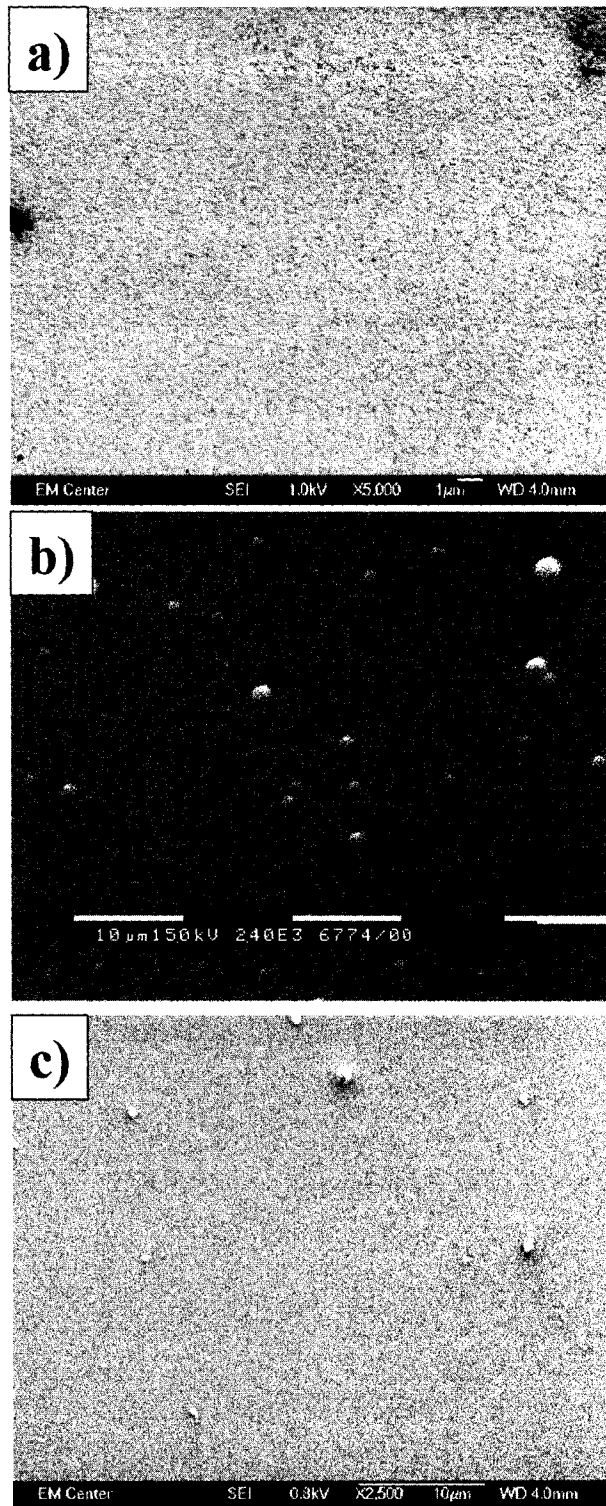


Figure 3.6. SEM images of a) flat ITO substrate; b) PPPy film deposited on flat ITO conductive glass by a pulsed plasma with $P_p = 130$ W, a 10% duty cycle, and deposition time of 5 min; and c) thermally-treated (1 hour at 300 °C under N₂) PPPy film on flat ITO substrate.

are no high mass polymer species in the gas phase. In addition, the structure of the polymer may not be true polypyrrole, but may contain other cross-linked products, as expected from the observed changes in the FTIR spectra upon thermal treatment (Figure 3.2) and from the UV-Vis spectra. The presence of trapped oligomers in the polymer could also contribute to the observed morphology. Upon thermal treatment, however, these spherulites do not completely disappear from the surface of the films, Figure 3.6c.

Figure 3.7 shows a series of SEM images of nanostructured materials. The electron micrograph in Figure 3.7a is of 1000 nm Au nanotubes that have been removed from the bulk of the polyester membrane in which they were formed. The inner diameters of the tubes are 500~600 nm, and the outer diameters are ~1000-1200 nm, consistent with the pore size of the template membrane. This image reveals that the outer surface of these nanotubes is not smooth, but rather contains a high level of porosity. This structure could be the result of a limited number of complexation sites on the pore walls during the growth of Au nanotubes.¹ Alternatively, formation of grain boundaries, defects or vacancies in the metal could also explain the incomplete nature of the growing material.

Figure 3.7b shows the SEM image of Au nanotubes coated with PPPy films, demonstrating the PPPy film covers the entire surface of each of the Au nanotubes, with no exposure of the underlying gold. With increasing deposition time, the Au nanotubes can be converted into nanofibers coated with PPPy films, including complete caps on the ends of the tubes.¹ Figure 3.7c shows a higher magnification SEM image of PPPy film coated Au nanotubes after thermal treatment (300 °C for 1 hr). The PPPy films are somewhat smoother after thermal treatment, and the ends of the tubes appear to be completely capped in this image. This suggests that thermal

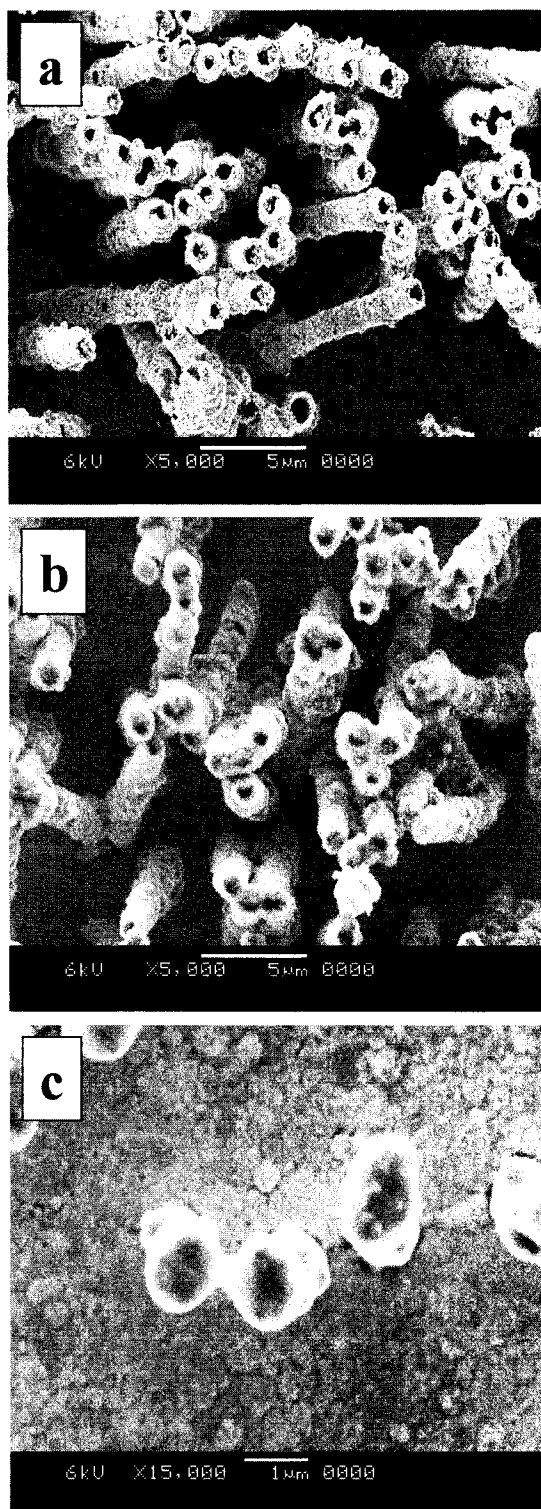


Figure 3.7. SEM images of: (a) bare 1000 nm Au nanotubes; (b) 1000 nm Au nanotubes coated with PPy film deposited using a pulsed plasma with $P_p = 130\text{W}$, a 10% duty cycle, and a deposition time of 5 min; (c) the Au/PPy composite nanotubes after thermal treatment (1 hour at 300 °C under N_2).

treatment eliminates fragments, increases the content of unsaturated structures, and results in denser, smoother PPPy films. It is also possible that the thermal treatment results in smoother films simply because of increased mobility of the polymer chains, leading to a configuration with lower surface energy.⁴⁴ CV data of the composite membrane after the thermal treatment could not, however, be obtained because thermal treatment damaged the membrane ensemble.

3.2.4. Cyclic voltammetry (CV). Electrochemical properties of PPPy films were characterized by a series of CV analyses in LiClO₄/acetonitrile non-aqueous solutions. PPPy films deposited on flat ITO electrodes did not demonstrate redox peaks within the potential scans (Figure 3.8a, dash line). It has been reported that thermal treatment can improve the stability and electrochemical properties of PPPy films.⁵ Figure 3.8b shows the cyclic voltammogram of the thermally treated PPPy film coated on the flat ITO electrode. The scan rate is 100 mV/S and the potential scan region is from -1250 mV to 1250 mV. The redox properties of the PPPy films can be seen at -700 mV and 415 mV. A large non-Nernstian electrochemical behavior (peak separation, $\Delta E_p > 59/n$ mV) was observed due to slow electron transfer kinetics.

Nanomaterials have attracted researchers because of their unique structural properties, such as large surface areas, which is especially important for electrochemical processes.^{9,25} Figure 3.8c shows the CV data of non-thermally treated PPPy films coated on 1000 nm Au nanotubes. Compared with the electrochemical properties of the as-deposited PPPy film coated on the flat ITO electrode, the irreversible redox peaks can be seen at ~960 mV and ~400 mV. The diffusion coefficient of the ions within the polymer is strongly influenced by the thickness, surface morphology and the bulk structure of the polymer.^{3,28} Here we

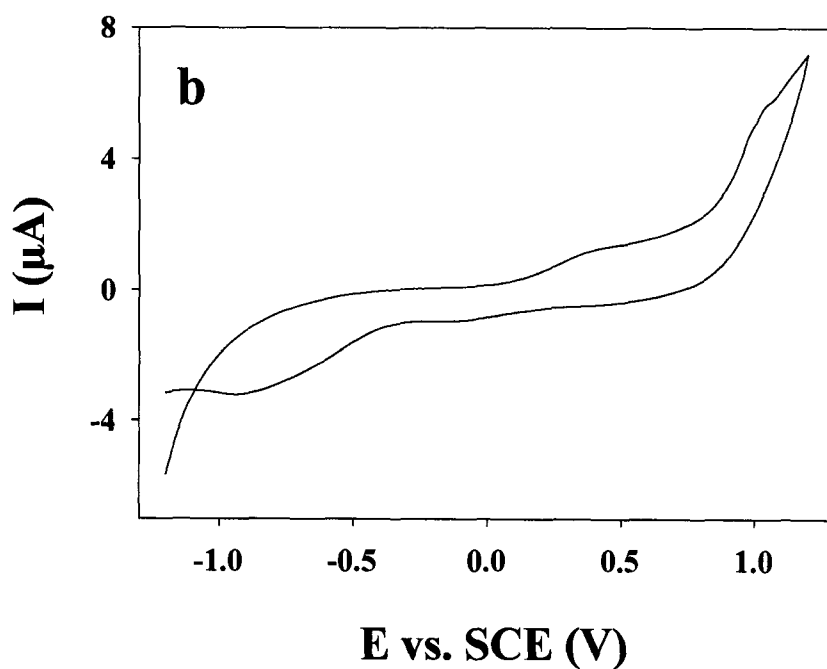
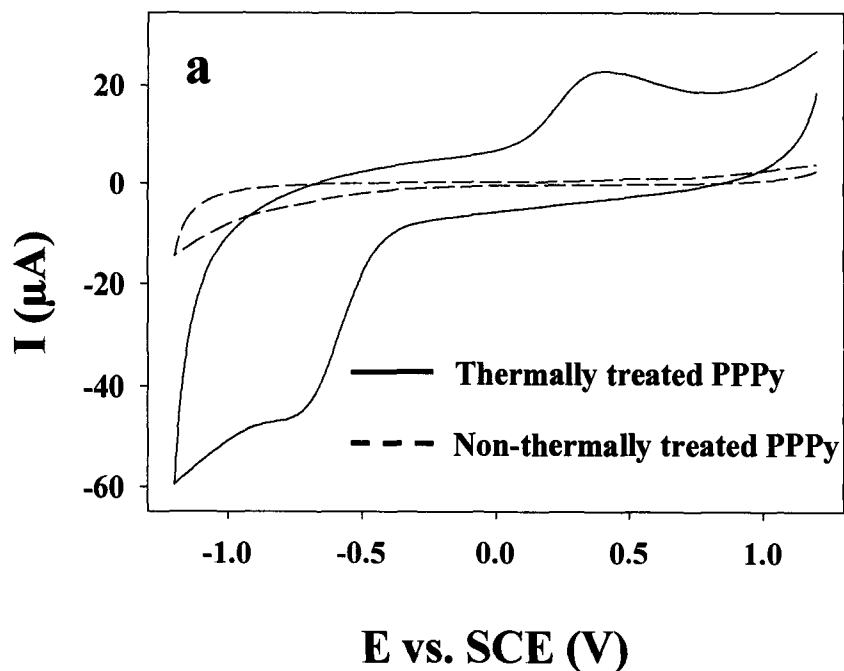


Figure 3.8. (a) Cyclic voltammograms of as-deposited (dashed line) and thermally-treated (solid line) PPPy films coated on flat ITO electrodes. Electrolyte solution was 0.1 M LiClO₄ in acetonitrile. (b) Cyclic voltammogram of as-deposited PPPy film deposited on 1000 nm Au nanotubes by a pulsed plasma with $P_p = 130\text{W}$, a 10% duty cycle, and deposition time of 5 min.

believe film thickness also plays a key role in determining the electrical properties of the material. The Au nanotubes provide a large surface area support for the thinner PPPy films, resulting in an increased electron transfer within the PPPy electrode. Literature studies also showed that templated-synthesized polypyrrole nanotubes with large-diameter displayed a conductivity comparable to that of bulk polypyrrole, whereas small diameter tubes possessed a conductivity one order of magnitude higher.^{20,45} The narrowest tubes have the highest conductivity because they contain a relatively higher proportion of the ordered material (and a small amount of the disordered material) than the large-diameter tubes.^{20,45} Note that the thermally treated PPPy films coated on the flat ITO electrode demonstrate better electrochemical activities than the as-deposited PPPy films coated on the flat ITO electrode. From the FTIR and SEM data, some changes in the PPPy film morphology and bulk structure clearly occurs upon heating. From Figure 3.2a, the peak absorption around 1600 cm^{-1} increases significantly with an increase in conjugated structures, whereas the peak absorptions at $\sim 2219\text{ cm}^{-1}$ and $\sim 2900\text{ cm}^{-1}$ indicate $\text{C}\equiv\text{N}$ and aliphatic C-H fragments are decreased. SEM images also indicate that the PPPy films are smoother after thermal treatment (Figure 3.7c), as if they have undergone a melting and coagulation progress. It appears that these changes in the morphology and bulk structure after thermal treatment are possibly the result of removal of loosely bound, low-molecular weight oligomers.

3.3. Summary

We have synthesized and characterized the properties of PPPy/Au composite nanotubes. Results from FTIR and XPS studies indicate the chemical and physical properties of PPPy films depend primarily on the applied plasma parameters, most

significantly duty cycle in pulsed plasma polymerization schemes. Ring-opening reactions and the polymerization of pyrrole in the plasma take place simultaneously. Decreasing the duty cycle facilitates the retention of the rings of the pyrrole monomer. Identification of gas-phase species as well as surface analysis data indicate that plasma polymerization of pyrrole occurs on the substrate surface rather than in the gas phase. Thermal treatment of the PPPy films enhances the electrochemical properties as a result of changes in the surface morphology and bulk structures of the films. However, as-deposited PPPy films coated on Au nanotubes demonstrate better electrochemical properties than the as-deposited PPPy films coated on a flat substrate. A non-Nernstian irreversible redox behavior of the composite results from the increase in surface area and decrease in film thickness of PPPy-coated Au nanotubes.

References

- (1) Steen, M. L.; Flory, W. C.; Capps, N. E.; Fisher, E. R. *Chem. Mater.* **2001**, *13*, 2749.
- (2) Duchet, J.; Legras, R.; Demoustier-Champagne, S. *Syn. Met.* **1998**, *98*, 113.
- (3) Chen, J. H.; Huang, Z. P.; Wang, D. Z.; Yang, S. X.; Li, W. Z.; Wen, J. G.; Ren, Z. F. *Synth. Met.* **2002**, *125*, 289.
- (4) Jurewicz, K.; Delpoux, S.; Bertagna, V.; Beguin, F.; Frackowiak, E. *Chem. Phys. Lett.* **2001**, *347*, 36.
- (5) Lee, K. P.; Park, S. Y.; Kim, N. *Mol. Cryst. Liq. Cryst.* **1993**, *224*, 53.
- (6) Tsumura, A.; Koezuka, H.; Ando, T. *Appl. Phys. Lett.* **1986**, *49*, 1210.
- (7) Cherian, L.; Radhakrishnan, P. *Current Science* **1992**, *62*, 423.
- (8) Otero, T. F.; Cheng, S. A.; Huerta, F. *J. Phys. Chem. B* **2000**, *104*, 10522.
- (9) Che, G.; Lakshmi, B. B.; Martin, C. R.; Fisher, E. R. *Chem. Mater.* **1998**, *10*, 260.
- (10) Hirotsu, T.; Hou, Z. *J.M.S.-Pure, Appl. Chem.* **2000**, *A37*, 735.
- (11) Borros, S.; Picazo, L.; Ferrer-Anglada, N.; Takhtoukh, Y.; Esteve, J. *J. Phys.* **1999**, *4*, 9.
- (12) Park, S. Y.; Lee, K. P.; Choi, D. H.; Kim, N.; Song, S. K. *Mol. Cryst. Liq. Cryst.* **1994**, *247*, 321.
- (13) Sathir, R. K.; Schoch, K. F. *J. Thin Solid Films* **1993**, *223*, 154.
- (14) Johnston, E. E.; Ratner, B. D. *J. Electron Spectrosc. and Rel. Phenom.* **1996**, *81*, 303.
- (15) Yasuda, H. *Plasma Polymerization*; Academic Press: Orlando, FL, **1985**.

- (16) Eufinger, S.; Van ooi, W. J.; Ridgway, T. H. *J. Appl. Polym. Sci.* **1996**, *61*, 1503.
- (17) Bhat, N. V.; Wavhal, D. S. *J. Appl. Polym. Sci.* **1998**, *70*, 203.
- (18) Liz-Marzan, L. M.; Norris, D. J. *MRS Bull.* **2001**, *26*, 981.
- (19) Wallace, G. G.; Innis, P. C. *J. Nanosci. Nanotech.* **2002**, *2*, 441.
- (20) Martin, C. R. *Science* **1994**, *266*, 1961.
- (21) Cepak, V. M.; Martin, C. R. *Chem. Mater.* **1999**, *11*, 1363.
- (22) Demoustier-Champagne, S.; Legras, R. *J. Chim. Phys.* **1998**, *95*, 1200.
- (23) Shelimove, K. B.; Moskovits, M. *Chem. Mater.* **2000**, *12*, 250.
- (24) Piraux, L.; Dubois, S.; Duvail, J. L.; Radulescu, A. *J. Mater. Res.* **1999**, *14*, 3042.
- (25) Che, G.; Jirage, K. B.; Fisher, E. R.; Martin, C. R. *J. Electrochem. Soc.* **1997**, *144*, 4296.
- (26) Cepak, V. M.; Hulteen, J. C.; Che, G.; Jirage, K. B.; Lakshmi, B. B.; Fisher, E. R.; Martin, C. R. *J. Mater. Res.* **1998**, *13*, 3070.
- (27) Mikat, J.; Orgzall, I.; Lorenz, B.; Sapp, S.; Martin, C. R.; Burris, J. L.; Hochheimer, H. D. *Physica B* **1999**, *265*, 154.
- (28) Panero, S.; Prospero, P.; Scrosati, B. *Electrochim. Acta* **1987**, *32*, 1465.
- (29) Mackie, N. M.; Castner, D. G.; Fisher, E. R. *Langmuir* **1998**, *14*, 1227.
- (30) Wang, J.; Neoh, K. G.; Kang, E. T. *Thin Solid Films* **2004**, *446*, 205.
- (31) Appel, G.; Schmeisser, D.; Bauer, J.; Bauer, M.; Egelhaaf, H. J.; Oelkrug, D. *Syn. Met.* **1999**, *99*.
- (32) Salzner, U.; Pickup, P. G.; Poirier, R. A.; Lagowski, J. B. *J. Phys. Chem. A* **1998**, *102*, 2572.
- (33) Bredas, J. L.; Street, G. B. *Acc. Chem. Res.* **1985**, *18*, 309.

- (34) Zotti, G.; Martina, S.; Wegner, G.; Schluter, A.-D. *Adv. Mater* **1992**, *4*, 798.
- (35) Gengenback, T. R.; Chatelier, R. C.; Griesser, H. J. *Surf. Interface Analysis* **1996**, *24*, 271.
- (36) Pfluger, P.; Street, G. B. *J. Chem. Phys.* **1984**, *80*, 544.
- (37) Zhang, J.; Wu, M. Z.; Pu, T. S.; Zhang, Z. Y.; Jin, R. P.; Tong, Z. S.; Zhu, D. Z.; Cao, D. X.; Zhu, F. Y.; Cao, J. Q. *Thin Solid Films* **1997**, *307*, 14.
- (38) Pfluger, P.; Krounbi, M.; Street, G. B. *J. Chem. Phys.* **1983**, *78*, 3212.
- (39) Vigmond, S. J.; Kallury, K. M. R.; Thompson, M. *Anal. Chem.* **1992**, *64*, 2763.
- (40) Antanasoska, L.; Naoi, K.; Smyrl, W. H. *Chem. Mater.* **1992**, *4*, 988.
- (41) Tong, Z. S.; Wu, M. Z.; Pu, T. S.; Zhang, Z. Y.; Zhang, J.; Jin, R. P.; Zhu, D. Z.; Zhu, F. Y.; Cao, D. X.; Cao, J. Q. *J. Appl. Polym. Sci.* **1998**, *69*, 1743.
- (42) Silverstein, R. M.; Webster, F. X. *Spectrometric Identification of Organic Compounds*, 6th ed.; John Wiley & Sons: New York, **1998**.
- (43) Cruz, G. J.; Morales, J.; Olayo, R. *Thin Solid Films* **1999**, *342*, 119.
- (44) Murakami, T.; Kuroda, S.; Osawa, Z. *J. Colloid Interface Sci.* **1998**, *200*, 192.
- (45) Kros, A.; Nolte, R. J. M.; Sommerdijk, N. A. J. M. *Adv. Mater.* **2002**, *14*, 1779.

CHAPTER 4

INVESTIGATION OF INDUCTIVELY COUPLED Ar AND CH₄/Ar PLASMAS AND THE EFFECT OF ION ENERGY ON DLC FILM PROPERTIES

This dissertation chapter contains results from a full paper submitted for publication to *Plasma Source Science and Technology*. The manuscript was written by Jie Zhou and edited by Ellen R. Fisher. The coauthors were Ina T. Martin, Reed Ayers, Eli Adams, and Dongping Liu. Reed Ayers performed the hardness measurements for diamond-like carbon (DLC) films. Ina T. Martin, Eli Adams, and Dongping Liu made helpful contributions to the construction of the new system. The aim of this study was to provide insight into the plasma gas-phase physics during the deposition of DLC films. The measurements were performed on a new system that we designed and built to facilitate Langmuir probe and mass spectrometer (MS) measurements on the plasma systems we study using our Imaging of Radicals Interacting with Surfaces (IRIS). The role of ion energy on the structural and mechanical properties of DLC films was investigated by applying different substrate potentials.

4.1. Introduction

Low pressure inductively coupled plasmas (ICPs) have been used to deposit diamond-like carbon (DLC) films. These materials have numerous properties similar to diamond including high hardness, low surface roughness, scratch resistance, chemical inertness, good thermal conductivity, high electrical resistance, and optical transparency.^{1,2} DLC films prepared with plasma enhanced chemical vapor deposition (PECVD) are metastable amorphous materials, which contain a significant amount of hydrogen. When using different deposition methods, the hydrogen content in DLC films was determined to be in the range of < 10% to 60%.³ DLC films are essentially an amorphous network of sp^3 (diamond-like), sp^2 (graphite-like), and even sp coordinated carbon atoms in a disordered network. The properties of DLC films cover a wide range of values between those of diamond, graphite, and hydrocarbon polymers.⁴ However, diamond films are polycrystalline materials, with crystallites up to tens of micron in size, having the crystal structure of diamond. Of different PECVD processes, microwave and electron cyclotron resonance (ECR) are commonly used for deposition of diamond. These methods for growing diamond films are based on the production of high concentrations of atomic hydrogen in the gas phase, which is believed to etch the nondiamond phases during PECVD, thereby, promoting the growth of the diamond.⁵ Although a planar spiral coil coupling an rf field through a quartz window is most commonly used to generate low pressure ICPs,⁶ a helical coil geometry has also been used to provide high density plasma sources for etching and deposition.⁶⁻⁸ Moreover, ion density and ion energy can be independently controlled by rf power input through the helical coil and substrate, respectively.⁹⁻¹¹

Plasma processing parameters significantly influence the properties of DLC films deposited by PECVD. Therefore, the effects of parameters, such as pressure, rf

power (P) and bias voltage on the properties of DLC films have been widely studied.¹²⁻²⁰ Very little, however, has been reported on gas-phase ion and electron kinetics in methane containing plasmas.^{10,21,22} This lack of fundamental gas-phase data has hindered the development of process models that are useful in the improvement of plasma reactor design for DLC film deposition. Hence, full characterization of plasma species is essential to understand gas-phase ion and electron kinetics, and to optimize processing parameters to control the deposition of DLC films.

Langmuir probes and mass spectrometry (MS) are standard gas-phase diagnostic techniques used to investigate plasmas. The former has been utilized to measure important plasma parameters such as plasma potential (V_p), electron density (n_e), ion density (n_i), electron temperature (T_e), and electron energy distribution functions (EEDF), whereas the latter is useful for detecting ions and neutral species generated in plasmas. Additionally, mass spectrometers with energy analysis capabilities can measure ion energy distributions (IEDs) of ions created in the plasma. IEDs are of great importance in plasma assisted processes, therefore they are fundamental parameters for complete characterization of a gas flow discharge. Our group has investigated the effect of ions on the surface reactivity of numerous small molecules during the deposition of carbon and silicon based materials.^{23,24} For example, previously published work involving our Imaging of Radicals Interacting with Surfaces (IRIS) technique shows that in fluorocarbon PECVD systems, ions have a significant influence on both film properties and the surface production of CF_2 .²⁵ Most notably, the scatter coefficients measured for CF_2 are correlated directly to the average ion energies measured for the plasma systems.^{26,27} Clearly gas-phase

diagnostics are critical to understanding PECVD systems and controlling the composition of deposited materials.

The measurements presented in this thesis were made on a new system that we designed and built to facilitate Langmuir probe and MS measurements on the plasma systems we study using IRIS. Details of this apparatus are presented in Chapter 2.2. Here, we used a Langmuir probe and a MS with energy analysis capabilities to characterize low pressure Ar and CH₄/Ar ICPs. The IEDs and relative ion densities of plasma-generated ions were obtained for Ar and CH₄/Ar plasma molecular beams. In general, to measure ion energies, a small sampling orifice (25-100 μm) either on the grounded or the powered electrode is used so that the IEDs are not modified by ion-molecule collisions near the orifice.^{28,29} However, this sampling technique has a drawback in depositing systems such as methane containing plasmas because of the high deposition rate. To measure ion energies in our plasmas we have built a new instrument in which the sampling orifice of the mass spectrometer is used to sample a molecular beam with an ICP source. Materials are deposited and Langmuir probe measurements are made in the plasma source, but the MS measurements are made on a plasma molecular beam created by the source. This work contains the first reported IEDs ions in plasma molecular beams. Some ion-energy exchange via ion-neutral collisions occurs when ions exit the plasma source. This is evaluated based on the measured IEDs. Lastly, the effect of ion energy on the surface and mechanical properties of hydrogenated DLC films were investigated using an independently rf powered substrate. Ion bombardment was found to have a significant influence on the DLC film properties.

4.2. Results and Discussion

4.2.1. Argon. Figure 4.1 shows Langmuir probe data for 100% Ar plasmas as a function of pressure and power. As shown in Figure 4.1(a), both electron and ion density increase with increasing power, similar to Ar ICP data in the literature.^{30,31} In general, the plasma is considered electrically quasi-neutral, i.e. the ion and electron density should be essentially equal ($n_i = n_e$) in the bulk of the plasma. The Langmuir probe data in Figure 4.1(a) show that n_i is about 20-40% higher than n_e in our system. Similar results have been observed in ICP argon plasmas by Kim et al.³⁰ This overestimate of n_i may be due to additional ion current induced by secondary electron emission from the tip surface as a result of bombardment of ions, energetic neutrals, and plasma radiation. The electron density may be affected by the reflection and re-emission of electrons on the tip surface. Hence, the values of n_i and n_e should be considered as the upper and lower limits of the plasma density, respectively.³⁰ Figure 4.1(a) also shows there is little variation of n_i and n_e as a function of pressure in the range from 30 mTorr to 50 mTorr.

Electron temperature is an important parameter for low-pressure plasmas because it governs the rates of ionization, dissociation, and excitation processes. Figure 4.1(b) shows the variation of electron temperature as a function of power and pressure. An inverse dependence of T_e on power is observed as power is increased from 30 W to 150 W. This is different from common observations in true ICPs, in which T_e is independent of P .³¹ From Figure 4.1(b), an abrupt drop in T_e (from ~5.0 eV to ~3.7 eV) occurs between 50 W and 90 W, which represents the transition from the dim E mode (30 W to 50 W) to the bright H mode (>90 W). The mechanisms of the E-to-H transition for ICPs have been investigated in detail by Turner et al.³² and Marakhtanov et al.,³³ and similar transitions are found in other studies of ICPs.^{13,34} In

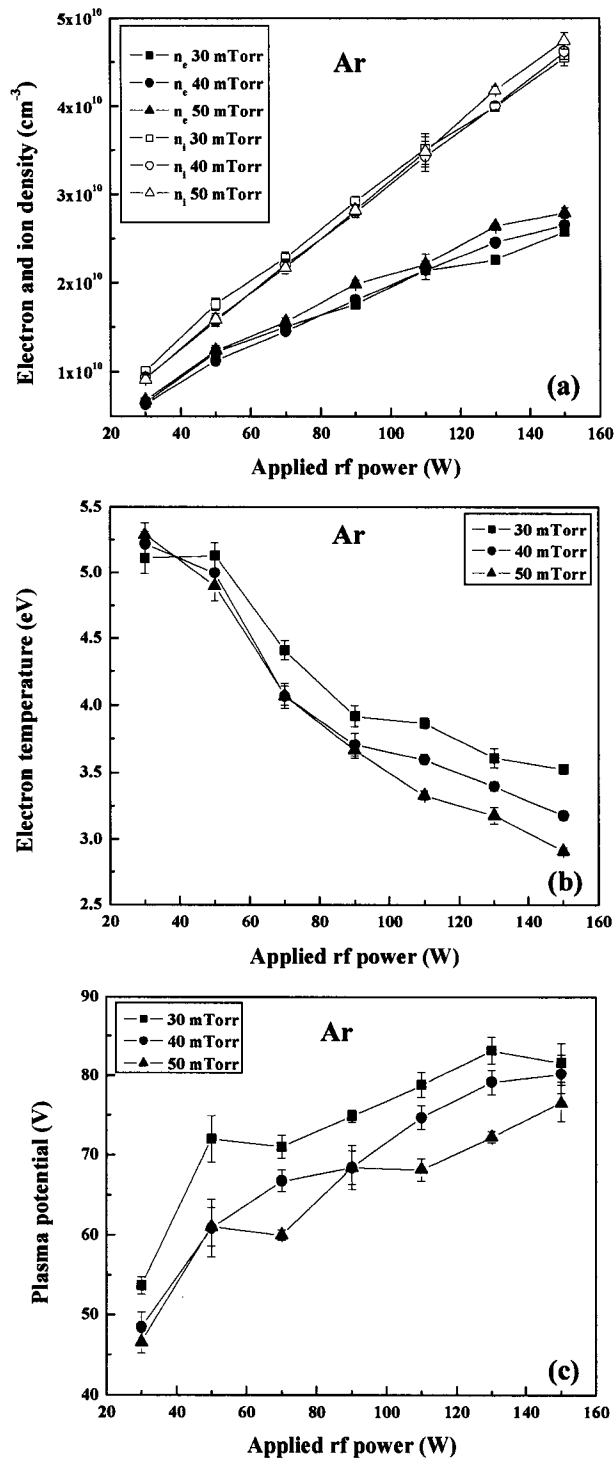


Figure 4.1. Langmuir probe data for 100% argon plasma: (a) n_e and n_i ; (b) T_e ; (c) V_p as a function of pressure and P .

the H mode regime, a small decrease in T_e (from ~ 3.7 eV to ~ 3.2 eV) can be seen at higher powers. This is consistent with other results obtained in truly inductively coupled plasmas that show T_e is nearly independent of power.³¹ From Figure 4.1(b) it can also be seen that T_e increases with decreasing gas pressure in the H mode regime. In a steady state plasma, the global rates of creation and loss of ions are equal, and the balance between the total volume ionization and the loss of particles to the wall, neglecting the recombination of charged particles in the volume, has been derived:^{35,36}

$$\frac{K_{iz}(T_e)}{C_s(T_e)} = \frac{1}{n_g d_{eff}} \quad (9)$$

where K_{iz} is the rate constant for ionization, C_s is the ion sound speed, n_g is the neutral gas density, and d_{eff} is an estimated effective length of the discharge which depends on the chamber size and the fraction between the bulk and the edge plasma density. Hence, when the neutral gas density is increased by increasing the pressure, the ionization rate constant must decrease to maintain the particle balance, which requires a concomitant decrease in the electron temperature.

Plasma potential is another important parameter in low-pressure plasmas because the ion energy impinging on the substrate surface is usually determined by the potential difference between the plasma and substrate potentials. The variation of V_p as a function of power and pressure is shown in Figure 4.1(c). The V_p increases sharply when power is increased from 30 W to 70 W, then slightly increases at higher power. This also reflects the transition of the plasma from the dim E mode to the bright H mode. This decreased variation of V_p with power in the bright H regime is in agreement with results presented in other studies that V_p is not significantly affected by power in a true ICP.³¹ Figure 4.1(c) also demonstrates that V_p generally decreases

with increasing pressure over nearly the entire investigated power region; note that the values of V_p are somewhat overlapped at 40 mTorr and 50 mTorr.

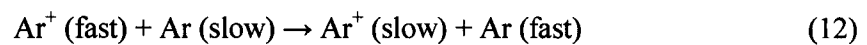
Figure 4.2 shows the IEDs of Ar^+ measured in Ar plasma molecular beams. As noted above, the shapes of the IEDs measured by sampling ions in the molecular beams are more complicated than those obtained by sampling ions through a small orifice on the electrode surface as a result of ion-neutral collisions that can occur when ions exit from a large plasma reactor orifice. Coburn and Kay examined the effects of collisions in this region,³⁷ and equated the variation of neutral flux with distance away from the orifice by equation 10,

$$n(z) = \frac{2F(z)}{\bar{c}} = \frac{n_b}{2} \frac{R^2}{R^2 + z^2} \quad (10)$$

where $F(z)$ is the flux of neutrals at an axial distance z away from the orifice with radius R ; n_b is the concentration of neutrals in the plasma well away from the orifice and \bar{c} is the average speed of the molecules [$\bar{c} = (8kT/\pi m)^{1/2}$]. The fraction of ions that pass through the orifice to a point $z = L$ without any collisions is given by equation (11),

$$\frac{N(z)}{N(0)} = \exp\left[\frac{-\sigma R n_0}{2} \arctan \frac{z}{R}\right] \quad (11)$$

where σ is the cross section for ion-molecule collisions and n_0 is the number density of molecules at $z = 0$. From equation (11), it is clear that the effect of ion-neutral collisions is greatest at high pressures and large orifice sizes. Figure 4.2 shows significant low-energy peaks in the IEDs of Ar^+ in all argon plasmas. The low-energy peaks in the Ar^+ IEDs are a result of energy exchange via ion-neutral collisions:



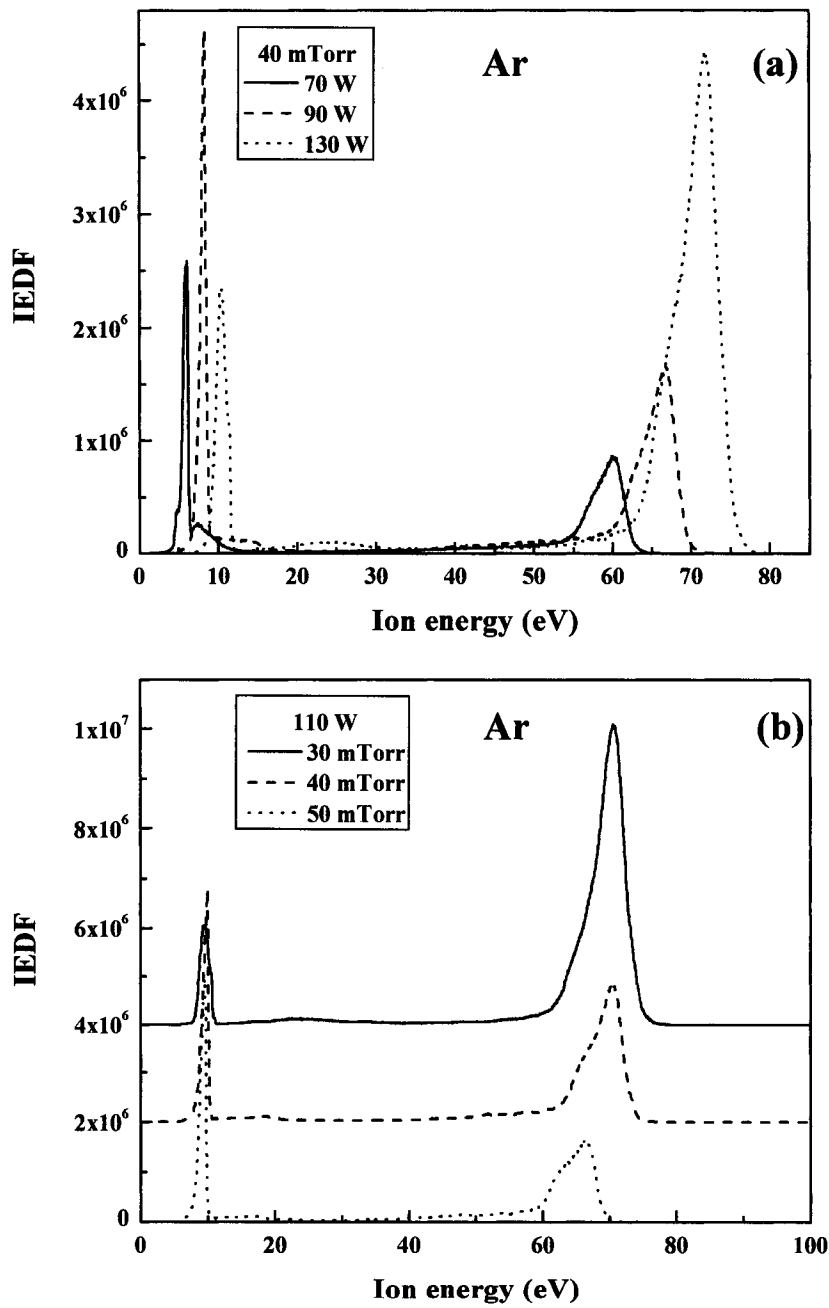


Figure 4.2. IEDs of Ar⁺ for 100% argon plasma: (a) at 40 mTorr, various powers; (b) at 110 W, various pressures.

where the energy of Ar^+ (fast) is controlled by V_p and the energy of Ar neutrals is much lower than 0.1 eV in the bulk plasma.²² This energy exchange can occur easily because of the high concentration of Ar neutrals in Ar plasmas. In contrast to the low-energy peaks, the high-energy peaks represent the energy of ions that do not collide with neutrals after passing through the reactor orifice. We can, therefore, estimate the fraction of ions that do not undergo ion-neutral collisions by separately integrating the low-energy and high-energy peaks. For 110 W argon plasmas, Figure 4.2(b), ~ 88%, 75% and 65% of the ions pass through the orifice of the plasma reactor without suffering ion-neutral collisions at 30, 40 and 50 mTorr, respectively. These values agree with equation (11) which shows that more ions will encounter ion-neutral collisions at higher pressure when exiting from the sampling orifice.

The profiles of high-energy peaks in the Ar^+ IEDs are nearly monoenergetic and represent the ion energy obtained by acceleration across the sheath electrical field. The values of these high-energy peaks are consistent with V_p values measured by the Langmuir probe. Note that Langmuir probe V_p values are about 2-6 eV higher than the values of the high-energy peaks in the IEDs. The shape and energy dispersion of IEDs has been discussed in detail by Kawamura et al.³⁸ Their analytical calculations show that the time an ion takes to traverse the sheath (τ_{trans}) and the period of the applied potential (τ_{rf}) are critical parameters in describing the shape of the IED. In high density plasmas, the sheath is thin and collisionless, and the ion mean free path is an order of magnitude larger than the sheath thickness, therefore $\tau_{trans}/\tau_{rf} \gg 1$. Consequently ions take many rf cycles to cross the sheath and respond only to an average sheath potential, resulting in an IED with a single energy peak with narrow energy spread (full width at half maximum (FWHM) ~ 5.0 eV). The ion energy is a result of the acceleration of ions across the potential difference of the sheath.

Additionally, numerous factors can contribute to the observed broadening for an IED, including effects from the initial ion energy in the presheath, thermal ion temperature in the bulk plasma, the stray capacitive component between the coil and the plasma, and instrumental energy resolution.³⁹

Usually, the average potential drop across the sheath or the self dc bias is taken to be representative of the ion energies bombarding the substrate, and process results such as etch or deposition rate and selectivity are related to the mean ion energy measured in this manner. In our studies, mean ion energies were calculated using the following equation:⁴⁰

$$\langle E_i \rangle = \frac{\int_0^{\infty} f(E)E dE}{\int_0^{\infty} f(E) dE} \quad (13)$$

where $f(E)$ is the ion energy distribution function. Note that the mean ion energy may not be representative of the actual energies of ions bombarding the substrate surface, especially in broad or multimodal distributions such as those measured in plasma molecular beams. In this work, the presence of low energy ions created by ion-neutral collisions near the reactor orifice has a significant effect on the mean ion energies. Figure 4.3 shows $\langle E_i \rangle$ for Ar^+ in Ar plasma molecular beams as a function of P at different pressures. The mean ion energy increases with increasing P and decreases with increasing pressure over the investigated range. Compared with the Langmuir probe results in Figure 4.1(c), the mean energies of Ar^+ are much lower than the plasma potentials. This is due to the contribution of low energy ions to the mean ion energy. Increased pressure results in increased availability of Ar neutrals for energy exchange reactions (Reaction 12). Consequently, there is a greater contribution of the lower ion energy component to the IED, which results in lower mean ion energies at higher pressures. Although mean ion energies are not good representations of the V_p

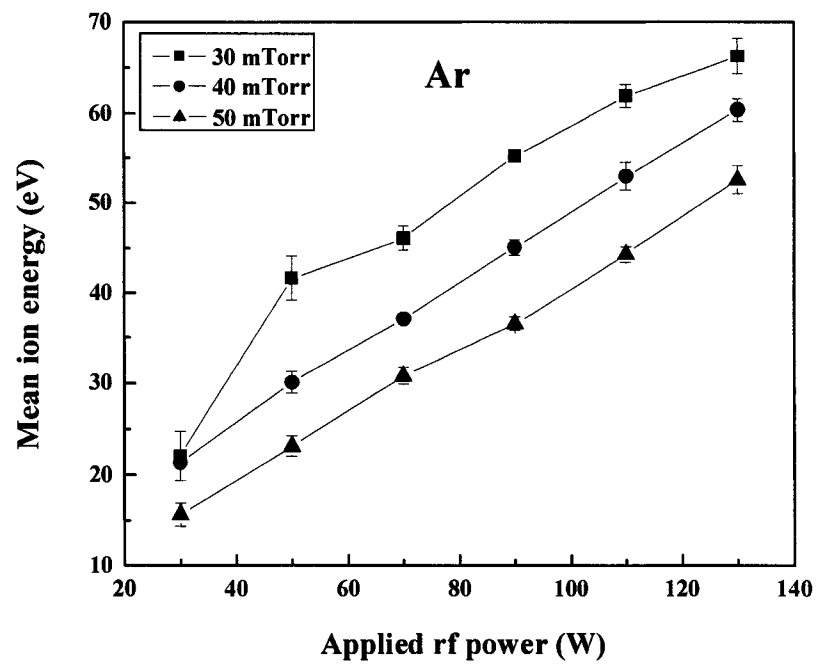


Figure 4.3. Mean energy of Ar^+ in 100% argon plasma as a function of pressure and power.

of these systems, the high ion energy of the IEDs corresponds well to V_p values measured by the Langmuir probe, as discussed above.

4.2.2. CH₄/Ar mixture. Recently, inert gases such as He, Ar, and Xe have been added to dilute the carbon containing precursor gases used in PECVD of DLC films. This is believed to assist the creation of plasmas in hydrocarbon gases and to enhance the plasma density.^{19,41} Therefore the characterization of gas-phase ion and electron kinetics in these plasmas is crucial to understand the mechanisms of DLC film growth. MS measurements show that there is a high concentration of multicarbon ions such as C₂H_y⁺, C₃H_y⁺, C_xH_y⁺ ($x \geq 4$) in the gas-phase of CH₄-containing plasmas. To suppress the formation of multicarbon ions, C_xH_y⁺ ($x \geq 4$), in the gas-phase, low CH₄ content CH₄/Ar plasmas (flow ratio, CH₄:Ar = 15:85) were used. Figure 4.4 shows Langmuir probe data, n_i , n_e , T_e and V_p collected for CH₄/Ar plasmas as a function of pressure and P . n_i and n_e increase slightly with increasing P from 30 W to 50 W and then increase nearly linearly at higher P . No significant dependence of n_e and n_i on pressure is observed, Figure 4.4(a). The variation of T_e with P and pressure is shown in Figure 4.4(b). A decrease in T_e with increasing P is typical in CH₄/Ar plasmas. This is similar to the observation made in 100% Ar plasmas that T_e is high in the E regime and low in the H regime. T_e in CH₄/Ar plasmas is, however, ~ 0.5 to 1.5 eV higher than that measured in 100% Ar plasmas under the same pressure and P .

From Figure 4.4(b), T_e in CH₄/Ar plasmas increases with increasing pressure. This is contrary to the observation made in pure Ar plasmas in which an inverse dependence of T_e on pressure is seen. This unusual variation has also been reported by Okada et al. in a low pressure CH₄/H₂ inductively coupled plasma.⁶ The assumptions of equation (9) are that the global ion loss rate in the volume is constant and that the recombination of charged particles in the volume can be neglected.

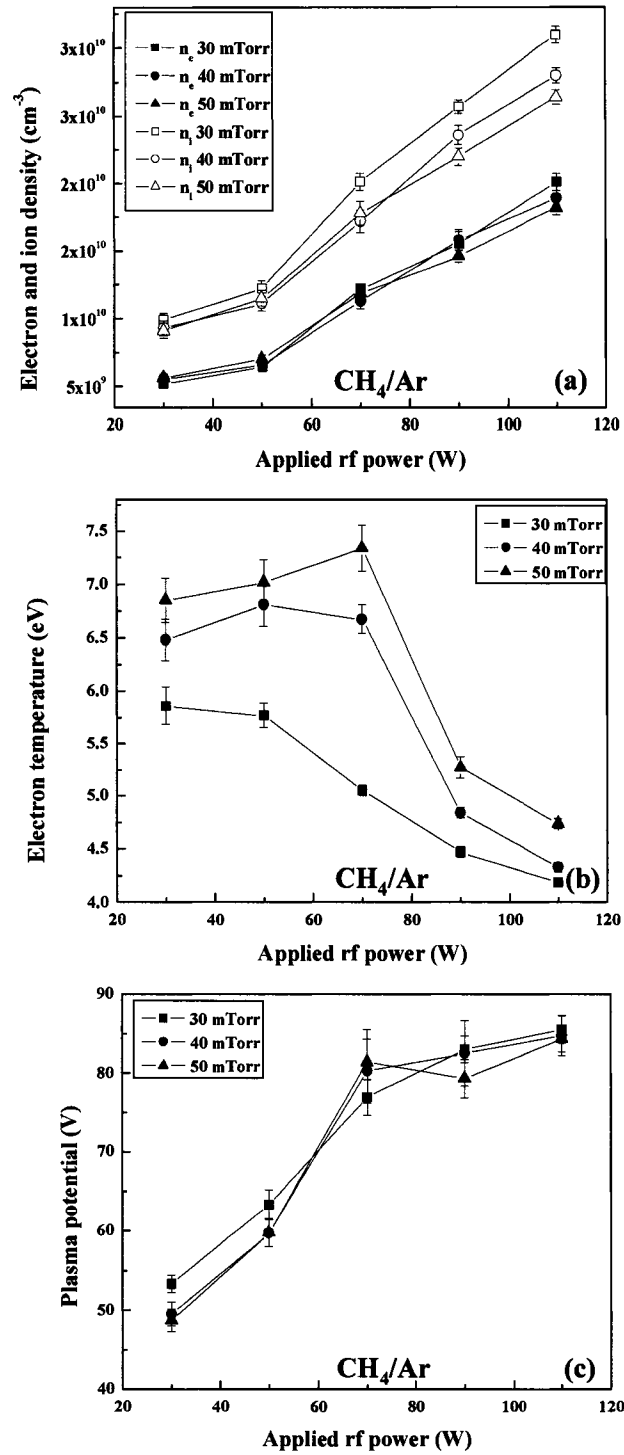


Figure 4.4. Langmuir probe data for 15:85 CH₄/Ar plasma: (a) n_e and n_i ; (b) T_e ; (c) V_p as a function of pressure and power.

However, this equation may not be valid for highly depositing discharges such as CH₄-containing plasmas. Highly depositing systems can have an increase of the ion loss rate to the walls or of the recombination of charged particles in the volume, which requires a higher T_e as compensation. Figure 4.4(c) shows the variation of V_p as a function of pressure and P . No clear dependence of V_p on pressure in the entire investigated range is present. V_p increases quickly in the transition region from E mode to H mode and then is almost constant at higher P .

The relative ion intensities in CH₄/Ar plasmas as a function of pressure and P are shown in Figure 4.5. It is clear that CH₃⁺ is the dominant ion in most cases except for the 30 mTorr plasmas with $P \geq 90$ W. Despite the large Ar fraction in the CH₄/Ar precursor gases, Ar⁺ is not a dominant ion in these plasmas. This can be explained using the electron impact ionization thresholds for the primary ions in CH₄/Ar plasmas, Table 4.1. The ionization energy of Ar is higher than that of hydrocarbons, which leads to a smaller fraction of Ar⁺ in the plasma. From Figure 4.5, ArH⁺ also appears to be a significant component in CH₄/Ar mixtures and its density increases significantly with increasing P . ArH⁺ ions are most likely created through the following reactions:



These reactions can serve as loss channels for Ar⁺. Although there is an expected abundance of neutral H in these discharges, the possibility of the creation of ArH⁺ through reaction (16)



is less than that through reaction (15) because the cross section for reaction (16) is smaller.³⁰ As evident from Figure 4.5, H⁺ and H₂⁺ contribute 1-2% of the total ion

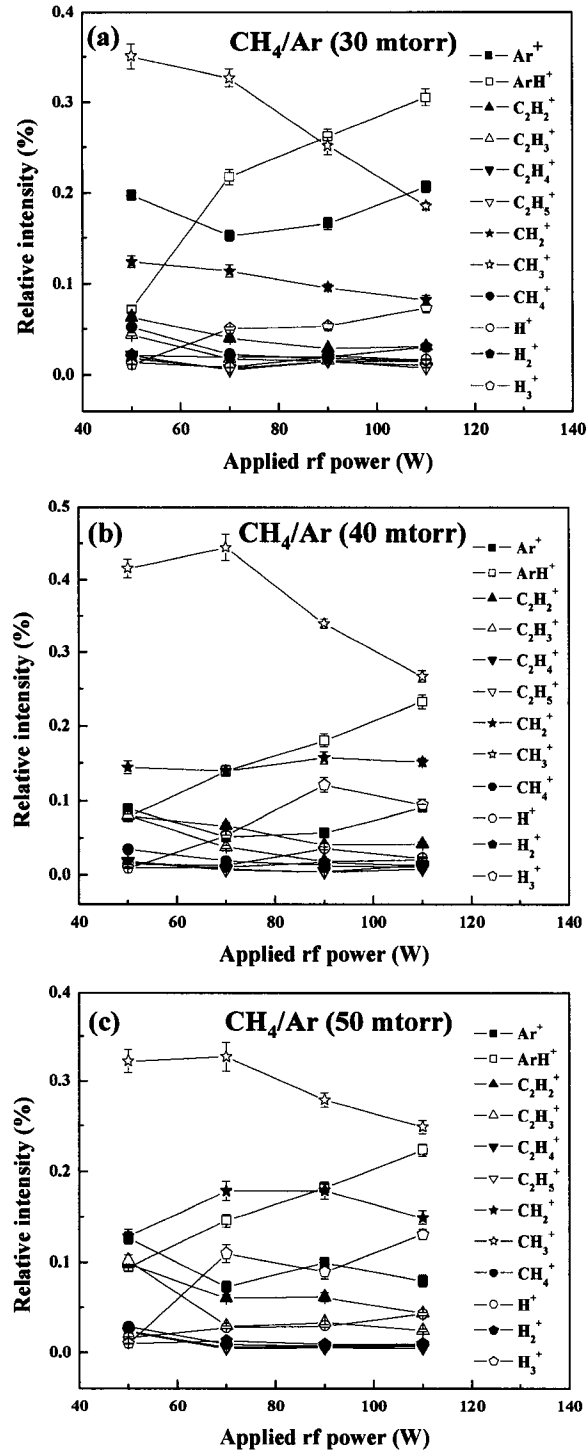


Figure 4.5. Relative ion intensity in the 15:85 CH₄/Ar plasmas as a function of power at: (a) 30 mTorr; (b) 40 mTorr; (c) 50 mTorr.

Table 4.1. Thresholds for primary electron impact ionization reactions in CH₄/Ar plasmas.^a

Reaction	Threshold energy (eV)
Ar + e → Ar ⁺ + 2e	15.75
CH ₄ + e → CH ₄ ⁺ + 2e	12.61
CH ₄ + e → CH ₃ ⁺ + H + 2e	14.00
CH ₄ + e → CH ₃ ⁺ + H ⁺ + e	13.30
CH ₃ + e → CH ₃ ⁺ + 2e	9.84
CH ₂ + e → CH ₂ ⁺ + 2e	10.40
CH + e → CH ⁺ + 2e	10.64
C + e → C ⁺ + 2e	11.26
H ₂ + e → H ₂ ⁺ + 2e	15.43
H + e → H ⁺ + 2e	13.60
C ₂ H ₆ + e → C ₂ H ₆ ⁺ + 2e	11.52
C ₂ H ₅ + e → C ₂ H ₅ ⁺ + 2e	8.12
C ₂ H ₄ + e → C ₂ H ₄ ⁺ + 2e	10.51
C ₂ H ₃ + e → C ₂ H ₃ ⁺ + 2e	8.25
C ₂ H ₂ + e → C ₂ H ₂ ⁺ + 2e	11.41
C ₂ H + e → C ₂ H ⁺ + 2e	11.61
C ₂ + e → C ₂ ⁺ + 2e	11.40

^a Values are taken from references^{22,42,43}

flux and are not clearly dependent on P . The major creation channels of H^+ and H_2^+ are through ionization by direct electron impact:



It can also be seen from Figure 4.5 that the relative H_3^+ flux is much higher than that of H^+ and H_2^+ , especially at higher P . The predominance of H_3^+ over H^+ and H_2^+ indicates the presence of secondary ion-molecule reactions such as $H_2^+ + H_2 \rightarrow H_3^+ + H$.^{21,22}

Figures 4.6 and 4.7 show the IEDs of the eight major ions Ar^+ , ArH^+ , CH_2^+ , CH_3^+ , $C_2H_2^+$, $C_2H_3^+$, H^+ , and H_3^+ measured in CH_4/Ar plasma molecular beams as a function of P and pressure. The IEDs of Ar^+ still exhibit intense low-energy peaks as seen in the 100% Ar plasmas. However, the IEDs of other ions show very low intensity low-energy peaks. For example, for CH_4/Ar plasma molecular beams (130 W, 40 mTorr), the fractions of low-energy peaks in the IEDs of Ar^+ , ArH^+ , CH_2^+ , CH_3^+ , $C_2H_2^+$, $C_2H_3^+$, H^+ , and H_3^+ are 38.9%, 4.0%, 0.4%, 0.5%, 2.5%, 1.6%, 8.0%, and 1.0%, respectively. As discussed above, the large low-energy peaks in the IEDs of Ar^+ are caused by energy exchange via collisions between fast Ar^+ and slow Ar neutrals. However, the small fraction of the low-energy peaks in the IEDs of other intermediate ions indicates that only a few of these ions undergo energy exchange via collisions, even though there is a large concentration of slow Ar neutrals near the orifice. This indicates that energy exchange via collisions between the other intermediate ions and Ar neutrals is less likely to happen, probably due to different collisional cross sections. Hence, the low-energy peaks measured in the molecular beams mainly arise from the energy exchange via collisions between the same kinds

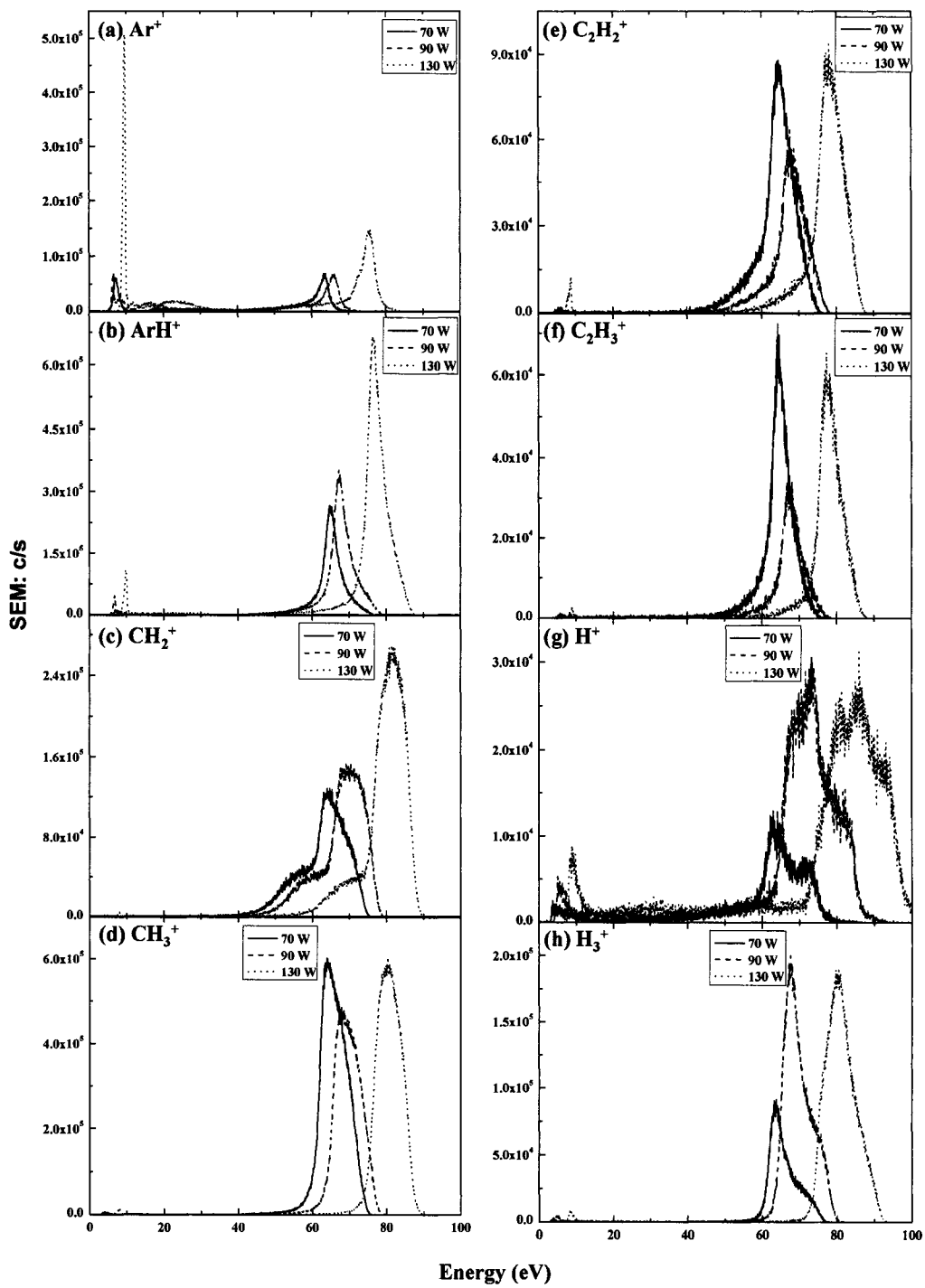


Figure 4.6. IEDs of (a) Ar^+ ; (b) ArH^+ ; (c) CH_2^+ ; (d) CH_3^+ ; (e) C_2H_2^+ ; (f) C_2H_3^+ ; (g) H^+ ; (h) H_3^+ in 15:85 CH_4/Ar plasma at 40 mTorr, various powers.

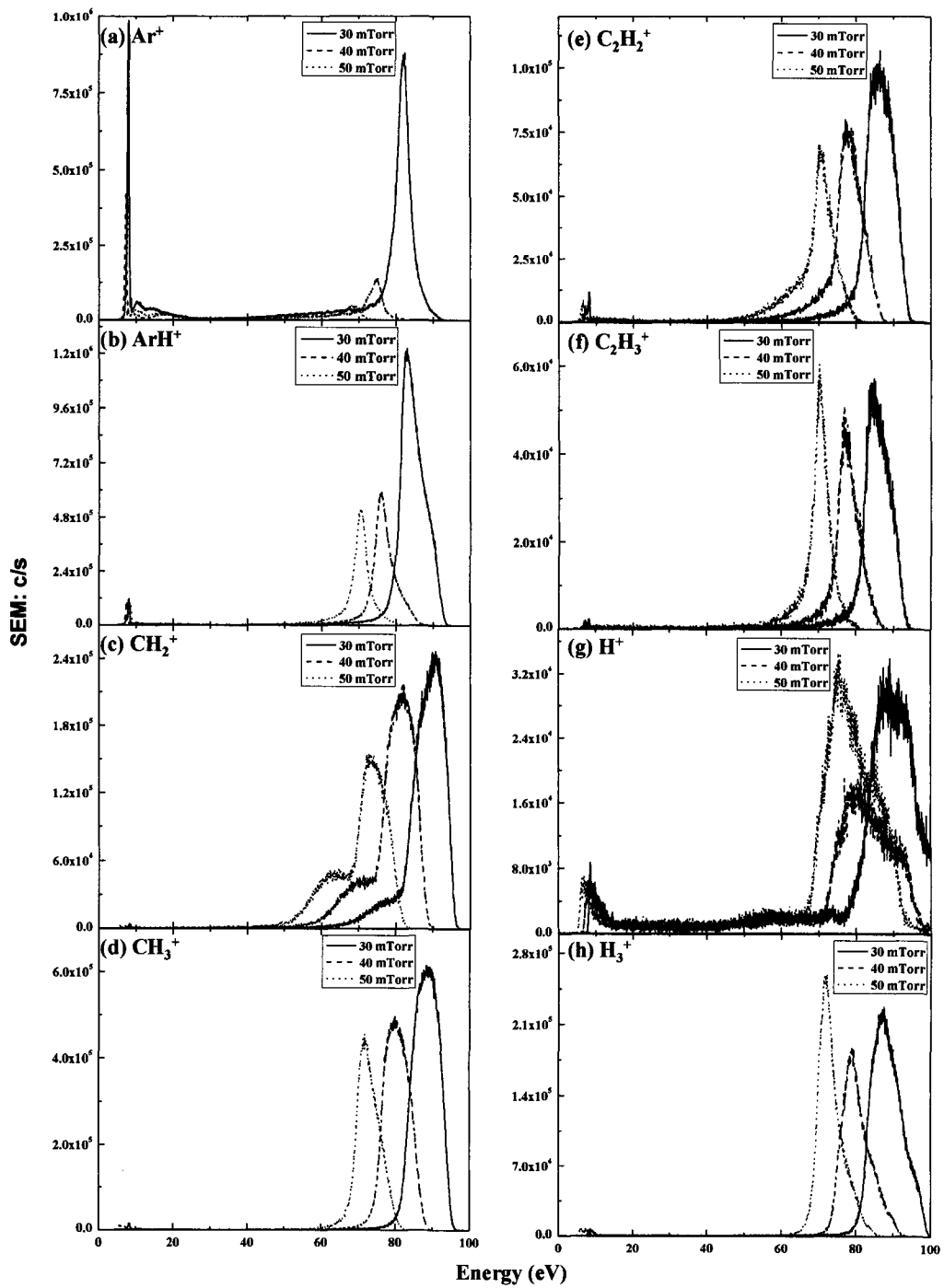


Figure 4.7. IEDs of (a) Ar^+ ; (b) ArH^+ ; (c) CH_2^+ ; (d) CH_3^+ ; (e) C_2H_2^+ ; (f) C_2H_3^+ ; (g) H^+ ; (h) H_3^+ in 15:85 CH_4/Ar plasma at 110 W, various pressures.

of ions and neutrals. As shown above, about 8% of H^+ encounters energy exchange through ion-neutral collisions because there is a large concentration of H neutrals in hydrocarbon containing plasmas.^{41,42} Compared with the IEDs of Ar^+ and H^+ , the small low-energy peaks in the IEDs of CH_2^+ , CH_3^+ , $C_2H_2^+$, $C_2H_3^+$, and H_3^+ indicate that there is a small number of the corresponding neutral species in the plasma.

The shapes of the high-energy peaks in the IEDs are also shown in Figures 4.6 and 4.7. From Figure 4.7, the high-energy peaks in the IEDs of Ar^+ increase with decreasing pressure similar to that in the IEDs of Ar^+ measured in the 100% Ar plasmas as a result of fewer ion-neutral collisions near the orifice at low pressures. The shapes of the high-energy peaks of heavier ions, such as Ar^+ , ArH^+ , CH_3^+ , $C_2H_2^+$, $C_2H_3^+$ are nearly Gaussian, whereas the lighter ions, such as H^+ , H_3^+ , and CH_2^+ exhibit broad multi-peaked IEDs. The energy spread (ΔE) by rf modulation is known to increase with decreasing ion mass (m) as $\Delta E \sim m^{-1/2}$.²² The transit time across the sheath for heavier ions is much longer than the rf cycle, which yields a bimodal ion energy distribution with two peaks lying close together. In contrast, lighter ions traverse the sheath faster and the ion energy is strongly modulated by rf cycle, which leads to substantial broadening with a width on the order of the peak-to-peak rf voltage.^{21,22,38} This is more obvious in the IEDs of H^+ .

The mean ion energies of Ar^+ and CH_3^+ calculated by equation (13) are shown in Figure 4.8. The mean energy of Ar^+ is much less than that of CH_3^+ under the same conditions, which reflects that more Ar^+ ions than CH_3^+ ions undergo energy exchange via ion-neutral collisions. The mean energies for both Ar^+ and CH_3^+ increase with decreasing pressure. At 30 mTorr, the mean energy of CH_3^+ is almost equal to the V_p measured by Langmuir probe. Therefore the IEDs of intermediate

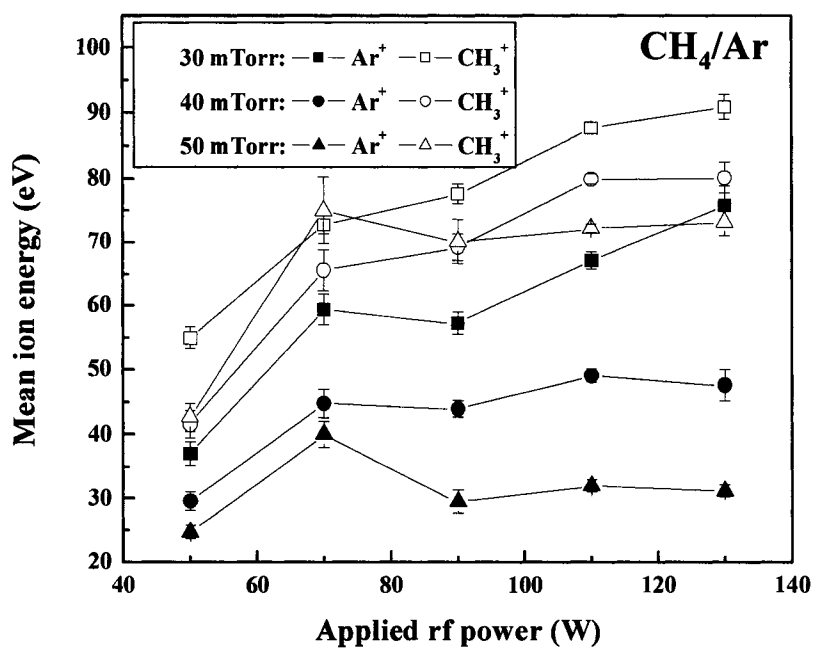


Figure 4.8. Mean energy of Ar⁺ and CH₃⁺ in 15:85 CH₄/Ar plasma as a function of power at three different reactor pressures.

ions measured at low pressure can be a good reflection of the ion energy obtained as the ions cross the sheath inside the plasma reactor.

Figures 4.9(a) and 4.9(b) show the EEDFs of Ar and CH₄/Ar plasmas at different P and pressures. The inaccuracy in the EEDFs obtained at low electron energy for both Ar and CH₄/Ar plasmas could be from larger experimental uncertainties caused by fluctuation of the time-averaged plasma potential.¹⁰ For 100% Ar plasmas, the EEDFs exhibit Maxwellian distributions when the electron energy is lower than 15 eV. At higher electron energies (>15 eV), a depletion is apparent due to the inelastic collisions and loss of high-energy electrons to the reactor walls.⁴⁴ No clear dependence on pressure in the EEDFs can be seen. However, at higher P , the slopes of the EEDFs are more negative, which indicates a lower T_e because the slope in the EEDF with a Maxwellian distribution function is equal to $(-1/kT_e)$.¹⁰ From Figure 4.9(b), the EEDFs in CH₄/Ar plasmas maintain a Maxwellian distribution up to an energy of 18 eV, beyond which the EEDFs are depleted. The variations of the EEDFs with pressure and P in CH₄/Ar plasmas are similar to those observed in 100% Ar plasmas. When P is low, less negative slopes in the EEDFs can be observed clearly in the CH₄/Ar plasmas, indicating a higher T_e . This is consistent with the results shown above.

4.2.3. Effect of ion energy on the properties of DLC films. DLC films were deposited at different substrate potentials (V_{sub}) as described in Chapter 2.1.3. FTIR spectroscopy was used to determine the local environment of carbon bonding and the content of hydrogen in DLC films, Figure 4.10. Prominent spectral features include the absorption peaks at 2956 cm⁻¹, 2932 cm⁻¹, and 2872 cm⁻¹ which correspond to sp^3 asymmetrical CH₃, sp^3 CH₂, and sp^3 CH₃ stretching modes, respectively.^{12,15} The absorption intensities of all three C-H vibrations decrease significantly when a

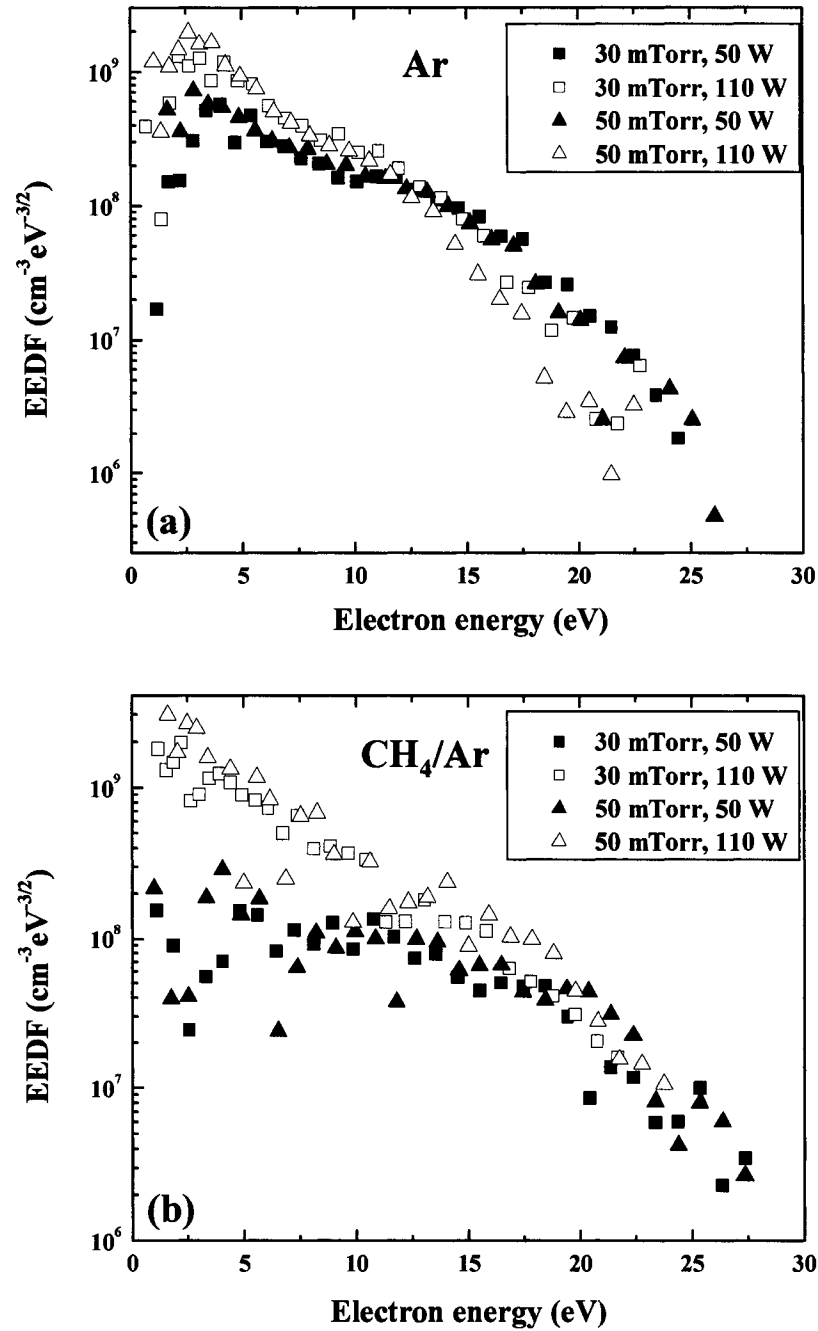


Figure 4.9. EEDFs measured at 30 and 50 mTorr, 50 and 110 W in (a) Ar plasmas and (b) 15:85 CH₄/Ar plasmas.

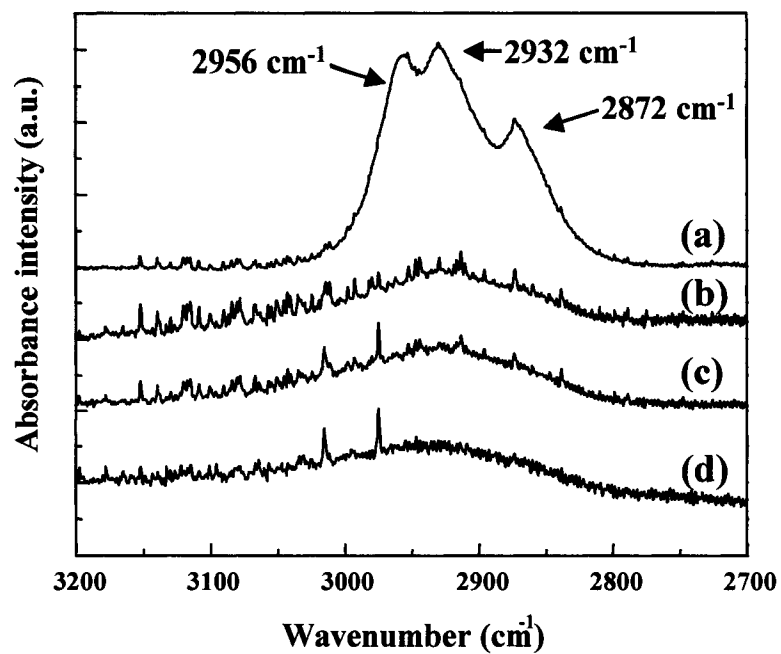


Figure 4.10. FTIR spectra of DLC films (normalized by the thickness of the films) deposited at different substrate potentials, (a) 50 V; (b) -50 V; (c) -100 V; (d) -150 V in the 2700 – 3200 cm^{-1} range.

negative bias potential is applied to the substrate, Figure 4.10. No obvious change in the absorption intensities of these C-H vibrations was found when the negative bias potential increased from -50 V to -150 V.

The deposition rates of DLC films were determined using the SEM cross-section images shown in Figure 4.11. Deposition rates with substrate potentials of 50 V, -50 V, -100 V, and -150 V are 75.1 ± 3.1 , 21.2 ± 0.6 , 16.6 ± 0.3 , and 15.3 ± 0.2 nm/min, respectively. Figure 4.12 shows the morphologies of the hydrogenated DLC films deposited at various substrate potentials using AFM. The root-mean-square (RMS) roughness of the film deposited with a substrate potential of 50 V is 2.85 ± 0.09 nm. Changing the substrate potential to -50 V, -100 V, and -150 V yields much smaller roughness values of 0.104 ± 0.005 nm, 0.105 ± 0.004 nm, and 0.086 ± 0.004 nm, respectively. The hardness and Young's modulus of the DLC films as a function of substrate potential are shown in Figure 4.13. The hardness and Young's modulus of the film deposited with the substrate potential of 50 V are 0.49 ± 0.05 GPa and 9.95 ± 0.65 GPa, respectively, which represents a soft polymer-like film. However, when a substrate potential of -50 V is applied, the hardness and Young's modulus of the film increase significantly to 13.1 ± 0.3 GPa and 130.7 ± 2.1 GPa, respectively. With increased negative biases, the hardness and Young's modulus reach a maximum at $V_{sub} = -100$ V (15.3 ± 0.4 GPa and 138.3 ± 2.8 GPa, respectively) and drop slightly at $V_{sub} = -150$ V (12.5 ± 0.3 GPa and 131.1 ± 2.5 GPa, respectively). Because the ion energy impinging on the silicon wafers is approximately equal to $(V_p - V_{sub})$, the results above indicate that the ion energy has a significant influence on the surface and mechanical properties of the hydrogenated DLC films.

With our current experimental apparatus, the ion flux and ion energy are independently controlled by the coil power and the substrate potential, respectively.

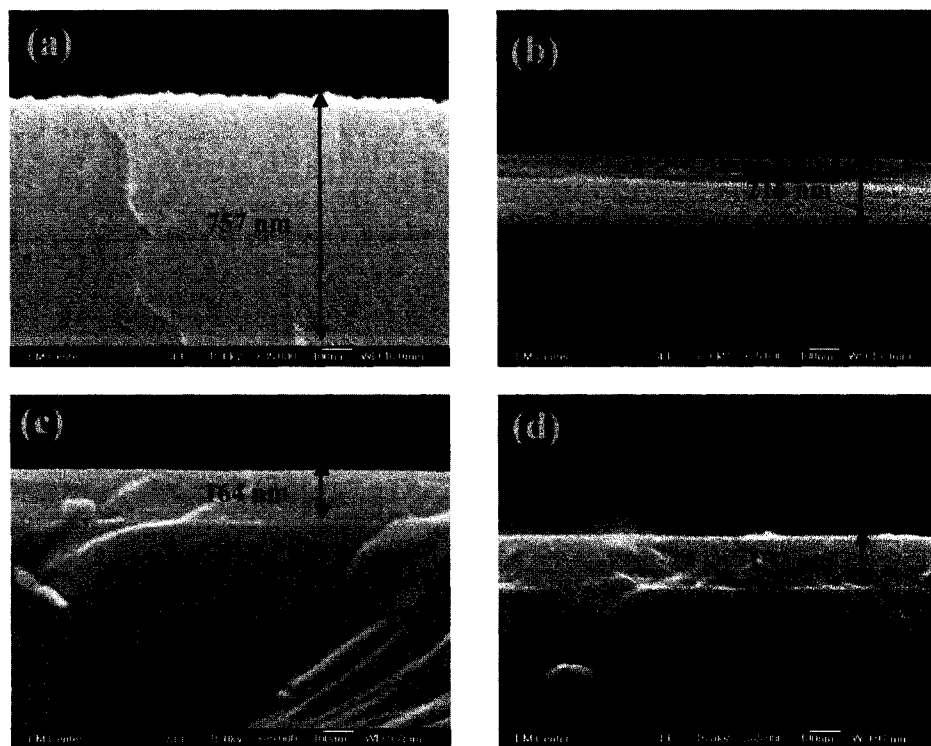


Figure 4.11. SEM cross-sectional images of DLC films deposited at different substrate potentials: (a) 50 V; (b) -50 V; (c) -100 V; (d) -150 V. The magnification for all images was fixed at 85,000.

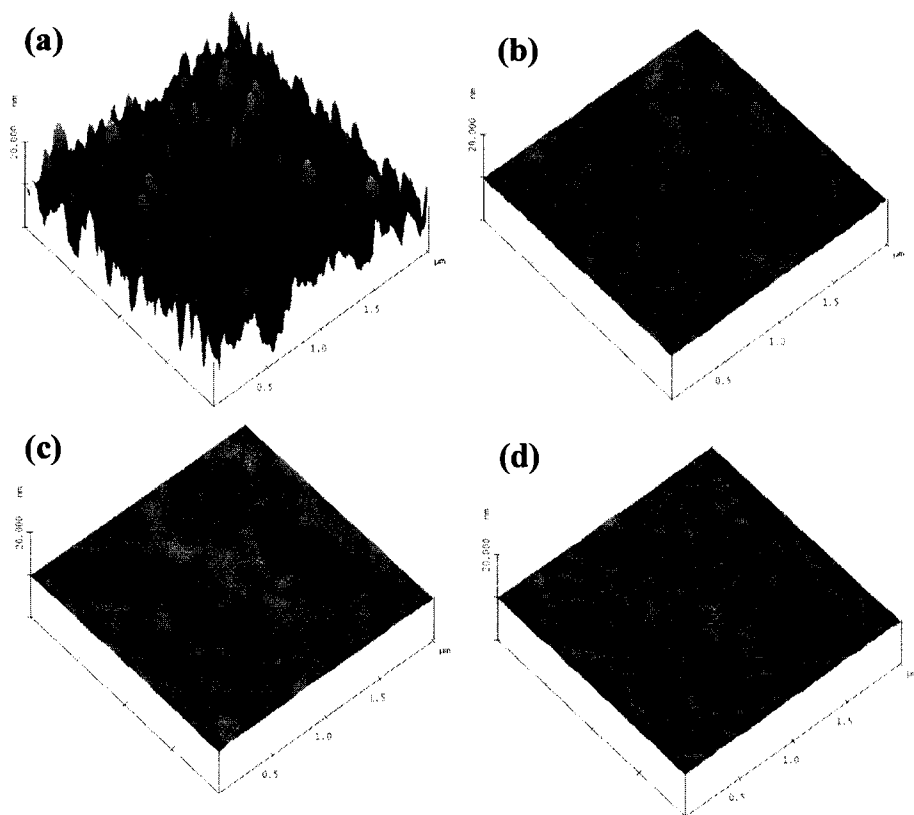


Figure 4.12. AFM images of DLC films deposited at different substrate potentials: (a) 50 V; (b) -50 V; (c) -100 V; (d) -150 V. RMS roughness values are 2.85 ± 0.09 , 0.104 ± 0.005 , 0.105 ± 0.004 , and 0.086 ± 0.004 nm, respectively.

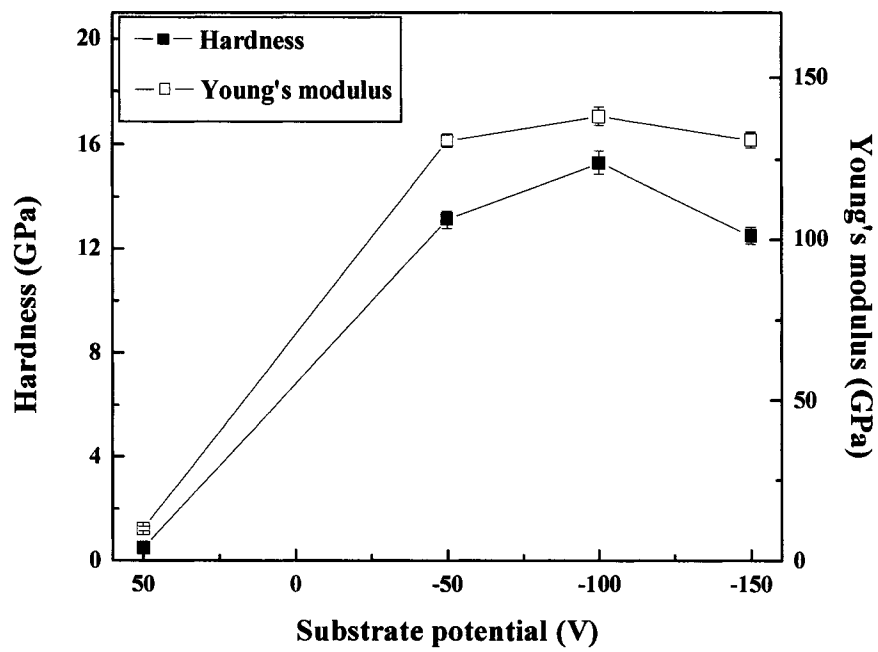


Figure 4.13. Hardness (■) and Young's modulus (□) of the DLC films as a function of substrate potential.

Because the coil power and pressure inside the reactor are fixed during the deposition processes, the ion flux and radical flux in the plasmas should be approximately constant, although there may be a slight increase in the ion or radical flux due to the substrate rf power. We assume that $V_p \sim 80$ eV during the deposition processes, based on the diagnostic results for CH₄/Ar plasmas. Hence, when the applied substrate power is 0 W, the ion energy bombarding the silicon wafers should be ~ 30 eV because the substrate potential is 50 V during the deposition. As noted above, radicals have very low energy. Therefore, the growth of the hydrogenated carbon films in this case is mainly controlled by radicals and low-energy ions.

According to CVD and PECVD mechanisms for hydrogenated DLC films, based on the ion-stitching model¹⁸ and the ion sub-plantation model,²⁰ low-energy hydrocarbon ions impinge upon the substrate surface and create radical sites on the surface. The neutral hydrocarbon radicals are then absorbed at these sites, leading to film growth. Because ions have insufficient energy to break C-H bonds, the films formed under these conditions have a large number of C-H bonds and less tetrahedral carbon network in the films. As can be seen in Figures 4.10-4.13, the film deposited here is a soft polymer-like carbon film (0.49 ± 0.05 GPa) with a high deposition rate and large roughness value. However, when negative substrate biases are applied, the significant decreases in the deposition rate, hydrogen content, and surface roughness and concomitant increase in the hardness indicate that ion energy plays a key role on the surface and structural properties of the hydrogenated DLC films. Note that the ion and radical fluxes are nearly constant under these conditions. Thus, these high-energy hydrocarbon ions can actually etch C-H and weak C-C bonds, penetrate into the sub-surface to form the carbon network consisting of more sp^3 carbon atoms. Therefore, the growth of hydrogenated DLC films in our plasma system is a result of competition

reactions between deposition by low-energy ions or radicals and sputter etching by high-energy ions. The quality and hardness of DLC films are ultimately determined by the content of sp^3 carbon atoms forming a carbon network.

4.3. Conclusions

A new molecular beam-based vacuum system was constructed to measure gas-phase characteristics of Ar and CH₄/Ar plasmas used for DLC deposition. The instrument has both MS and Langmuir probe capabilities. An rf-compensated Langmuir probe was used to measure n_e , T_e , n_i , V_p , and EEDF in Ar and Ar/CH₄ inductively coupled rf plasmas. At low P , relatively low electron and ion densities and high electron temperature were found in both Ar and CH₄/Ar plasmas as a result of electrostatic (capacitive) coupling (E mode). When P was increased, the plasma transitions to the electromagnetic (inductive) coupling (H mode) with high electron and ion densities and low electron temperature.

Relative ion intensities, IEDs and mean ion energies were measured in molecular beams of Ar and CH₄/Ar plasmas by a mass-resolved ion energy analyzer. CH₃⁺ is the dominant ion in most cases for the CH₄/Ar plasmas and its flux was observed to increase with P . The relative intensities of ArH⁺ and H₃⁺ also increase with increasing P . Significant low-energy peaks in the IEDs of Ar⁺ can be seen in both the Ar and CH₄/Ar plasmas due to the energy exchange via ion-neutral collisions near the reactor orifice. The intensities of these low-energy peaks significantly decrease as pressure decreases. High-energy peaks in the IEDs of heavier ions, Ar⁺, ArH⁺, CH₃⁺, C₂H₂⁺, C₂H₃⁺ exhibit narrow, near-Gaussian peaks whose values are consistent with the plasma potentials measured by the Langmuir probe. The FWHM for these ions is in the range of 3-5 eV. However the high-energy peaks in the IEDs

of lighter ions, H^+ , H_3^+ , and CH_2^+ exhibit broad multi-peaked IEDs due to the fast transit time cross the sheath. The IEDs of all ions except that of Ar^+ show small low-energy peaks as a result of the low probability energy exchange via ion-neutral collisions.

Hydrogenated DLC films were deposited on silicon wafers at different substrate potentials produced by an independently controlled 13.56 MHz rf generator. The hydrogen content, surface roughness and deposition rate significantly decrease, whereas the hardness of the films increases dramatically when negative biases were applied. Based on these results, ion energy has a critical influence on the structure and mechanical properties of DLC films. The growth of DLC films in our plasma system is controlled by competition reactions between deposition by radicals or low-energy ions and etching by high-energy ions.

References

- (1) Kim, H.; Jung, D. H.; Park, B.; Yoo, K. C.; Lee, J. J.; Joo, J. H. *Surf. Coat. Technol.* **2005**, *193*, 255.
- (2) Haverkamp, J.; Mayo, R. M.; Bourham, M. A.; Narayan, J.; Jin, C.; Duscher, G. *J. Appl. Phys.* **2003**, *93*, 3627.
- (3) Grill, A. *Cold Plasma in Material Fabrication from Fundamentals to Applications*; IEEE Press: New York, **1993**.
- (4) Robertson, J. *Adv. Phys.* **1986**, *35*, 317.
- (5) Bachmann, P. *Phys. World* **1991**, *4*, 32.
- (6) Okada, K.; Komatsu, S.; Matsumoto, S. *J. Vac. Sci. Technol. A* **1999**, *17*, 721.
- (7) Kang, B.; Park, J.; Kim, Y. H. *IEEE Trans. on Plasma Sci.* **2001**, *29*, 383.
- (8) Gorla, C. R.; Liang, S.; Tompa, G. S.; Mayo, W. E.; Lu, Y. *J. Vac. Sci. Technol. A* **1997**, *15*, 860.
- (9) Colpo, P.; Ceccone, G.; Sauvageot, P.; Baker, M.; Rossi, F. *J. Vac. Sci. Technol. A* **2000**, *18*, 1096.
- (10) Hong, J.; Granier, A.; Leteinturier, C.; Peignon, M. *J. Vac. Sci. Technol. A* **2000**, *18*, 497.
- (11) Chiu, K. F. *J. Electrochem. Soc.* **2004**, *151*, A1865.
- (12) Watanabe, T.; Yamamoto, K.; Tsuda, O.; Tanaka, A.; Koga, Y.; Takai, O. *Jpn. J. Appl. Phys.* **2002**, *41*, 6165.
- (13) Sun, Z.; Xu, S.; Ostrikov, K. N.; Tsakadze, E. L.; Tsakadze, Z. L. *Inst. J. Mod. Phys. B* **2002**, *16*, 836.
- (14) Kinoshita, H.; Otaka, N. *J. Vac. Sci. Technol. A* **2002**, *20*, 1481.
- (15) Park, K. C.; Moon, J. H.; Jang, J.; Oh, M. H. *Appl. Phys. Lett.* **1996**, *68*, 3594.

- (16) Yang, W. J.; Choa, Y.; Sekino, T.; Shim, K. B.; Niihara, K.; Auh, K. H. *Mater. Lett.* **2003**, *57*, 3305.
- (17) Mutsukura, N.; Handa, Y. *Plasma Chem. Plasma Proc.* **2002**, *22*, 607.
- (18) Cicala, G.; Bruno, P.; Losacco, A. M. *Diam. Relat. Mater.* **2004**, *13*, 1361.
- (19) Chakrabarti, K.; Kim, J. B.; Wilson, J. I. B.; Lee, C. *Phys. Stat. Sol. (a)* **2002**, *194*, 112.
- (20) Li, H.; Xu, T.; Chen, J.; Zhou, H.; Liu, H. *J. Phys. D: Appl. Phys.* **2003**, *36*, 3183.
- (21) Okada, K.; Komatsu, S.; Matsumoto, S. *J. Vac. Sci. Technol. A* **2003**, *21*, 1988.
- (22) Teii, K.; Hori, M.; Goto, T. *J. Appl. Phys.* **2002**, *92*, 4103.
- (23) Fisher, E. R. *Plasma Sources Sci. Technol.* **2002**, *11*, A105.
- (24) Fisher, E. R. *Plasma Process. Polym.* **2004**, *1*, 13.
- (25) Martin, I. T.; Fisher, E. R., manuscript in preparation.
- (26) Martin, I. T.; Fisher, E. R. *J. Vac. Sci. Technol. A* **2004**, *22*, 2168.
- (27) Liu, D.; Martin, I. T.; Zhou, J.; Fisher, E. R. *Pure Appl. Chem.* **2005**, Submitted for publication.
- (28) Thompson, B. E.; Allen, K. D.; Richards, A. D.; Sawin, H. H. *J. Appl. Phys.* **1986**, *59*, 1890.
- (29) Wild, C.; Koidl, P. *J. Appl. Phys.* **1991**, *69*, 2909.
- (30) Kim, J. S.; Rao, M. V. V. S.; Cappelli, M. A.; Sharma, S. P.; Meyyappan, M. *Plasma Sources Sci. Technol.* **2001**, *10*, 191.
- (31) Kim, C. *Korean J. Chem. Eng.* **2004**, *21*, 746.
- (32) Turner, M. M.; Lieberman, M. A. *Plasma Sources Sci. Technol.* **1999**, *8*, 313.
- (33) Marakhtanov, A. M.; Tuszewski, M.; Lieberman, M. A.; Lichtenberg, A. J.; Chabert, P. *J. Vac. Sci. Technol. A* **2003**, *21*, 1849.

- (34) Fuller, N. C. M.; Malyshev, M. V.; Donnelly, V. M.; Herman, I. P. *Plasma Sources Sci. Technol.* **2000**, *9*, 116.
- (35) Aanesland, A.; Fredriksen, A. *J. Vac. Sci. Technol. A* **2001**, *19*, 2446.
- (36) Lieberman, M. A.; Lichtenberg, A. J. *Principles of Plasma Discharges and Materials Processing*; Wiley: New York, **1994**.
- (37) Coburn, J. W.; Kay, E. *J. Vac. Sci. Technol.* **1971**, *8*, 738.
- (38) Kawamura, E.; Vahedi, V.; Lieberman, M. A.; Birdsall, C. K. *Plasma Sources Sci. Technol.* **1999**, *8*, 45.
- (39) Sobolewski, M. A.; Wang, Y.; Goyette, A. *J. Appl. Phys.* **2002**, *91*, 6303.
- (40) Edelberg, E. A.; Perry, A.; Benjamin, N.; Aydil, E. S. *J. Vac. Sci. Technol. A* **1999**, *17*, 506.
- (41) Riccardi, C.; Barni, R.; Sindoni, E.; Fontanesi, M.; Tosi, P. *Vacuum* **2001**, *61*, 211.
- (42) Morrison, N. A.; William, C.; Milne, W. I. *J. Appl. Phys.* **2003**, *94*, 7031.
- (43) NIST Chemical Webbook <http://webbook.nist.gov>, **2002**.
- (44) Seo, D. C.; Chung, T. H.; Yoon, H. J.; Kim, G. H. *J. Appl. Phys.* **2001**, *89*, 4218.

CHAPTER 5

EFFECTS OF ARGON DILUTION ON THE TRANSLATIONAL AND ROTATIONAL TEMPERATURES OF SiH IN SILANE AND DISILANE PLASMAS

Reprinted with permission from Jie Zhou, Jianming Zhang, and Ellen R. Fisher, *J. Phys. Chem. A*, **109** (46), 10521-10526, 2005

This dissertation chapter contains results from a full paper published in the *Journal of Physical Chemistry A*. The manuscript was written by Jie Zhou and edited by Ellen R. Fisher. The coauthor was Jianming Zhang, who helped to collect the data. This chapter describes the effects of argon dilution on the translational and rotational temperatures of SiH in both silane and disilane plasmas using the imaging of radicals interacting with surfaces (IRIS) technique. The underlying chemistry and mechanisms of SiH energy equilibrium in Ar diluted plasmas have been discussed.

5.1. Introduction

Silane and disilane plasmas have been extensively applied to the deposition of hydrogenated amorphous silicon films (a-Si:H). These materials are widely used in microelectronic devices such as solar cells, thin film transistors, and flat panel displays.¹⁻⁶ During the deposition processes, neutral SiH_x ($x = 0-3$) species are considered as important precursors for film growth.^{1,7,8} Among these, the long-lived SiH_3 is considered the primary precursor for film growth, although the short-lived Si, SiH , and SiH_2 still have significant influence on film properties.^{3,9,10} Investigations of the surface interactions of these species are, therefore, of practical importance to the improvement of film characteristics.

Chemically active radicals can be easily created in low-temperature plasmas through electron impact dissociation of precursor molecules. This is primarily because electrons in these systems have relatively high temperatures (10^3 - 10^5 K) in comparison to the gas temperature ($<10^3$ K).¹¹ The precursor fragments can obtain different kinetic energies during the dissipation of excess energy as a result of differences in mass as well as energy transfer pathways. Therefore, knowledge of the energy partitioning among these species is a key component of the plasma chemistry occurring during film growth. In most silane or disilane plasmas, however, the SiH density is low due to its high gas-phase reactivity and surface sticking probability.^{1,2,12,13}

SiH in plasma systems can be examined using various gas-phase diagnostics. For example, laser-induced fluorescence (LIF) is a sensitive plasma diagnostic tool that has been used extensively to investigate the nature of a variety of plasma species, including the SiH radical. Data on relative or absolute gas-phase concentrations, gas and surface reactivity, and kinetic energy have all been obtained with LIF.^{2,11,14,15}

Combining LIF and plasma molecular beam technology, our imaging of radicals interacting with surfaces (IRIS) technique is particularly useful and versatile. IRIS can provide spatially and temporally resolved 2D images of plasma species of interest, and has been applied to measure the surface interactions and translational/rotational temperatures of probed species.¹⁶⁻¹⁸

Previously, we have measured the surface interactions as well as the rotational (Θ_R) and translational temperatures (Θ_T) for SiH radicals in 100% silane and disilane plasmas as a function of applied rf power (P).^{1,19} The SiH surface reactivity is near unity under all plasma conditions, showing no clear dependence on P , substrate temperature (T_S), and precursor gas. In addition, the average SiH rotational and translational temperatures were also independent of P and precursor gas, and were measured as ~ 600 K and ~ 1100 K for silane and disilane plasmas, respectively.¹ This difference between Θ_R and Θ_T indicates that SiH radicals are not in thermal equilibrium within the plasmas. A similar observation has also been made for OH in alkoxy silane/ O_2 plasmas, wherein $\Theta_T(OH)$ is significantly higher than $\Theta_R(OH)$, again indicating a non thermalized system.²⁰⁻²³ However, Θ_R and Θ_T for OH are nearly identical in H_2O plasmas, suggesting that OH radicals are in thermal equilibrium in this system.^{21,23} These results led us to hypothesize that radicals produced by unimolecular dissociation processes (such as in the H_2O system) are more likely to reach thermal equilibrium than molecules formed via bimolecular reactions, such as in the alkoxy silane/ O_2 systems.

The SiH results, however, would appear to disagree with this hypothesis, provided that SiH was formed through a stepwise dissociation process. Previously, we noted that SiH is formed by the direct electron-induced dissociation of SiH_4 , rather than via sequential dissociation of SiH_3 or SiH_2 .¹ Because this dissociation pathway

proceeds via a super-excited electronic transition state, this creation mechanism may result in the significant differences measured in the rotational and translational temperatures of SiH. Moreover, the extremely high gas-phase reactivity of SiH may also contribute to this discrepancy. Specifically, SiH is very reactive with SiH₄, such that the SiH radicals probed in the molecular beam are mainly produced close to the extraction orifice, and have undergone only ~5 collisions prior to exiting the reactor. Thus, there are not enough collisions to allow SiH to reach thermal equilibrium. One can expect that the discrepancy between Θ_R and Θ_T of SiH can be reduced or eliminated if there are more non-reactive collisions for SiH. Therefore, we have investigated the effects of argon dilution on Θ_T and Θ_R of SiH in both silane and disilane plasmas. The argon dilution in these systems can provide additional non-reactive-collisional cooling for SiH, as well as more information on the energetics characterization of reactive plasma species. The process of thermal equilibration of SiH radicals is also discussed.

5.2. Results

Figure 5.1 shows the two dimensional ICCD images of SiH LIF signals using a 100% Si₂H₆ plasma molecular beam ($P = 60$ W) at gate delays of 205, 505, 805, and 1105 ns. In these images, the plasma molecular beam moves from left to right and the laser is propagating from bottom to top. As the gate delay increases, the SiH LIF intensity decreases significantly due to the radiative decay of the excited SiH A²Δ state after laser excitation.¹ Figure 5.2a shows the corresponding x-cross sections of the SiH LIF images in Figure 5.1. For the shortest time interval, we observe a peak position shift of ~0.2 mm. Although the shifts of the maximum LIF intensity along the direction of the molecular beam can be seen in the cross sections, they are better

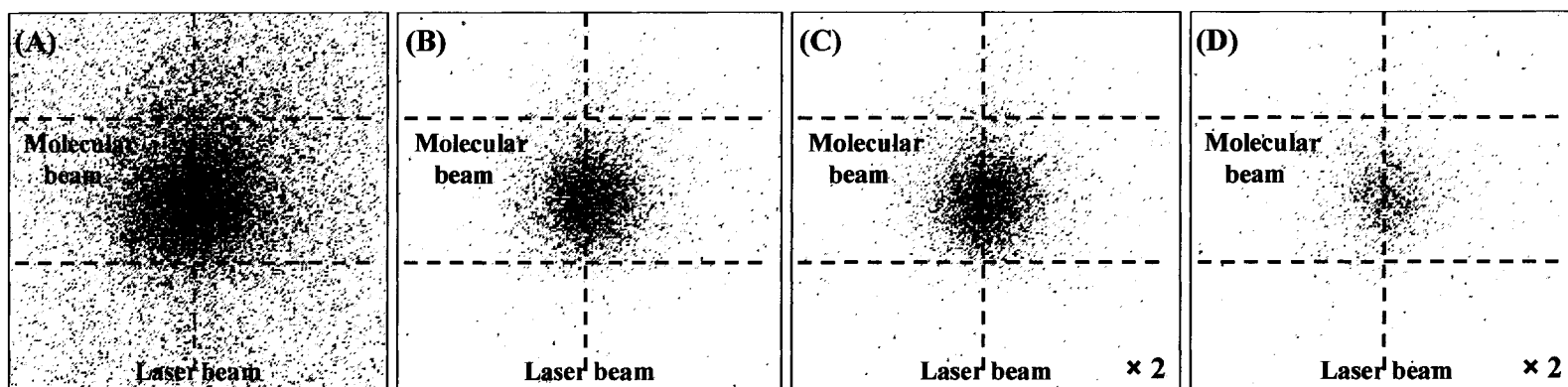


Figure 5.1. ICCD images of LIF signals for SiH radicals in a 100% Si₂H₆ plasma molecular beam ($P = 60$ W) at four different gate delays: (a) 205 ns, (b) 505 ns, (c) 805 ns, and (d) 1105 ns after laser excitation. Dashed lines indicate the locations of the molecular beam and the laser beam, which intersect each other at a 90° angle. The intensity scales in (a) and (b) are identical; due to the lower signal intensity in (c) and (d), the data have been multiplied by a factor of 2.

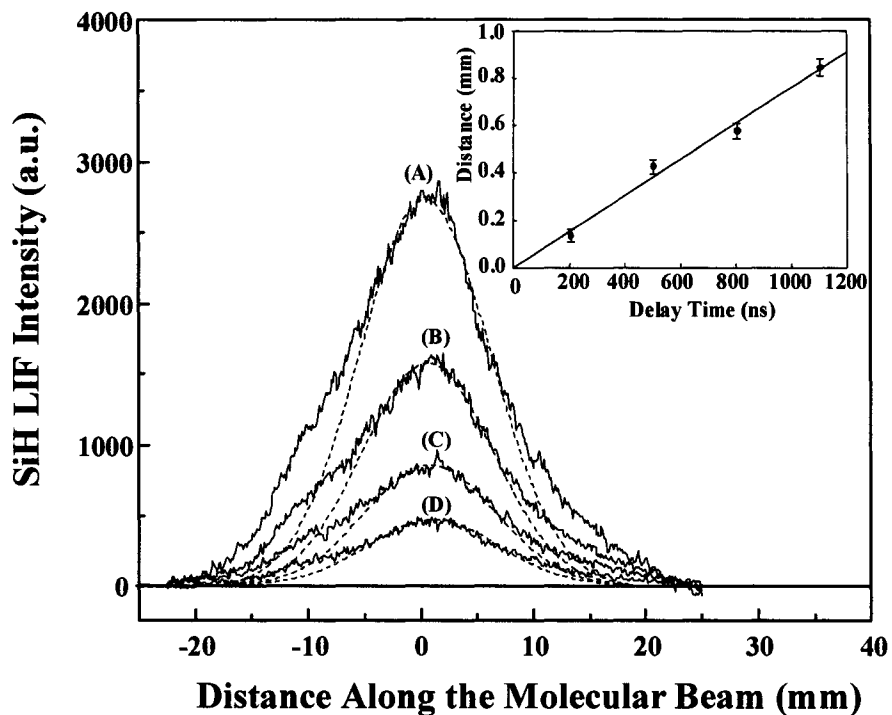


Figure 5.2a. Cross-sectional data for the SiH LIF images shown in Figure 5.1 (solid lines) at four different time delays: (A) 205 ns, (B) 505 ns, (C) 805 ns, and (D) 1105 ns after laser excitation. Simulated curves for $\Theta_T = 820$ K are also shown (dashed lines). In the inset, the spatial positions of the maxima of the LIF signals are plotted as a function of time delay. The slope of the linear regression analysis corresponds to the speed (759 m/s) of the SiH radicals along the central axis of the molecular beam.

distinguished when plotted as a function of time delay as in the inset of Figure 5.2a. The linear regression analysis yields a slope of 759 m/s, which represents a lower limit to the average SiH speed in the molecular beam. This value corresponds to $\Theta_T(\text{SiH}) = 789$ K. To obtain a more accurate average speed and the corresponding average translational temperature, the spatial shifts as a function of time delay have been simulated at different translational temperatures until a good agreement between the experimental and simulated results is obtained. The simulation results are also plotted in Figure 5.2a, yielding an average kinetic speed of 760 ± 62 m/s and corresponding average translational temperature of $\Theta_T = 820 \pm 129$ K. The discrepancies between the model and the experimental signal shapes in Figure 5.2a are the result of the radial movement of the molecular beam in all directions during the expansion through a slit, resulting in “wings” on the data. For the speed measurements, however, the peak positions are the critical dimension being simulated, and this is not significantly affected by the wider wings at lower delay times.

Figure 5.2b shows the cross sectional plots of SiH LIF images for a mixed Si₂H₆/Ar plasma with a 2:1 ratio (67% Si₂H₆). The cross sections and the corresponding linear regression analysis are very similar to those shown in Figure 5.2a. The slope of the linear regression fit is, however, somewhat lower than that for the 100% Si₂H₆ plasma, 607 m/s. The simulation yields a correspondingly lower Θ_T of 525 ± 96 K for the Ar diluted system.

We have previously collected extensive excitation data for SiH over a wide range of wavelengths (411-414.5 nm)^{1,19} and have measured the rotational temperature from these spectra. Here we again collected excitation spectra over a reasonably wide wavelength range, and found good agreement with these previous results. For the purposes of determining Θ_R in this work, we focused on two

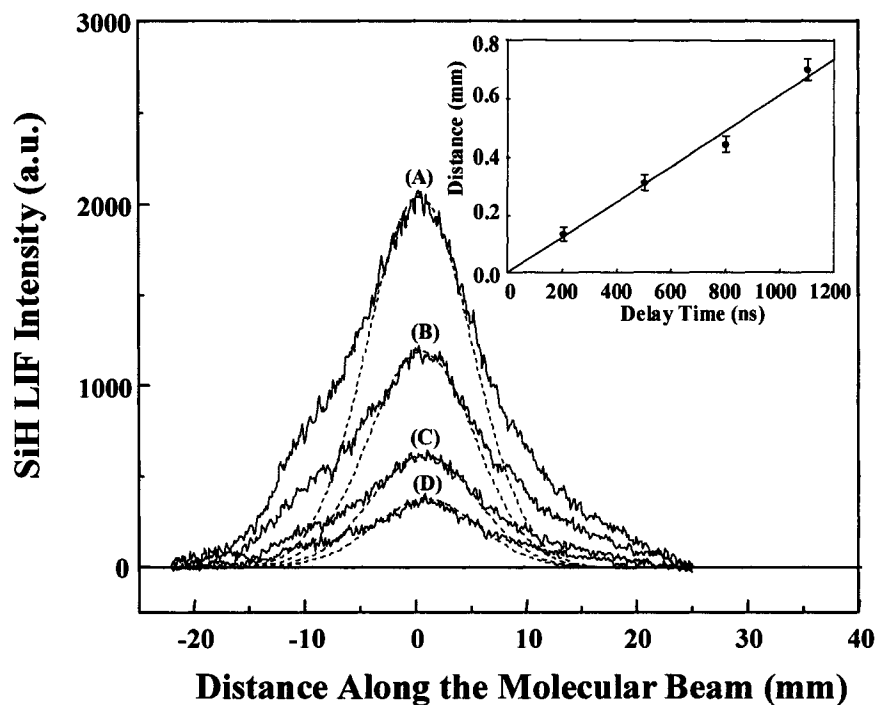


Figure 5.2b. Cross sectional data of SiH radicals in a 2:1 Si₂H₆/Ar plasma (67% Si₂H₆) at four different time delays: (A) 205 ns, (B) 505 ns, (C) 805 ns, and (D) 1105 ns after laser excitation. Simulated curves for $\Theta_T = 525$ K are also shown (dashed lines). In the inset, the spatial positions of the maxima of the LIF signals are plotted as a function of time delay. The slope of the linear regression analysis corresponds to the speed (607 m/s) of the SiH radicals along the central axis of the molecular beam.

rotational lines with significantly different quantum states. Figure 5.3 shows the experimental and simulated excitation spectra of SiH $A^2\Delta-X^2\Pi$ from 413.40 to 413.45 nm collected using a 100% Si₂H₆ plasma molecular beam (Figure 5.3a) and a 67% Si₂H₆ plasma molecular beam (Figure 5.3b). These data clearly show that the populations of the two states are similar for the two different plasma conditions, although it appears that the Q₁($J=10.5$) rotational state is slightly more populated in the diluted plasma system. As can be seen in Figure 5.3, excellent fits between the experimental and simulated data were obtained for both data sets. Because these two rotational lines have quite different J quantum numbers (10.5 and 2.5), the ratio of these two peaks heights will be sensitive to changes in the rotational temperatures. As noted above, we have previously fit larger portions of the rotational spectrum for SiH and find good correspondence between these fits and the fits to the two rotational states chosen for analysis in this study.^{1,19} From several data sets, the simulation yielded a rotational temperature of 520 ± 10 K for the 100% Si₂H₆ data set and 550 ± 30 K for the 67% Si₂H₆ data set. These values are consistent with the observation that the $J=10.5$ state is more highly populated in the diluted plasma system.

Figures 5.4 and 5.5 contain the average Θ_T and Θ_R values determined for SiH in SiH₄/Ar and Si₂H₆/Ar plasmas as a function of SiH₄ and Si₂H₆ fraction in the mixtures, respectively. As noted in the experimental section, the fraction of SiH₄ and Si₂H₆ in the mixture is defined as the ratio of the flow rate of SiH₄ or Si₂H₆ to the flow rate of Ar. For the rotational temperatures of SiH, no clear dependence on the argon dilution is found in either silane or disilane plasmas. The weighted average Θ_R values for SiH in SiH₄/Ar and Si₂H₆/Ar plasmas (averaging all dilution conditions) are 490 ± 10 K and 530 ± 10 K, respectively. In contrast, Θ_T for SiH demonstrates different trends in the two plasma systems. No significant dependence on Ar dilution

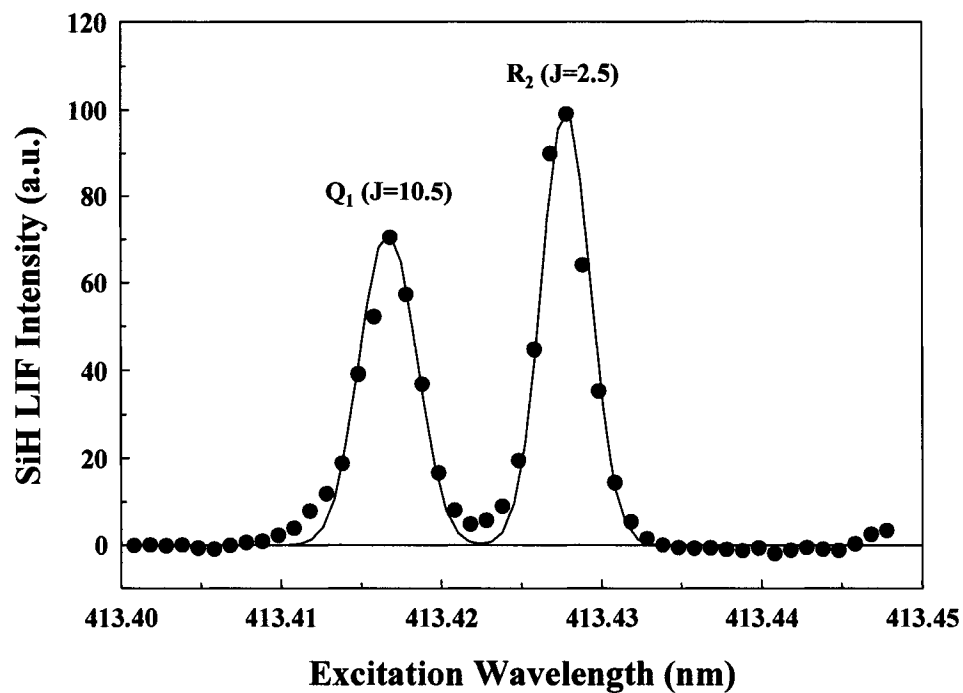


Figure 5.3a. The SiH $A^2\Delta-X^2\Pi$ excitation spectrum (solid circle) from 413.40 nm to 413.45 nm obtained in a 100% Si_2H_6 plasma. The simulated excitation spectrum using LIFBASE program is also shown (solid line). The best fit between the experimental and simulated data corresponds to rotational temperature of 520 K.

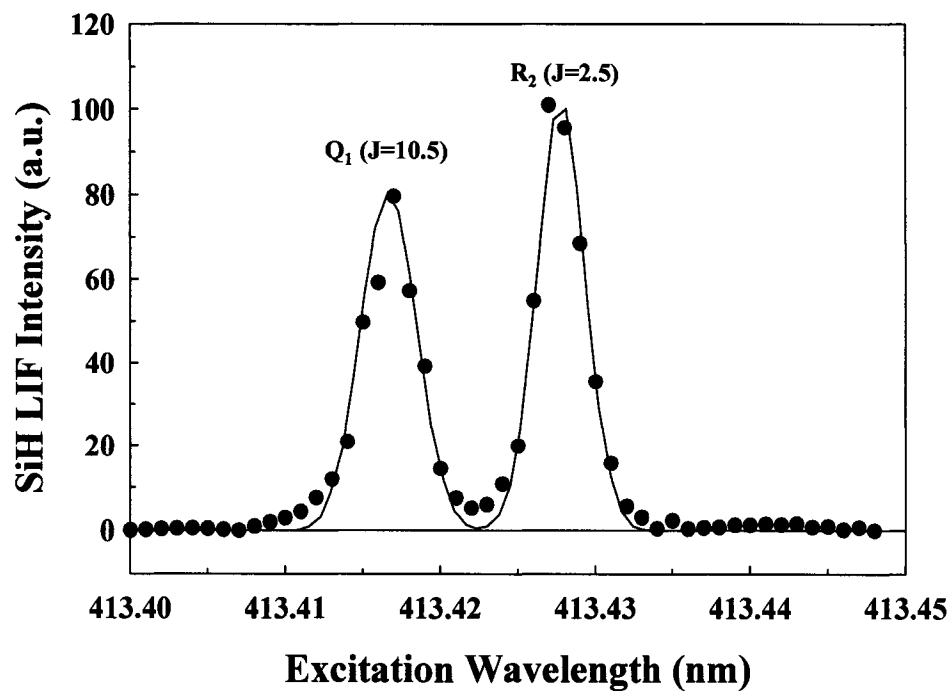


Figure 5.3b. The SiH $A^2\Delta-X^2\Pi$ excitation spectrum (solid circle) from 413.40 nm to 413.45 nm obtained in a 67% Si_2H_6 plasma. The simulated excitation spectrum using LIFBASE program is also shown (solid line). The best fit between the experimental and simulated data corresponds to rotational temperature of 550 K.

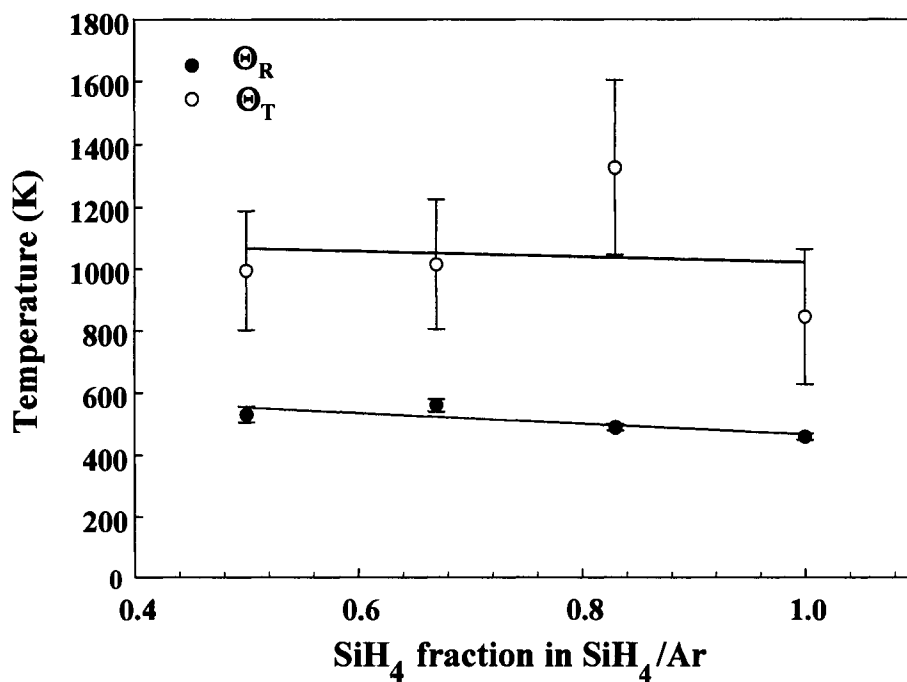


Figure 5.4. The average translational (open circles) and rotational (solid circles) temperatures of SiH radicals in SiH₄/Ar plasmas as a function of SiH₄ fraction in the feed gas. The lines are linear regression fits to the data.

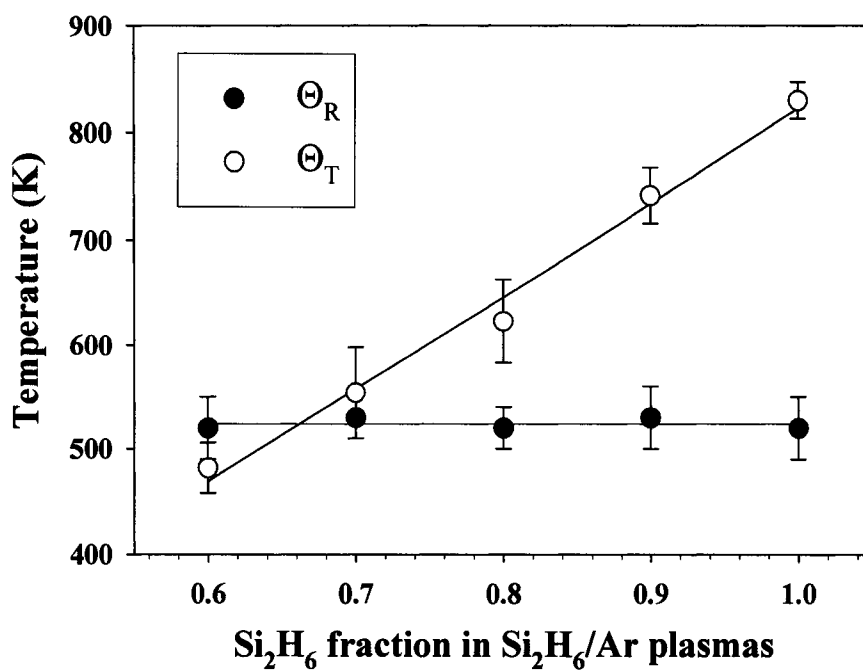


Figure 5.5. The average translational (open circles) and rotational (solid circles) temperatures of SiH radicals in Si₂H₆/Ar plasmas as a function of Si₂H₆ fraction in the feed gas. The lines are linear regression fits to the data.

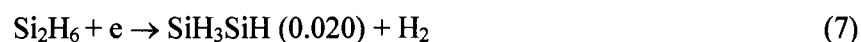
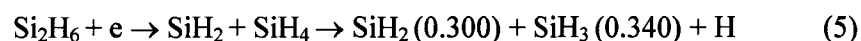
is seen in the SiH₄/Ar plasma within the investigated fraction range of SiH₄ from 0.5 to 1.0, as shown in Figure 5.4. At lower SiH₄ fractions, the SiH signal decreases to below the detectable limit in our apparatus. In the Si₂H₆/Ar plasma, however, the translational temperature of SiH increases significantly with increasing Si₂H₆ fraction. When the fraction of Si₂H₆ reaches 0.67, the translational temperature of SiH is almost equal to its rotational temperature, which indicates that SiH radicals reach thermal equilibrium in this plasma system.

5.3. Discussion

The energy distribution of radicals produced in a plasma system largely depends on their formation mechanisms. In silane and disilane plasmas, the primary radical fragments formed through direct electron impact reactions are quite different. The primary radicals produced in the SiH₄ plasma are given in Reactions 1-4,^{7,10,14,15,24-26} where the numbers in parentheses refer to the fraction of the radicals in the gas phase:



Note that the production mechanisms for SiH radicals have been extensively studied. From these works, it is commonly accepted that SiH radicals are formed primarily from the direct electron impact dissociation of SiH₄, Reaction 3.^{1,10,14,25} In contrast, for Si₂H₆ plasma, SiH is not formed from the direct electron impact dissociation of Si₂H₆.^{1,3,10} The primary Si₂H₆ dissociation reactions in Si₂H₆ plasmas are given in Reactions 5-7.^{3,10}



In a disilane plasma, SiH radicals are mainly produced by further dissociation of the primary product SiH₄, presumably via reaction (3), or possibly by a stepwise dissociation mechanism (i.e. SiH₄ → SiH₃ → SiH₂ → SiH).^{1,3,10}

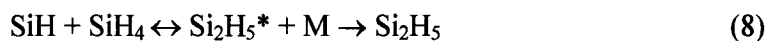
During the dissociation of precursor molecules via electron impact reactions, the released excess energy is transferred to the dissociated fragments. This can lead to a high initial translational and rotational energy for these fragments,^{1,8,14-16} which can be dissipated through collisional cooling. The rotational temperatures of SiH in both silane and disilane plasmas are nearly the same at all gas ratios, indicating that the rotational energy of SiH has been thermally equilibrated. This is supported by the observation that the rotational relaxation rate of SiH is fairly high ($1.5 \times 10^{-10} \text{ cm}^3/\text{s}$),²⁷ such that the rotational temperature of SiH is likely thermalized to the average gas temperature before it is extracted from the plasma source. It is a common assumption that the rotational temperature of the gas-phase radicals is equal to the average ambient gas temperature because the high initial rotational energy can be easily dissipated through rotational-rotational and rotational-translational energy transfer due to the high rotational relaxation rate.^{1,4,28} Thus, in our systems, we believe the gas temperature is ~500 K, in good agreement with what we found previously for SiH₄ and Si₂H₆ plasmas over a range of applied rf powers ($P = 20\text{-}80 \text{ W}$).¹

It is also commonly accepted that the average rotational temperature of the gas-phase species in plasmas is equal to their average translational temperature and thus to the ambient gas temperature. Our results for SiH do not, however, support this

assumption. Indeed, the Θ_T values measured for SiH in both SiH₄/Ar and Si₂H₆/Ar plasmas are significantly higher than the gas temperature (~1000 K vs ~500 K) under most dilution conditions. This indicates that the initially high translational energy has not been thermalized prior to extraction from the source. The observation that Θ_T is nearly the same as Θ_R at the highest Ar dilution for Si₂H₆ plasma is discussed further below.

One possibility for the significantly higher Θ_T values found in the SiH₄ systems and in most of the Si₂H₆ systems is that there has been some supersonic expansion in the molecular beam. For a typical supersonic expansion molecular beam, however, the internal energy of molecules is transferred to the kinetic energy during the expansion, leading to very low Θ_R values (e.g. <50 K). In our systems, $\Theta_R \sim 550$ K, significantly higher than typical supersonic beams. Moreover, if supersonic expansion was occurring, Θ_T would be high under all conditions and the addition of Ar would not affect these values (as the pressure is the same). For the most diluted Si₂H₆ plasmas, however, we measure a *lower* Θ_T for SiH, indicating that the dilution significantly affects the translational temperature, most likely through collisional cooling. One additional point can be made from previous results in our laboratory for a 100% H₂O plasma, wherein we measured the rotational and translational temperatures of OH radicals as nearly identical, with no dependence on applied rf power.²⁰ Finally, we have previously explicitly tested the effects of orifice size and find no dependence on this parameter for either the Θ_T or Θ_R for SiH radicals. Thus, we are confident that the effects we observe are not the result of supersonic expansion of our molecular beam.

Gas-phase production and loss reactions of radicals are important for understanding thermal equilibration processes in a plasma system. Like other highly reactive radicals such as Si and SiH₂, SiH easily reacts with SiH₄ via Reaction 8,



where M is a third body that collisionally stabilizes Si₂H₅*.²⁹ Nomura *et al.* measured the rate constant of this reaction as $4.8 \times 10^{-11} \text{ cm}^3 \text{ mol}^{-1} \text{ s}^{-1}$ in the afterglow of an SiH₄/Ar plasma at 300 K.²⁹ Reaction 8 has, therefore, been considered as the primary gas-phase loss mechanism of SiH in silane plasmas.⁹ As noted above, the primary creation mechanism for SiH is Reaction 3 in both silane and disilane plasmas. Thus, the balance between these two processes affects both the SiH density in the plasma as well as the thermalization of the translational and internal energies. For example, the increase of Ar in both systems results in a significant decrease (~factor of 2-3 at 30% Ar) in the number density of SiH as a result of fewer precursor molecules. Likewise, the translational temperature of SiH shows different trends as a function of argon dilution in SiH₄/Ar and Si₂H₆/Ar plasmas, as shown in Figures 5.4 and 5.5. In the Si₂H₆/Ar plasma, a clear dependence on the Ar fraction is found, whereas there is no dependence on Ar dilution in the SiH₄/Ar plasma. This difference in the translational temperatures indicates that SiH radicals in the silane and disilane plasmas have different thermal equilibration rates.

This can be understood by examining the source of the SiH being detected in the IRIS experiments. In the 100% silane and disilane plasmas, the loss rate of SiH radicals via reaction with SiH₄ is high due to the relatively high density of SiH₄. The detected SiH radicals in these systems must, therefore, be those extracted from the plasma reactor before their kinetic energy has been thermalized via non-reactive collisions with SiH₄. These SiH radicals have a relatively high translational energy of

~1000 K, which arises from the initial dissociation processes. It is assumed that the third body collisional stabilization in Process 8 comes primarily from precursor gas molecules in each system.

The gas-phase chemistry of the two systems is significantly affected by Ar dilution. Specifically, the dilution affects the density of SiH₄ in the SiH₄/Ar and Si₂H₆/Ar plasmas differently. In the disilane system, SiH radicals are produced via subsequent dissociation of SiH₄ that is formed via electron impact of Si₂H₆, Reaction 5. Because this is a secondary dissociation pathway, the SiH₄ density is relative low, especially at high fractions of argon. SiH radicals formed in the disilane system are thus more likely to be thermalized via non-reactive collisions before they are lost through reaction with SiH₄. In the silane plasmas, however, the relative SiH₄ density is significantly higher than that in a disilane plasma. Thus, the loss of SiH via reaction with SiH₄ is high, even at argon fractions of 0.5. Hence, the SiH radicals detected within the investigated dilution range are most likely nascent SiH radicals formed via Reaction 3, thereby maintaining a high translational energy, even with the addition of Ar.

Support for this hypothesis comes from literature studies of Si atoms and SiH₂ in SiH₄/Ar systems. In comparison, Si atoms have a much higher reactivity with SiH₄ than SiH,^{9,30} whereas SiH₂ has a comparable reactivity to SiH.²⁹ Tanaka *et al.* measured the translational temperature of Si in a 50 mtorr SiH₄/Ar plasma using laser absorption spectroscopy.³⁰ From their data, $\Theta_T(\text{Si})$ decreases significantly when the fraction of SiH₄ is lower than 0.5. In the 100% SiH₄ system, $\Theta_T(\text{Si}) \sim 680$ K, whereas at 20% SiH₄, $\Theta_T(\text{Si}) \sim 480$ K. At 5% SiH₄, the translational temperature of Si reaches room temperature, which indicates that the Si radicals have been completely thermalized. In contrast, Kono *et al.* measured the translational temperature of SiH₂

in SiH₄/Ar plasmas (40 mtorr, 4.5 W) and found that $\Theta_T(\text{SiH}_2)$ is close to room temperature, 336 ± 34 K, regardless of the SiH₄ mixing ratio. Because of the high reactivity of atomic Si with SiH₄ molecules, Si atoms are lost via the Si + SiH₄ reaction before their kinetic energy is thermalized by non-reactive collisions with SiH₄ and Ar. For SiH₂, the rate constant of the SiH₂ + SiH₄ reaction is fairly large, but it is still an order of magnitude smaller than that of the Si + SiH₄ reaction. Thus, it is likely that SiH₂ produced via dissociation of SiH₄ can experience several non-reactive collisions before it is lost via the SiH₂ + SiH₄ reaction, even in pure SiH₄ plasma. This can explain the low and nearly constant translational temperature of SiH₂.

Although the reactions of Si atoms and SiH₂ molecules in SiH₄/Ar systems are not identical to our SiH systems, the trends are the same. The translational energy dissipation and equilibration of a species is determined by the non-reactive collisional rate. Species with lower reactivity in higher inert gas-diluted systems will have more efficient collisional cooling, thereby increasing the rate of thermal equilibration of translational energy.

One additional note about the effects of Ar dilution on the gas-phase chemistry in the plasmas. The initial rotational, vibrational, and translational energy for species such as SiH originates from the dissociation process of the parent molecule, primarily via electron impact reactions. Thus, the initial energy obtained in these degrees of freedom is associated with the electron energy in the plasmas. Although we have not explicitly measured the electron energy in the silane systems, we have previously measured it in similar CH₄/Ar plasmas,³¹ and found there is little variation in the electron energy with Ar addition when the plasma is in an inductively-coupled regime. Hence, we assume there is little variation in electron energy in the present systems.

Nonetheless, even small variations could result in differences in the initial rotational, vibrational, and translational energy distribution, which may be altered as the result of thermalizing collisions in the plasma. We have explicitly demonstrated the effects of thermalizing collisions on Θ_T and Θ_R . We have not, however, addressed the effects of Ar addition on the amount of vibrational heating occurring in the system as there is not a sufficiently high population of vibrationally excited SiH for us to detect in our systems under the conditions used here.

5.4. Summary

We have studied the effects of argon dilution on the translational and rotational energy equilibration of SiH in both SiH₄/Ar and Si₂H₆/Ar plasmas using the IRIS technique. Within the investigated gas ratio range, the rotational temperature of SiH shows no dependence on the Ar dilution in both systems, which indicates that the SiH rotational energy has been thermalized. Ar dilution does, however, have different effects on the SiH translational temperatures in the two plasma systems, which is caused by different SiH₄ concentrations in the gas phase. The gas-phase SiH₄ concentrations in SiH₄/Ar plasmas are higher. Thus in this system, there is no clear dependence of Θ_T on the Ar dilution, which indicates that the loss of SiH through reaction with SiH₄ in the gas phase is significant. The detected SiH radicals are likely nascent radicals formed in the direct electron impact dissociation of SiH₄. In contrast, Θ_T (SiH) in Si₂H₆/Ar plasmas decreases significantly as the fraction of Ar increases, which suggests that SiH radicals in the argon diluted disilane plasma efficiently lose their kinetic energy through non-reactive collisions.

References

- (1) Kessels, W. M. M.; McCurdy, P. R.; Williams, K. L.; Barker, G. R.; Venturo, V. A.; Fisher, E. R. *J. Phys. Chem. B* **2002**, *106*, 2680.
- (2) Ho, P.; Breiland, W. G.; Buss, R. J. *J. Chem. Phys.* **1989**, *91*, 2627.
- (3) Longeway, P. A.; Weakliem, H. A.; Estes, R. D. *J. Phys. Chem.* **1984**, *88*, 3282.
- (4) Hertl, M.; Jolly, J. *J. Phys. D: Appl. Phys.* **2000**, *33*, 381.
- (5) Shirai, H.; Sakuma, Y.; Moriya, Y.; Fukai, C.; Ueyama, H. *Jpn. J. Appl. Phys. Part 1* **1999**, *38*, 6629.
- (6) McCurdy, P. R.; Truitt, J. M.; Fisher, E. R. *J. Vac. Sci. Technol. A* **1999**, *17*, 2475.
- (7) Kono, A.; Koike, N.; Nomura, H.; Goto, T. *Jpn. J. Appl. Phys. Part 1* **1995**, *34*, 307.
- (8) Kono, A.; Hirose, S.; Kinoshita, K.; Goto, T. *Jpn. J. Appl. Phys. Part 1* **1998**, *37*, 4588.
- (9) Kessels, W. M. M.; Hoefnagels, J. P. M.; Boogaarts, M. G. H.; Schram, D. C.; van de Sanden, M. C. M. *J. Appl. Phys.* **2001**, *89*, 2065.
- (10) Shirafuji, T.; Tachibana, K.; Matsui, Y. *Jpn. J. Appl. Phys. Part 1* **1995**, *34*, 4239.
- (11) Amorim, J.; Baravian, G.; Jolly, J. *J. Phys. D: Appl. Phys.* **2000**, *33*, R51.
- (12) Kono, A.; Hirose, S.; Goto, T. *Jpn. J. Appl. Phys. Part 1* **1999**, *38*, 4389.
- (13) Yamamoto, Y.; Suganuma, S.; Ito, M.; Hori, M.; Goto, T. *Jpn. J. Appl. Phys. Part 1* **1997**, *36*, 4664.

- (14) Matsumi, Y.; Hayashi, T.; Yoshikawa, H.; Komiya, S. *J. Vac. Sci. Technol. A* **1986**, *4*, 1786.
- (15) Stamou, S.; Mataras, D.; Rapakoulias, D. *J. Phys. D: Appl. Phys.* **1998**, *31*, 2513.
- (16) Zhang, J.; Williams, K. L.; Fisher, E. R. *J. Phys. Chem. A* **2003**, *107*, 593.
- (17) McCurdy, P. R.; Botoi, C. I.; Williams, K. L.; Fisher, E. R. *J. Phys. Chem. B* **1999**, *103*, 6919.
- (18) McCurdy, P. R.; Venturo, V. A.; Fisher, E. R. *Chem. Phys. Lett.* **1997**, *274*, 120.
- (19) McCurdy, P. R.; Bogart, K. H. A.; Dalleska, N. F.; Fisher, E. R. *Rev. Sci. Instrum.* **1997**, *68*, 1684.
- (20) Bogart, K. H. A.; Cushing, J. P.; Fisher, E. R. *J. Phys. Chem. B* **1997**, *101*, 10016.
- (21) Fisher, E. R.; Ho, P.; Breiland, W. G.; Buss, R. J. *J. Phys. Chem.* **1993**, *97*, 10287.
- (22) Zhang, J.; Fisher, E. R. *J. Phys. Chem. B* **2004**, *108*, 9821.
- (23) Buss, R. J.; Ho, P. *IEEE Trans. Plasma Sci.* **1996**, *24*, 79.
- (24) Nomura, H.; Kono, A.; Goto, T. *Jpn. J. Appl. Phys. Part 1* **1994**, *33*, 4165.
- (25) Gallagher, A.; Howling, A. A.; Hollenstein, C. *J. Appl. Phys.* **2002**, *91*, 5571.
- (26) Doyle, J. R.; Doughty, D. A.; Gallagher, A. *J. Appl. Phys.* **1992**, *71*, 4727.
- (27) Schmitt, J. P. M.; Gresier, P.; Krishnan, M.; de Rosny, G.; Perrin, J. *J. Chem. Phys.* **1984**, *84*, 281.
- (28) Perrin, J.; Delafosse, E. *J. Phys. D: Appl. Phys.* **1980**, *13*, 759.
- (29) Nomura, H.; Akimoto, K.; Kono, A.; Goto, T. *J. Phys. D: Appl. Phys.* **1995**, *28*, 1977.

- (30) Tanaka, T.; Hiramatsu, M.; Nawata, M.; Kono, A.; Goto, T. *J. Phys. D: Appl. Phys.* **1994**, *27*, 1660.
- (31) Zhou, J.; Martin, I. T.; Ayers, R.; Adams, E.; Liu, D.; Fisher, E. R. *Plasma Source Sci. Technol.* **2005**, manuscript in preparation.

CHAPTER 6

SURFACE REACTIVITY AND ENERGY ENERGETICS OF CH RADICALS DURING PLASMA DEPOSITION OF HYDROGENATED DIAMOND-LIKE CARBON FILMS

This dissertation chapter contains results from a full paper submitted for publication to *Journal of Physical Chemistry B*. The manuscript was written by Jie Zhou and edited by Ellen R. Fisher. This chapter describes the effects of applied rf power, argon fraction, substrate temperature, and substrate bias on the surface reactivity of CH radicals for CH₄/Ar plasmas. The mechanisms of surface reactions of CH radicals with surface were discussed. In addition, the translational and rotational temperatures of CH radicals in CH₄/Ar plasmas were also measured.

6.1. Introduction

Hydrogenated diamond-like carbon (DLC) films can be used in a wide range of applications because of their high hardness, extremely low surface roughness, scratch resistance, chemical inertness, good thermal conductivity, high electrical resistance, and optical transparency.¹ There are several low-pressure DLC deposition methods, including microwave plasmas,^{2,3} electron-cyclotron resonance (ECR) plasmas,^{4,5} dc-arcjet discharges,^{6,7} and inductively coupled plasmas (ICPs).^{8,9} The materials properties of films deposited by these techniques are usually dependent on the plasma parameters, which implies that different plasma species play a key role in film growth. Numerous studies have, therefore, been performed on plasma systems and on gas-phase densities of the different species in methane-based plasmas.¹⁰⁻¹³ During the deposition processes, neutral hydrocarbon species are considered as important precursors for film growth and have been widely studied.¹⁴ For example, Luque *et al.* studied CH radicals in the $CH A^2\Delta \leftarrow X^2\Pi$ transition of a dc-arcjet discharge by laser induced fluorescence (LIF).¹⁵ Menningen and co-workers used absorption spectroscopy to measure CH_3 radical concentrations in hot filament and dc-discharge reactors.¹⁶ The absolute concentration of C_2 has also been measured by Kaminski *et al.* in a diamond chemical vapor deposition (CVD) reactor using LIF.¹⁷ Among these neutral species, CH_3 and CH_2 are thought to be the dominant contributors to DLC film growth, whereas the contribution of CH radicals to film formation is small due to its low flux in methane plasmas.^{14,18} However, the quality of the film can be greatly affected by CH radicals.¹⁴ Therefore, data on the surface reactivity of CH radicals is very important to understand the mechanisms of film growth.

The roles of gas-phase radicals and gas-surface interactions during film growth processes are important to understand the overall methane plasma chemistry. For example, Kuedell and coworkers have investigated the simultaneous interaction of CH₃ and H radicals with a-C:H films using optical in-situ diagnostics.^{13,19} They found that the sticking coefficient of CH₃ radicals is related to the surface radical site or “dangling bond” density. These sites are created by H radicals through abstraction of surface hydrogen atoms. Impinging CH₃ radicals then adsorb at these active sites, leading to the growth of a-C:H films. In contrast to CH₃, CH radicals have high reactivity (some reactions exhibit no activation barrier and, hence, occur even at low temperature) in the gas phase.^{6,20} Furthermore, examination of the relevant literature indicates that gas-phase CH is lost primarily through neutral chemistry with the parent methane molecules.⁶ To date, however, there is little information about the relationship between the CH radicals and the quality of the deposited DLC films. Therefore, the measurements of CH reactivity with surfaces by our imaging of radicals interacting with surfaces (IRIS) in the present work will enable a better understanding of the mechanisms of DLC film growth in methane plasmas.

The IRIS technique used in our laboratories provides a unique way to measure radical-surface interactions during plasma processing of a substrate.²¹⁻²⁴ It combines plasma molecular beam techniques with spatially resolved LIF to study the state-specific reactivity and the translational and rotational temperatures of plasma-generated species during a plasma-processing event. With this method, the surface reactivity of radicals during plasma processing is directly measured by two-dimensional imaging using LIF. Moreover, the dependence of the surface reactivity on plasma parameters, substrate material, substrate temperature (T_s), and ion energy

can also be obtained with IRIS, primarily because the use of a molecular beam facilitates independent variations of the plasma and surface conditions.

In addition, knowledge of energy participation between different species is another important aspect to understand the overall chemistry occurring in low-temperature plasmas. However, kinetic energy distributions of plasma species are difficult to determine.²⁵ IRIS not only allows us to obtain surface reactivity of radicals interacting with surfaces but can also be used to measure speed distributions of radicals in the plasma molecular beam²⁶⁻²⁸ and of those scattered off of surfaces.^{29,30} The average translational speed of radicals is determined by taking LIF images at different time delays after the laser excitation of the radicals and evaluating the spatial shift of the LIF images. This speed can then be converted to a translational temperature. We have measured both translational temperature, Θ_T , and rotational temperature, Θ_R , for SiH in SiH₄/Ar and Si₂H₆/Ar plasmas. The results showed that Θ_R was ~550 K and independent of applied rf power and gas composition, whereas Θ_T (~1000 K) was significantly higher than Θ_R in SiH₄/Ar plasmas and independent of argon fraction under the investigated range (< 40%).³¹ Interestingly, Θ_T in Si₂H₆/Ar plasmas was found to be close to Θ_R at high argon fraction, suggesting that the initial high translational energy of SiH was thermalized via non-reactive collisions in the disilane systems. This was attributed to the lower probability of reactions between SiH and SiH₄ in the Si₂H₆ plasma.³¹ Such studies have, therefore, allowed us to discern different mechanisms for energy partitioning and have provided valuable information on the relationship between the kinetic and rotational temperatures of radicals in processing plasmas. In this study, the translational and rotational temperatures of CH as a function of applied rf power and Ar fraction will be measured. The energy partitioning in these plasmas will be discussed.

6.2. Results

6.2.1. Spectroscopy. LIF is a nonintrusive and highly selective technique that allows for the identification and study of one type of species among many others in the plasma molecular beam. Figure 6.1a shows the CH excitation spectrum obtained in a 50 mTorr, 100% CH₄ plasma, which represents the CH A²Δ ← X²Π (0, 0) transition. The entire excitation spectrum was collected by three individual scans at different ranges with a step size of 0.002 nm. Figure 6.1b shows the excitation spectrum of two closely spaced rotational lines, R₂ (*J* = 1) and Q₁ (*J* = 14.5), with significantly different quantum numbers. A comparison of the relative line intensities between the experimental spectrum with the spectra simulated at different rotational temperatures, using LIFBASE program,³² yields Θ_R = 1460 ± 20 K for CH in the 50 mTorr, 100% CH₄ plasma at *P* = 100 W.

Figure 6.2a shows the CH LIF intensity as a function of *P* for 50 mTorr, 100% CH₄ plasmas. All CH LIF intensities were collected at the on-resonance wavelength, 430.402 nm [R₁(*J* = 1)]. The background LIF intensity obtained at the off-resonance wavelength (430.2 nm) was subtracted from the on-resonance LIF intensity to remove interference from plasma emission. As seen in Figure 6.2a, the CH LIF intensity increases almost linearly when *P* < 100 W. At *P* > 100 W, the CH LIF intensity reaches a saturation region. Increasing *P* to 160 and 180 W results in a small decrease in CH signal intensity. This variation trend contrasts with previous results obtained in fluorocarbon plasmas, in which the CF₂ LIF intensity increases continuously with increasing rf power.³³ It is, however, similar to results obtained for NH in NH₃ plasmas.³⁴

6.2.2. Radical-surface interaction. Surface reactivity in IRIS experiments is measured by comparison of ICCD images obtained with the substrate in and out of the

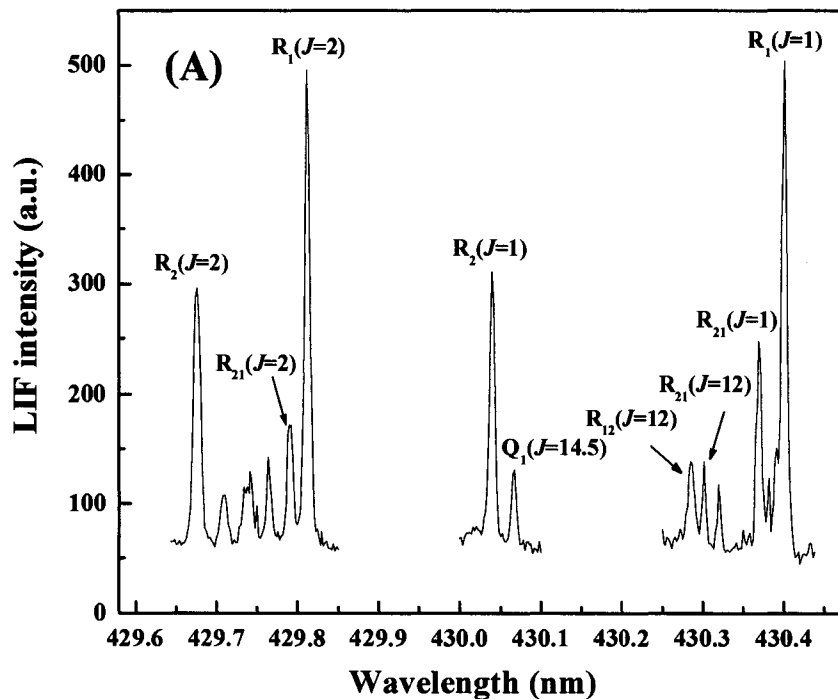


Figure 6.1a. The CH $A^2\Delta \leftarrow X^2\Pi$ excitation spectrum from 429.65 to 430.45 nm using a 100% CH_4 plasma at 50 mTorr, $P = 100$ W. The entire excitation spectrum was collected by three individual scans at different ranges. The $R_1(J=1)$ line was used for IRIS reactivity and speed measurements. The Lambda doubling of the rotational lines is not resolved because of optical saturation of the transition.

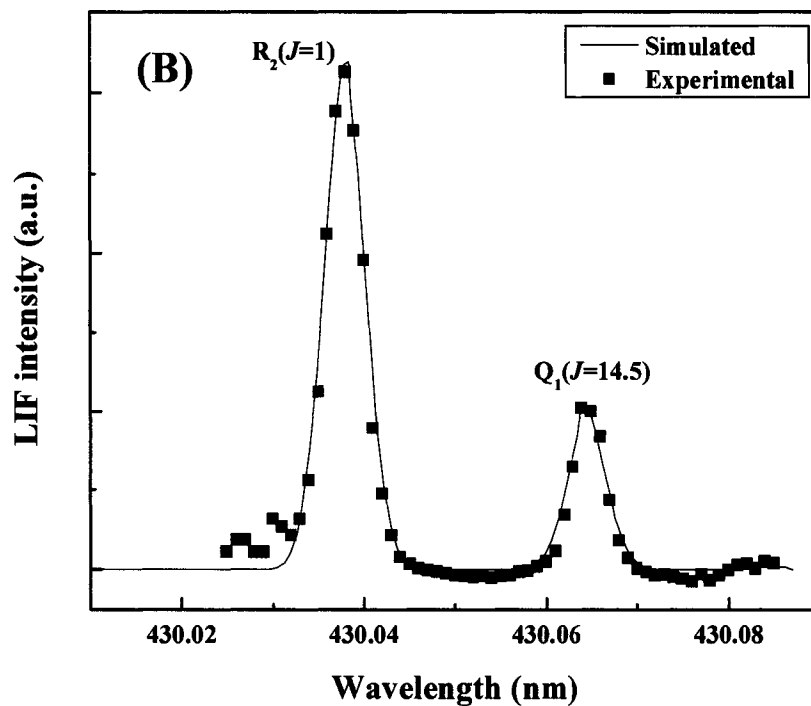


Figure 6.1b. The CH $A^2\Delta \leftarrow X^2\Pi$ excitation spectrum (\blacksquare) from 430.02 to 430.09 nm used for determining the Θ_R together with the simulated spectrum (—) for a 100% CH_4 plasma at 50 mTorr, $P = 100$ W. The Lambda doubling of the rotational lines is not resolved because of optical saturation of the transition.

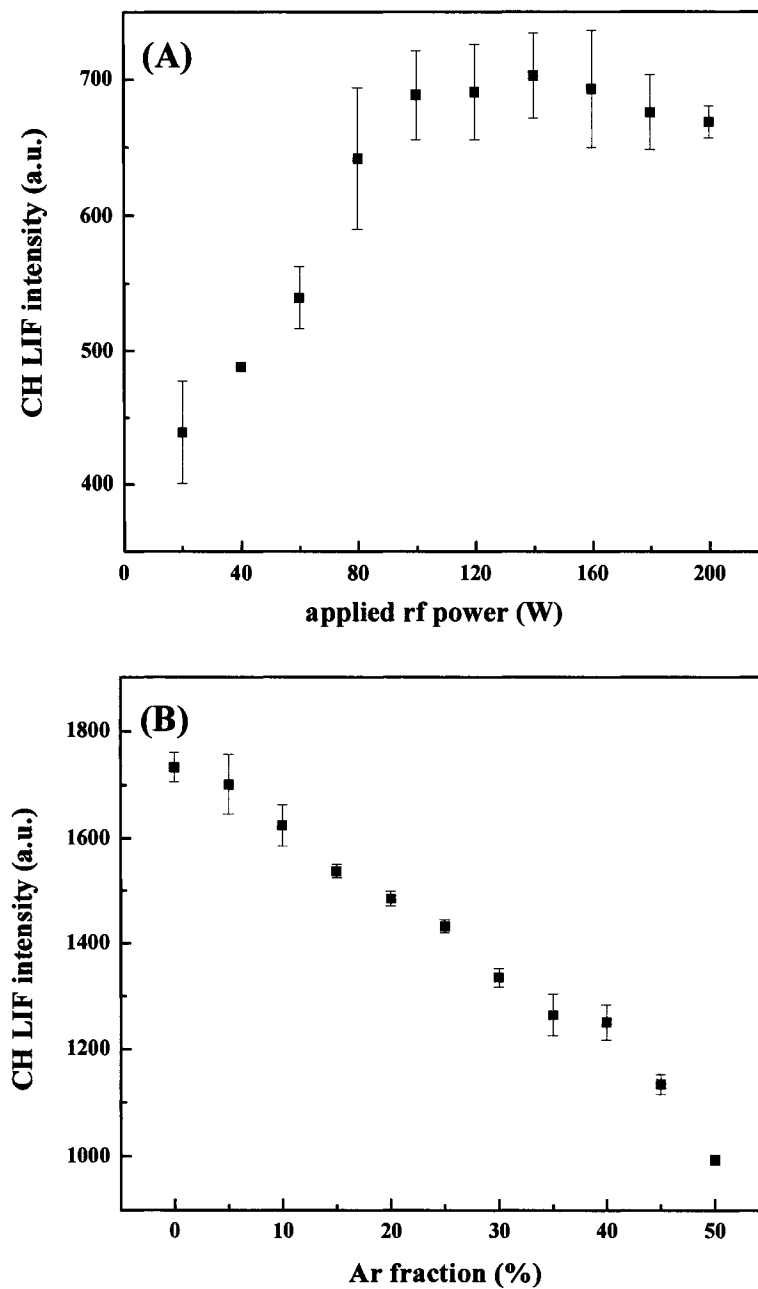


Figure 6.2. CH LIF intensity for (A) a 100% CH₄ plasma at 50 mTorr as a function of applied rf power and (B) a CH₄/Ar plasma at 50 mTorr as a function of Ar fraction.

path of the plasma molecular beam. Figure 6.3 shows a typical set of 2-dimensional ICCD images of LIF signals for CH in a 50 mTorr, 100% CH₄ plasma at $P = 140$ W. The CH signals in the incident molecular beam are shown in Figure 6.3a. In Figure 6.3b, the substrate is rotated into the path of the molecular beam and the LIF signal includes both CH in the incident molecular beam and any CH scattered from the substrate surface. Figure 6.3c is the difference between panels B and A in Figure 6.3, showing only the CH signal from the surface. By averaging several columns of pixels along the laser beam axis, 1-dimensional cross sections of the LIF images shown in Figure 6.3a and 6.3c can be obtained and are plotted in Figure 6.4. The simulation results, shown as dashed curves in Figure 6.4, yielded a scattering coefficient, $S = 0.01 \pm 0.04$, which results in a surface reactivity of $R = 0.99 \pm 0.04$ at the surface of a depositing a-C:H film.

The effects of applied rf power, substrate temperature, substrate bias, and Ar fraction on the surface reactivity of CH have been measured and the resulting R values are listed in Table 6.1. As can be seen clearly from the Table 6.1 data, the surface reactivity of CH is nearly unity and independent of these parameters. This high surface reactivity of CH implies that almost all incident CH radicals have been lost at the surface, either via a simple adsorption, sticking reaction, an abstraction of a surface atom reaction, or recombination with another radical at the surface.

6.2.3. Translational and rotational temperatures. A representative speed measurement is shown in Figures 6.5 and 6.6 for CH in a CH₄/Ar plasma with an Ar fraction of 10% and $P = 100$ W, using four different time delays and a 90° geometry between the laser and molecular beam. Figure 6.5 shows the ICCD images, and Figure 6.6 shows the corresponding X-cross-sectional LIF signals. As the time delay increases, the intensity of the LIF signal decreases and the cross section LIF signal

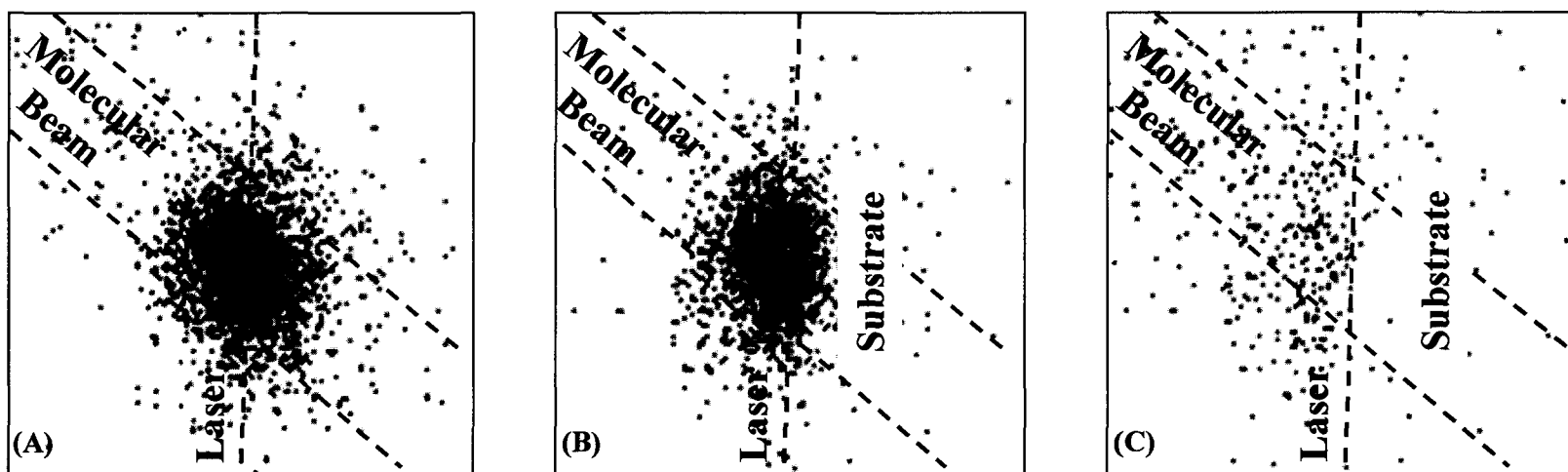


Figure 6.3. Two-dimensional ICCD images of CH LIF signals in (A) a 140 W, 100% CH₄ plasma molecular beam and (B) with a Si substrate rotated into the path of the molecular beam at a laser-surface distance of 3 mm. Image C is the difference between images B and A and shows only CH radicals scattered from the surface. Dashed lines indicate the locations of the molecular beam and the laser beam.

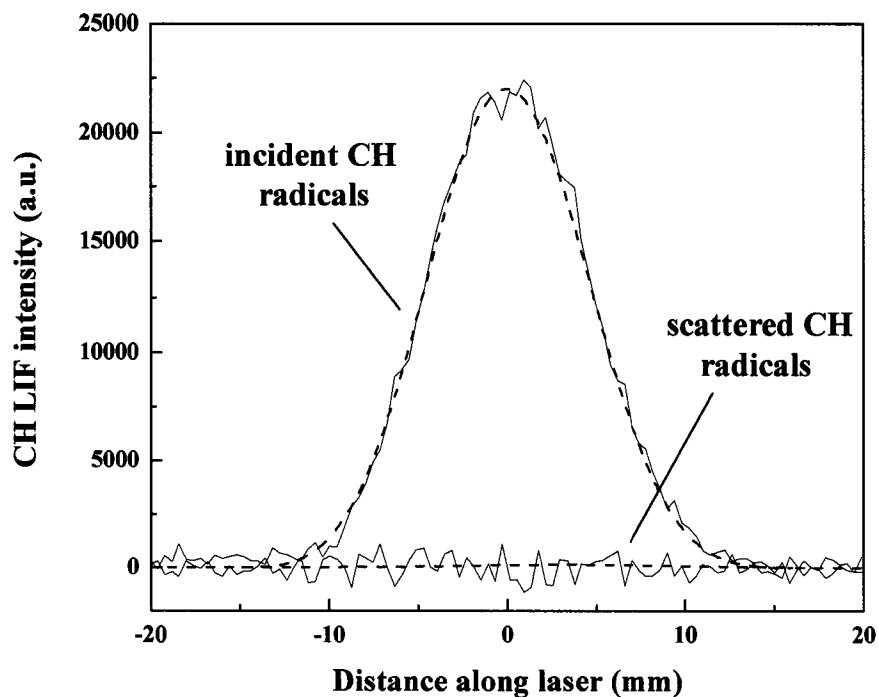


Figure 6.4. Cross-sectional data of the CH IRIS images presented in Figure 6.3. LIF signals are shown for radicals in the molecular beam incident on the substrate and for radicals scattering from the substrate (corresponding to parts A and C of Figure 6.3, respectively). Dashed lines are simulated curves as obtained by the reactivity simulation program described in the text, yielding $S = 0.01 \pm 0.04$. This corresponds to a surface reactivity for CH of $R = 0.99 \pm 0.04$.

Table 6.1. Surface reactivity of CH measured with IRIS.

Source gases	Argon fraction (%)	rf power (W)	T _s (K)	Substrate bias (V)	R
CH ₄	0	80	298	0	0.99 ± 0.05
	0	100	298	0	0.98 ± 0.03
	0	120	298	0	1.00 ± 0.04
	0	140	298	0	0.99 ± 0.04
	0	160	298	0	0.98 ± 0.06
	0	100	311	0	0.97 ± 0.05
	0	100	363	0	1.00 ± 0.06
	0	100	433	0	0.99 ± 0.05
	0	100	503	0	0.97 ± 0.03
	0	100	573	0	1.00 ± 0.06
	0	100	298	400	0.98 ± 0.04
	0	100	298	200	0.99 ± 0.05
	0	100	298	-200	0.99 ± 0.05
	0	100	298	-400	0.98 ± 0.06
CH ₄ /Ar	5	100	298	0	1.00 ± 0.05
	10	100	298	0	0.99 ± 0.04
	15	100	298	0	0.96 ± 0.07
	20	100	298	0	0.99 ± 0.05

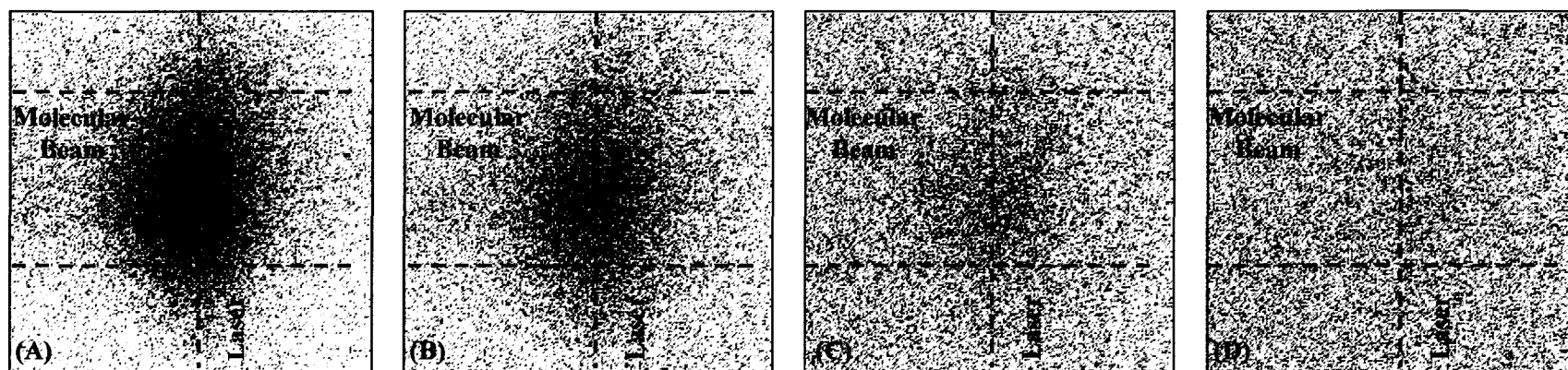


Figure 6.5. ICCD images of LIF signals for CH radicals in a 50 mTorr, CH₄/Ar (Ar fraction = 10% and $P = 100$ W) plasma molecular beam at four different gate delays: (A) 205 ns, (B) 705 ns, (C) 1205 ns, and (D) 1705 ns. Dashed lines indicate the locations of the molecular beam and the laser beam, which intersect at a 90° angle.

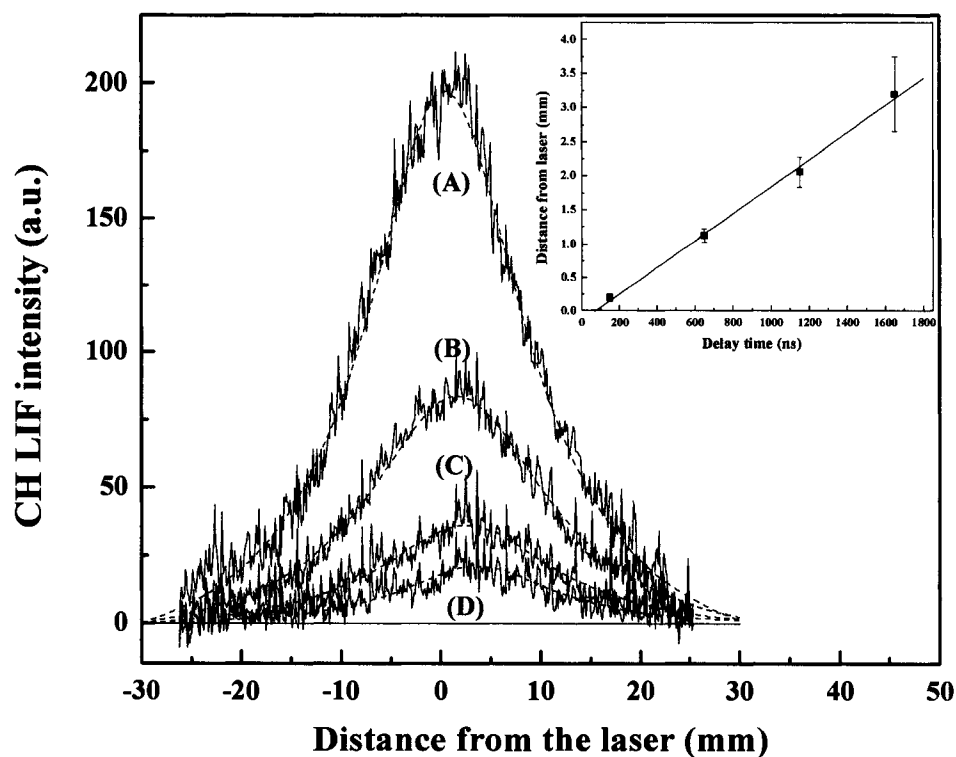


Figure 6.6. Cross-sectional data for the CH LIF images shown in Figure 6.5 (solid lines) at four different time delays: (A) 205 ns, (B) 705 ns, (C) 1205 ns, and (D) 1705 ns after laser excitation. Simulated curves for a CH translational temperature of 2518 ± 119 K are also shown (dashed lines). In the inset, the spatial positions of the maxima of the LIF signals are plotted as a function of time delay. The slope (1958 ± 44 m/s) of the linear regression corresponds to the speed of the CH radicals in the direction of the central axis of the molecular beam, which is a lower limit to the CH speed in the molecular beam.

shifts along the direction of the molecular beam. The shift is more clearly seen in the inset of Figure 6.6, which shows the peak position of LIF intensity as a function of time delay. The LIF intensity decreases with increasing time delay as a result of the radiation decay of the excited CH $A^2\Delta$ state after the laser excitation pulse. As mentioned above, larger steps in the time delay are preferred for more accurate measurement, but this is limited by the relatively low signal-to-noise ratio at longer time delays. The time delay steps (500 ns) used in the speed measurements are nearly as long as the radiative lifetime of CH (538 ns). The simulation results are also plotted in Figure 6.6. The good agreement between the experimental and simulated cross sections indicates the CH radicals in the effusive molecular beam follow a Maxwell-Boltzmann distribution. The simulation yields an average speed, v , of 1958 ± 44 m/s, corresponding to $\Theta_T = 2518 \pm 119$ K under these plasma conditions.

Figure 6.7 shows the average kinetic speed of CH as a function of applied rf power and Ar fraction. For the measurement of power dependence, a 100% CH₄ plasma was used as the molecular beam source and the pressure was kept at 50 mTorr. As seen in Figure 6.7a, very high average kinetic velocities of CH were found at low rf powers (20 and 60 W). Above 100 W, no significant change in the average kinetic velocities can be seen at higher P . Interestingly, this rapid decrease in speed at low P is concomitant with a transition of the CH₄-containing plasmas from a low-density regime to a high-density regime. Our previous work showed that there are two significant regimes in our inductively coupled plasma reactor: (1) a capacitive E mode with low plasma density, high electron temperature, and (2) an inductive coupling H mode with high plasma density, low electron temperature.³⁵ Figure 6.7b shows the effects of Ar addition on the speed of CH radicals at different pressures, 50 and 110 mTorr. For these measurements, $P = 100$ W. No significant dependence of Ar

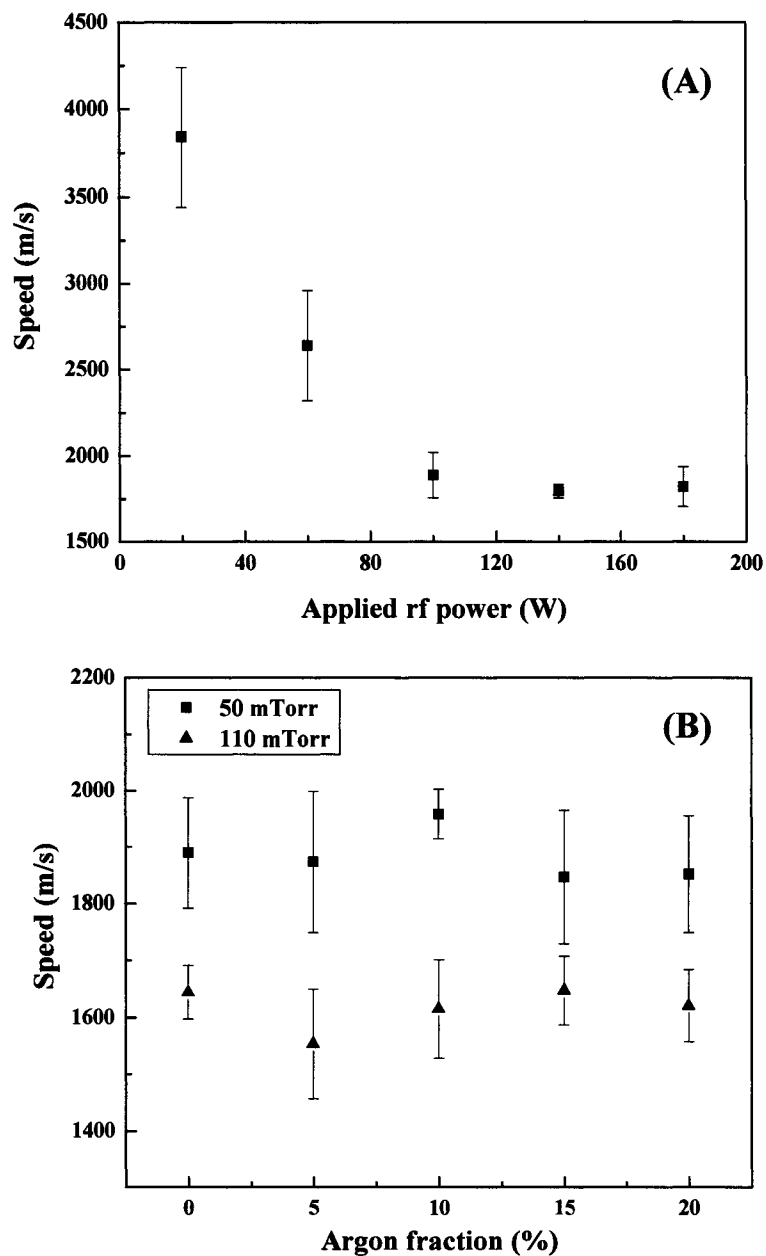


Figure 6.7. Speed of CH in the molecular beams of (A) 50 mTorr, 100% CH₄ plasmas as a function of applied rf power and (B) 50 mTorr and 110 mTorr CH₄/Ar plasmas ($P = 100$ W) as a function of argon fraction.

fraction on the average kinetic speed of CH can be found under the investigated Ar fraction range at both pressures. However, the average kinetic speed of CH radicals is significantly lower at the higher pressure. This might indicate higher electron temperatures at higher pressure.

The average CH kinetic translational temperatures are shown as a function of P and Ar fraction in Figure 6.8. At very low rf powers, 20 W and 60 W, Θ_T values are 9050 ± 2357 K and 4273 ± 1293 K, respectively. The large errors are most likely the result of plasma instabilities associated with the difficulty in sustaining the plasma at these low powers. At $P \geq 100$ W, no significant dependence of Θ_T (~ 2050 - 2300 K) values on P was measured. Θ_T values at different Ar fractions and pressures are shown in Figure 6.8b. No clear dependence of translational temperature on the Ar fraction can be observed. However, Θ_T is significantly lower at the higher source pressure of 110 mTorr.

Figure 6.8 also shows Θ_R as a function of P and Ar fraction. As discussed above, Θ_R is determined from two closely spaced rotational lines with considerably different quantum numbers (Figure 6.1b). As can be seen clearly, Θ_R is almost independent of P , Ar fraction, and pressure, which indicates that the rotational energy of CH radicals have been thermalized. Filippov *et al.* have calculated that the rotation relaxation coefficient of CH is $\approx 1.6 \times 10^{-10} \text{ cm}^3/\text{s}$.³⁶ Comparing this relaxation rate with the chemical reaction rate of $1 \times 10^{-10} \text{ cm}^3/\text{s}$ for the reaction of CH with CH_4 , CH can be easily rotationally equilibrated via several non-reactive collisions before reacting with the CH_4 molecules.^{12,37} Brown *et al.* indicated that rotational equilibrium can be achieved for diatomic molecules in four to six collisions.⁶

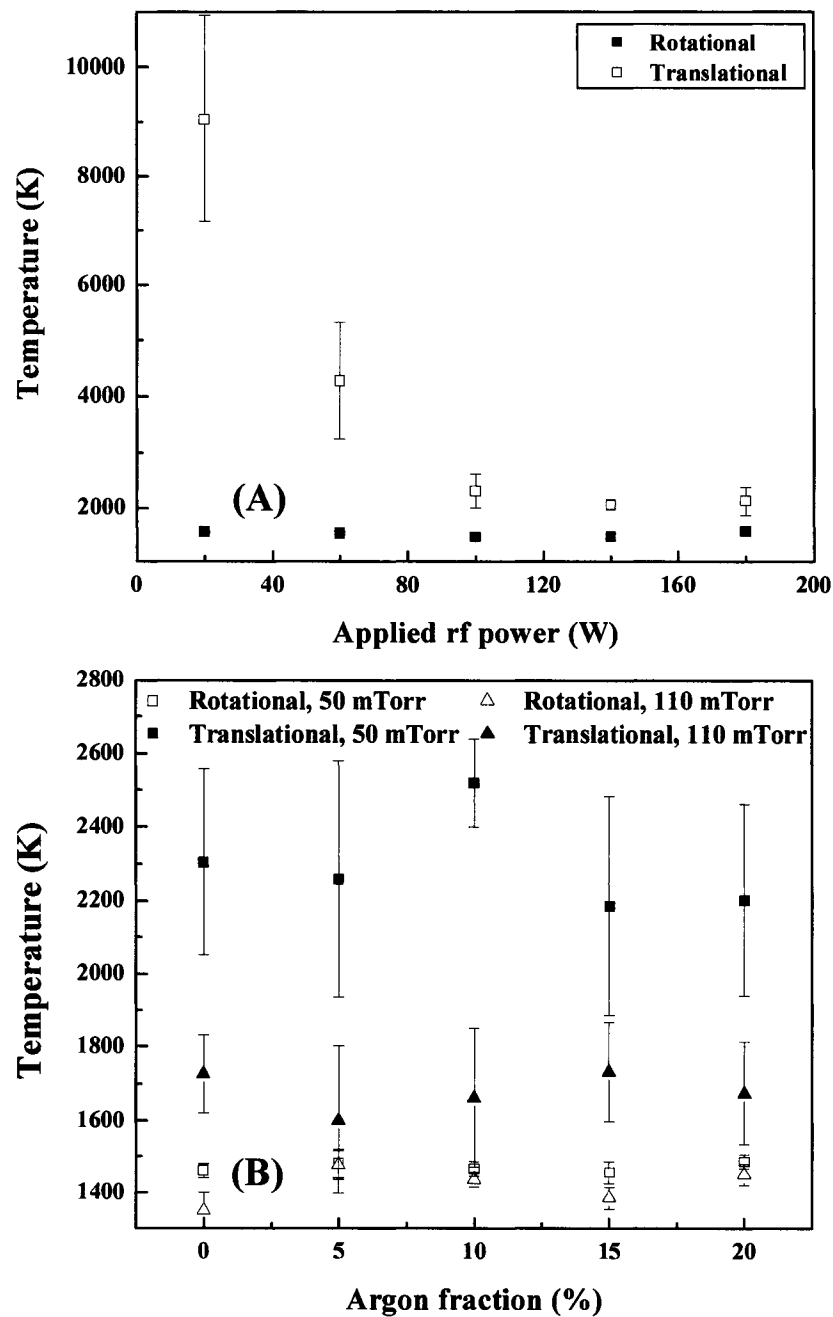


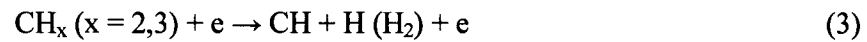
Figure 6.8. Average kinetic temperature, Θ_T , and rotational temperature, Θ_R , of CH in (A) 50 mTorr, 100% CH₄ plasmas as a function of applied rf power, and (B) CH₄/Ar plasmas ($P = 100$ W) at 50 mTorr and 110 mTorr as a function of argon fraction. The Θ_T values correspond to the speeds shown in Figure 6.7.

6.3. Discussion

To explain the power dissipation and the observed CH LIF intensity variation with applied rf power in CH₄ plasmas, the creation and loss mechanisms of CH in the CH₄ plasmas need to be addressed. In CH₄ plasmas, CH is created primarily by direct electron-impact dissociation reactions of CH₄, reactions 1 and 2 (the threshold energies for these two reactions are 9.19 eV and 13.71 eV, respectively),^{6,10}



rather than through a sequential dissociation of CH₃ or CH₂, as shown in reaction 3,



There are two loss channels for CH radicals, gas-phase reactions and surface loss reactions. For the gas-phase loss channel under the present discharge conditions, two reactions are important:



Reactions 4 and 5 have no activation barrier, hence, they occur even in a cool-discharge environment with high reaction rates, 3×10^{-10} and 1×10^{-10} cm³/s, respectively.⁶ Furthermore, considering the low density of H relative to that of CH₄ in CH₄ plasmas, reaction 5 should be the primary loss channel for CH radicals in the gas phase. As shown in the results section above, CH radicals demonstrated very high surface reactivity, suggesting that the primary surface loss mechanism is reaction 6:



Assuming that creation and loss of CH radicals are in an equilibrium, a balance equation for CH radicals can be written as (ignoring reaction 2 and 4):

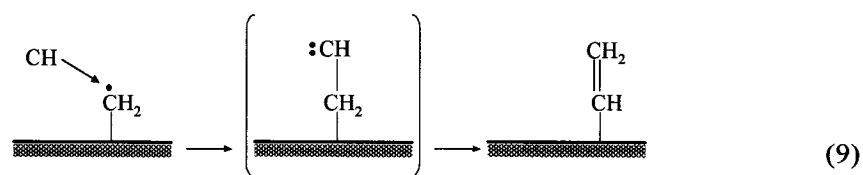
$$k_c[\text{CH}_4]n_e = k_{lg}[\text{CH}][\text{CH}_4] + k_{ls}[\text{CH}]A_s \quad (7)$$

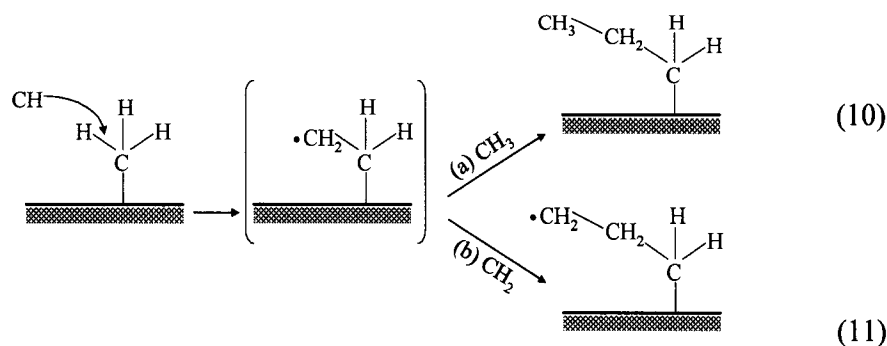
where k_c , k_{lg} , and k_{ls} are the rate constants for the CH creation reaction 1, the CH gas-phase loss reaction 5 and the CH surface loss reaction 6, respectively; n_e is the electron density in the CH₄ plasma; A_s is the surface area of the plasma reactor. Note that n_e is proportional to P in our present conditions ($n_e = kP$, where P is applied rf power), which has been confirmed by Langmuir probe results in our previous work.³⁵ Equation 7 also can be rewritten as equation 8:

$$[CH] = \frac{k_c [CH_4] n_e}{k_{lg} [CH_4] + k_{ls} A_s} \quad (8)$$

Here, $[CH_4]$ is also a function of P and decreases with increasing P because the methane plasmas are highly depositing systems. As P is increased, the degree of CH₄ dissociation will increase due to the increase in electron density, yielding a higher deposition rate. Consequently, CH₄ density decreases during the residence period in the plasma reactor as a result of the deposition loss of hydrocarbon radicals or ions, which are produced via the dissociation reactions of CH₄ molecules by electron impact. The accurate description of $[CH_4]$ as a function of P will not be discussed here due to the complexity. At low rf power ($k_{lg}[CH_4] \gg k_{ls}A_s$ because of the low dissociation rate of CH₄ and high $[CH_4]$), Equation 8 can be expressed as $[CH] = kP$, which corresponds the linear region in Figure 6.2a. For $100 < P < 180$ W, $[CH]$ is maximized because the increase of $[CH]$ as a result of an increase of n_e has been counteracted by the decrease of $[CH_4]$ because of film deposition. At $P > 180$ W, the increase in CH density from higher n_e can not compensate for the loss of $[CH_4]$ through film deposition. Therefore, a small decrease of $[CH]$ can be seen at this region, although it is still within experimental error. The CH LIF intensity decreases monotonically as a function of Ar fraction for 50 mTorr CH₄/Ar plasmas at $P = 100$ W, Figure 6.2b, as expected from the decrease in CH₄ concentration in the mixture.

The surface reactivity of CH is nearly unity and independent of all experimental variables studied, suggesting CH production via ion bombardment of a C:H film or via surface reactions of other species are clearly negligible. The mechanism for surface loss of CH radicals is, therefore, of significant interest. The growth mechanisms of hydrogenated carbon films can help elucidate this. It is well known that in methane containing plasmas, CH₃ and CH₂ radicals have higher gas-phase density; they are, therefore, considered the main contributors to film growth.³⁸ Morrison and coworkers have reported that 48.5% and 42.2% of total dissociation reactions of CH₄ contribute to the creation of CH₃ and CH₂, respectively, whereas only 4.4% contribute to the creation of CH.¹⁰ Tachibana *et al.* also reported that the calculated deposition rate contributed by CH radicals is smaller than the observed deposition rate by two orders of magnitude.¹⁴ Thus, film growth is primarily controlled by the following processes: (1) the abstraction of H from the C-H bonds on the surface by H radicals, thereby creating active sites on the surface; (2) CH₃ and CH₂ radicals adsorb at these active sites, resulting in film growth. Here, we propose the following mechanisms for the surface-interactions of CH radicals. Note, no CH desorption process is proposed as a result of negligible scattered signals in our IRIS experiments:





As shown in reaction 9, CH radicals may react with active sites on the surface to form intermediate radicals, which sequentially convert to stable C_2 products. The probability of CH surface loss via reaction 9 clearly depends on the surface density of active sites. From the literature, the surface coverage percentage of sp^3 -CH groups, sp^2 -CH groups, and active sites on the surface of an amorphous hydrogenated carbon film is $\sim 95\%$, $< 1\%$, and 4% , respectively.³⁹ This means that the surface loss of CH radicals via reaction 9 occurs with low possibility due to the low density of active sites on the surface of a-C:H film. Alternately, CH radicals may react with C-H bonds on the surface via reactions 10 and 11, because of a large amount of C-H bonds on the surface of a-C:H film. Considering the high reactivity rate of CH radicals with H_2 in the gas phase via $CH + H_2 \rightarrow CH_2 + H$ (rate coefficient is $2.01 \times 10^{-10} \text{ cm}^3/\text{s}$)⁴⁰ and the lower bond energy of C-H (413 kJ/mol) than that of H-H (436 kJ/mol),⁴¹ we can reasonably speculate that reactions 10 and 11 can occur with high probability on the surface, although there are no direct kinetic data for these reactions. The intermediate C_2 active sites can be quickly filled by CH_3 and CH_2 radicals coming from gas phase via reaction 10 and 11, respectively, resulting in film growth. From the discussion above, CH is clearly involved in film growth despite its low gas-phase density.

Knowledge of energy partitioning between different plasma species is important to an overall understanding of the chemistry occurring in low-temperature plasmas. It is commonly accepted that the average rotational temperature of gas-phase species (including stable species, as well as transient species such as radicals) is equal to the average gas temperature.⁴²⁻⁴⁵ The results presented here, however, are in apparent disagreement with this assumption, because Θ_T is considerably higher than Θ_R for CH in methane plasmas. During the dissociation process by electron impact reactions, the electron energy is used to dissociate precursor molecules, and the released excess energy is transferred to the dissociated fragments. Therefore, high initial translational and rotational energies for these fragments can be obtained from the high electron energy. As observed in the present work, Θ_R is independent of P , Ar fraction and pressure, which indicates that the high initial rotational temperatures have been thermalized because of the high rotational relaxation rate for CH. However, the Θ_T values measured in 100% CH₄ and CH₄/Ar plasmas are significantly higher than the Θ_R values (this is more obvious at low pressure), which suggests that the initial high translational energy has not been thermalized prior to extraction from the plasma reactor.

In Figure 6.8a, two very high Θ_T values obtained at the low P can be explained by higher electron temperatures in the low-power regime. This has been confirmed by our previous diagnostic data in CH₄/Ar plasmas using a Langmuir probe.³⁵ In that study, we also found that the electron temperature, T_e , is nearly constant in the high-power regime. The variation in Θ_T can, therefore, be explained by the change in T_e in the plasma. Moreover, the lower Θ_T values at the higher reactor pressure, Figure 6.8b, are consistent with this assumption, as T_e usually decreases with increasing pressure.²⁵ Although there are no direct data available on translational relaxation rates for CH

created by electron-impact dissociation of CH_4 , the data obtained here indirectly support another assumption that the relaxation rate of the translational energy is much lower than that of rotational energy and the reaction rate between CH and CH_4 . Considering the high reaction rate with CH_4 in the gas phase, CH radicals probed in the molecular beam are produced relatively close to the extraction orifice. Radicals with higher translational temperature will have fewer collisions than colder CH. As a consequence, the CH that survives and is extracted into the molecular beam could be relatively hot. These CH radicals would also have less opportunity for full equilibration. Ar addition to the plasma increases the possibility of thermalizing collisions. As can be seen in Figure 6.8b, however, the CH translational energy was still not thermalized even when the gas mixture was 20% Ar. Further increasing the argon fraction in CH_4/Ar mixtures, however, is limited by the significant decrease in CH signal at higher Ar fractions. In a previous study, we measured the $\Theta_T(\text{SiH})$ in $\text{Si}_2\text{H}_6/\text{Ar}$ plasmas as a function of argon fraction.³¹ We found that the $\Theta_T(\text{SiH})$ decreased significantly with increasing argon fraction, because the added argon significantly decreased the probability of a chemical reaction between SiH and SiH_4 due to the decrease in SiH_4 density in $\text{Si}_2\text{H}_6/\text{Ar}$ plasmas. Hence, although not strictly parallel to our present system, these results indicate that the initial high translational energy still can be relaxed via non-reactive collisions.

6.4. Summary

The surface reactivity of CH radicals produced in CH_4/Ar plasmas as a function of various parameters including applied rf power, argon fraction, T_s , and substrate bias has been measured using the IRIS technique. A surface reactivity of nearly unity has been observed for CH under all conditions studied. This very high

reactivity suggests that the CH radical has a significant influence on the properties of the hydrogenated carbon films, despite its relatively low gas-phase density in CH₄ plasmas. In addition, the kinetic translational temperature and the rotational temperature of CH were measured. Θ_R is essentially independent of P and gas composition, which indicates that the rotational energy of CH radicals is thermalized due to the high rotational relaxation rate. Θ_T values are, however, considerably higher than the Θ_R , especially at low source pressures, suggesting the thermodynamic equilibrium for Θ_T has not been established in these systems. The high initial Θ_T is likely a result of the excess energy released in the electron impact dissociation process of CH₄ and is also associated with the electron temperature in the plasma.

References

- (1) Haverkamp, J.; Mayo, R. M.; Bourham, M. A.; Narayan, J.; Jin, C.; Duscher, G. *J. Appl. Phys.* **2003**, *93*, 3627.
- (2) Choi, W. S.; Chung, I.; Lee, Y. Z.; Hong, B. *Surf. Coat. Technol.* **2004**, *180-181*, 254.
- (3) Umehara, Y.; Murai, S.; Koide, Y.; Murakami, M. *Diamond Relat. Mater.* **2002**, *11*, 1429.
- (4) Lung, B. H.; Chiang, M. J.; Hon, M. H. *Thin Solid Films* **2001**, *392*, 16.
- (5) Ueng, H. Y.; Guo, C. T. *Appl. Surf. Sci.* **2005**, *249*, 246.
- (6) Brown, M. S.; Forlines, R. A.; Ganguly, B. N. *J. Appl. Phys.* **2005**, *97*, 1.
- (7) Tang, W.; Liu, J.; Huang, T.; Lu, F. *Diamond Relat. Mater.* **2001**, *10*, 327.
- (8) Sun, Z.; Xu, S.; Ostrikov, K. N. *Diamond Relat. Mater.* **2002**, *11*, 92.
- (9) Lee, J. J. *Surf. Coat. Technol.* **2005**, *200*, 31.
- (10) Morrison, N. A.; William, C.; Milne, W. I. *J. Appl. Phys.* **2003**, *94*, 7031.
- (11) Yamashita, Y.; Toyoda, H.; Sugai, H. *Jpn. J. Appl. Phys.* **1989**, *28*, 1647.
- (12) Brinkman, E. A.; Raiche, G. A.; Brown, M. S.; Jeffries, J. B. *Appl. Phys. B* **1997**, *64*, 689.
- (13) Hummernbrum, F.; Kempkens, H.; Ruzicka, A.; Sauren, H. D.; Schiffer, C.; Uhlenbuschl, J.; Winter, J. *Plasma Sources Sci. Technol.* **1992**, *1*, 221.
- (14) Tachibana, K.; Mukai, T.; Yuuki, A.; Matsui, Y.; Harima, H. *Jpn. J. Appl. Phys.* **1990**, *29*, 2156.
- (15) Luque, J.; Juchmann, W.; Jeffries, J. B. *Appl. Opt.* **1997**, *36*, 3261.
- (16) Menningen, K. L.; Chids, M. A.; Toyoda, H.; Ueda, Y.; Anderson, L. W.; Lawler, J. E. *Contrib. Plasma Phys.* **1995**, *35*, 359.

- (17) Kaminski, C.; Ewart, P. *Appl. Phys. B* **1995**, *61*, 585.
- (18) Yun, J.; Dandy, D. S. *Diamond Relat. Mater.* **2005**, *14*, 1432.
- (19) Keudell, A. V.; Meier, M.; Schwarz-Selinger, T.; Jacob, W. *J. Appl. Phys.* **2001**, *89*, 2979.
- (20) Thiesemann, H.; MacNamara, J.; Taatjes, C. A. *J. Phys. Chem. A* **1997**, *101*, 1881.
- (21) Fisher, E. R. *Plasma Process. Polym.* **2004**, *1*, 13.
- (22) Zhang, J.; Williams, K. L.; Fisher, E. R. *J. Phys. Chem. A* **2003**, *107*, 593.
- (23) Zhang, J.; Fisher, E. R. *J. Phys. Chem. B* **2004**, *108*, 9821.
- (24) Williams, K. L.; Fisher, E. R. *J. Vac. Sci. Technol. A* **2003**, *21*, 1024.
- (25) Lieberman, M. A.; Lichtenberg, A. J. *Principles of Plasma Discharges and Material Processing*; Wiley and Sons: New York, **1994**.
- (26) McCurdy, P. R.; Venturo, V. A.; Fisher, E. R. *Chem. Phys. Lett.* **1997**, *274*, 120.
- (27) Bogart, K. H. A.; Cushing, J. P.; Fisher, E. R. *J. Phys. Chem. B* **1997**, *101*, 10016.
- (28) Kessels, W. M. M.; McCurdy, P. R.; Williams, K. L.; Barker, G. R.; Venturo, V. A.; Fisher, E. R. *J. Phys. Chem. B* **2002**, *106*, 2680.
- (29) McCurdy, P. R.; Butoi, C. I.; Williams, K. L.; Fisher, E. R. *J. Phys. Chem. B* **1999**, *103*, 6919.
- (30) Butoi, C. I.; Steen, M. L.; Peers, J. R. D.; Fisher, E. R. *J. Phys. Chem. B* **2001**, *105*, 5957.
- (31) Zhou, J.; Zhang, J.; Fisher, E. R. *J. Phys. Chem. A* **2005**, submitted for publication.

- (32) Luque, J.; Crosley, D. R. LIFBASE: Database and spectral simulation; 2.0.54 ed.; SRI International Report No. MP 99-009, **2005**.
- (33) Martin, I. T.; Fisher, E. R. *J. Vac. Sci. Technol. A* **2004**, *22*, 2168.
- (34) Steen, M. L.; Kull, K. R.; Fisher, E. R. *J. Appl. Phys.* **2002**, *92*, 55.
- (35) Zhou, J.; Ayers, R.; Adams, E.; Martin, I. T.; Liu, D.; Fisher, E. R. *Plasma Sources Sci. Technol.* **2005**, manuscript in preparation.
- (36) Filippov, A. V.; Mankelevich, Y. A.; Pal, A. F.; Rakhimova, T. V.; Ryabinkin, A. N.; Serov, A. O.; Yuriev, A. Y. 17th International Symposium on Plasma Chemistry, **2005**, Toronto.
- (37) Luque, J.; Crosley, D. R. *J. Chem. Phys.* **1996**, *104*, 2146.
- (38) Liu, D.; Martin, I. T.; Zhou, J.; Fisher, E. R. *Pure Appl. Chem.* **2005**, submitted for publication.
- (39) Keudell, A. V.; Meier, M.; Schwarz-Selinger, T. *Appl. Phys. A* **2001**, *72*, 551.
- (40) Fulle, D.; Hippler, H. *J. Chem. Phys.* **1997**, *106*, 8691.
- (41) *NIST Chemical Webbook*; <http://webbook.nist.gov>, **2002**.
- (42) Hertl, M.; Jolly, J. *J. Phys. D: Appl. Phys.* **2000**, *33*, 381.
- (43) Perrin, J. *J. Phys. D: Appl. Phys.* **1993**, *26*, 1662.
- (44) Perrin, J.; Leroy, O.; Bordage, M. C. *Contrib. Plasma Phys.* **1996**, *36*, 3.
- (45) Kessels, W. M. M.; Hoefnagels, J. P. M.; Boogaarts, M. G. H.; Schram, D. C.; Van de Sanden, M. C. M. *J. Appl. Phys.* **2001**, *89*, 2065.

CHAPTER 7

RESEARCH SUMMARY

This dissertation chapter addresses general considerations for plasma polymerization and plasma enhanced chemical vapor deposition. Additionally, future directions for this work are briefly discussed.

Deposition of coatings by plasma enhanced chemical vapor deposition (PECVD) is the most complex of all plasma surface treatment techniques. Full understanding is still limited, and the development of new deposition processes is mostly empirical. Advanced diagnostic techniques for both gas-phase species and plasma-surface interactions enable us to better understand the mechanisms of film growth. In thermal chemical vapor deposition (CVD) systems, the film growth is determined by thermodynamic reactions of species and controlled by the substrate temperature. The film growth in plasma reactors, however, originates from the bombardment of a flux consisting of all active species, such as radicals and ions which are created through the dissociation of precursor molecules primarily by electron impact. The characterization of these active species and electron energy, therefore, is critical for in-depth understanding of film growth.

In a low-temperature plasma, the free radical density is up to 10^5 times higher than the ion density; the plasma polymerization of organic molecules thus occurs generally through radical-molecule reactions.¹ Among a variety of plasma parameters, the electron energy in plasmas is a critical parameter during plasma polymerization. For example, as noted in Chapter 3, a higher degree of retained functional group in the polypyrrole backbone can be obtained by increasing the duty cycle of pulsed plasmas. The literature also shows that an energy of 0.0015 eV is consumed per styrene molecule for a typical chemical polymerization of styrene leading to polystyrene of a molecular mass of 100 kDa.² This energy is much lower than the average electron energy in our inductively coupled plasmas (ICPs) (1-10 eV). Moreover, the radical chain propagation is exothermic, and therefore, requires no additional energy.² The excess energy in the plasma will, therefore, lead to a large number of side reactions due to the rupture of the chemical bonds in the monomer.

For plasma polymerization of chemically well-defined polymers, lower electron energy and longer duty cycles are usually adopted.

Ion energy is another critical component of low-temperature plasma deposition processes. The substrate in these deposition systems is often negatively biased with respect to the plasma potential by means of an external power supply, so positive ions play a very important role in plasma-surface interactions. Positive ions bring energy to the surface and, thus, can assist chemical reactions and desorption of weakly volatile species, or induce direct sputtering. Ions are also chemically reactive species and their role on deposition or etching may not be negligible if their flux is comparable to that of neutral species. As described in Chapter 4, when the ion energy is lower than 30 eV, the deposited hydrocarbon film is more polymer-like. In addition, radicals still appear to be the primary contributors to the growth of DLC films due to their high density. In DLC film growth process, high-energy ions break the surface C-H bonds and etch away weak C-C bonds. The active sites created by high-energy ions are filled quickly by hydrocarbon radicals, leading to DLC film growth.

Although the IRIS studies of CH radicals have been investigated in this dissertation, additional IRIS work could be conducted to provide more information about DLC film growth mechanisms. As mentioned in Chapter 4, H and CH₂ are also important gas-phase radicals not only because of their high density in the plasma gas phase, but also because of their direct participation in the growth of DLC films. It has been speculated that H radicals may act as etchants to abstract H atoms from surface C-H bonds to create surface active sites.^{3,4} CH₃ and CH₂ radicals can then react with these active sites, ultimately, leading to film growth. To date, the direct evidence on the surface reactivity of H and CH₂ radicals is still missing. In the literature, H radicals have been detected by a two-photon LIF technique,⁵ and the B-A transition of

CH₂ has been studied by LIF.⁶ These LIF detection methods could help us to investigate the surface reactivity of these two radicals using our IRIS technique in the future.

Additional IRIS studies of the surface reactivity of H radicals as a function of ion energy would also be a reasonable future direction for these studies. As shown in this dissertation, high-energy ions significantly increase the hardness of DLC films. But it is still not clear how these high-energy ions etch surface hydrocarbon bonds and what the etched products are. If high-energy ions break C-H bonds on the surface of hydrocarbon films, H radicals could be created at the surface during this process. As a result, the scattered H signals from the surface should increase with increasing ion energy. Therefore, experimental studies using IRIS may provide more data on plasma-surface interactions, which will help elucidate mechanisms of DLC film growth.

In addition to the uses for plasma-deposited DLC films, CH₄-containing plasmas, such as H₂/Ar/CH₄ plasmas, have been also used for the production of high quality diamond films.^{7,8} The IRIS methods and data presented in this dissertation offer an opportunity to extend our research to explore the effects of multiple species, such as H, C, C₂, C₃, CH, and C₂H₂, in a single diamond film deposition system. Currently, the main concerns are focused on how different plasma species influence film growth, which needs more data about radical-surface interactions. The obtained information will be helpful to better understand the mechanisms of diamond film growth. Among these interesting species, the IRIS study of C₂ radicals is currently underway in the Fisher group. The C₂ radical is considered to be an important species during diamond film growth. Gruen and coworkers observed a strong correlation between C₂ emission and diamond film growth rate.⁷ Klein-Douwel *et al.* found C₂

emission relate to diamond film quality.⁹ Moreover, the absolute concentration of the C₂ radical in a microwave excited diamond PECVD has been measured by LIF.¹⁰ The transition of d³Π_g-a³Π_u Swan band near 473 nm was excited and the induced fluorescence was subsequently observed in the (1,1) band and some in the (0,0) band at 511 and 516 nm, respectively.¹⁰ Therefore, the IRIS studies of the C₂ radical, such as surface reactivity, ion energy effects on surface reactivity, and the energetics of C₂, would be useful for elucidating the roles of C₂ during DLC and diamond film growth. Combined with the results presented in this work, a very complete picture of the mechanisms for hard carbon film growth will be developed.

References

- (1) Grill, A. *Cold Plasma in Materials Fabrication from Fundamentals to Applications*; The Institute of Electrical and Electronics Engineers: New York, **1994**.
- (2) Friedrich, J.; Kuhn, G.; Mix, R.; Fritz, A.; Schonhals, A. *J. Adhesion Sci. Technol.* **2003**, *17*, 1591.
- (3) von Keudell, A.; Meier, M.; Schwarz-Selinger, T. *Appl. Phys. A* **2001**, *72*, 551.
- (4) von Keudell, A.; Meier, M.; Schwarz-Selinger, T.; Jacob, W. *J. Appl. Phys.* **2001**, *89*, 2979.
- (5) Woutersy, M. J.; Khachan, J.; Falconer, I. S.; James, B. W. *J. Phys. D: Appl. Phys.* **1998**, *31*, 2004.
- (6) Ashfold, M. N. R.; Fullstone, M. A.; Hancock, G.; Ketley, G. W. *Chem. Phys.* **1981**, *55*, 245.
- (7) Gruen, D. M.; Zuiker, C. D.; Krauss, A. R.; Pan, X. *J. Vac. Sci. Technol. A* **1995**, *13*, 1628.
- (8) Bruno, P.; Benedic, F.; Tallaire, A.; Silva, F.; Oliveira, F. J.; Amaral, M.; Fernandes, A. J. S.; Cicala, G.; Silva, R. F. *Diam. Relat. Mater.* **2005**, *14*, 432.
- (9) Klein-Douwel, R. J. H.; Zuiker, C. D.; Krauss, A. R.; Pan, X. *J. Appl. Phys.* **1995**, *78*, 2086.
- (10) Kaminski, C.; Ewart, P. *Appl. Phys. B* **1995**, *61*, 585.